Observation of Iron (III) and Iron (II) Chloro Species at the Air-Aqueous Interface via Second Harmonic Generation Spectroscopy

Dissertation

Presented in Partial Fulfillment of the Requirements for the Degree Doctor of Philosophy in the Graduate School of The Ohio State University

By

Ka Chon Ng

Graduate Program in Chemistry

The Ohio State University

2022

Dissertation Committee

Prof. Heather C. Allen, Advisor

Prof. Bern Kohler

Prof. L. Robert Baker

Prof. Peter F. Craigmile

Abstract

Iron speciation in solution is relatively well understood, yet interfacial distributions of iron species are not. In the following chapters, interfacial species of inorganic iron (III) and (II) chloride solutions at the air-aqueous interface are investigated. In Chapter 1, iron speciation in bulk and at the interface of salt solutions is summarized. This literature review chapter provides a background on the iron chemistry, iron complexes from speciation, difference of ion population between bulk and interface, and experimental techniques in surface studies. Chapter 2 explores the observation of interfacial $FeCl_3$ species by surface sensitive spectroscopic techniques. Through a series of measurements, the speciation of iron (III) complexes is determined using UV/Visible absorption spectroscopy, comparison to calculation (ChemEQL-generated speciation curves), and second harmonic generation (SHG) experiments. To explore the possibility of resonant iron (III) chloro species, molar absorptivity, and dipole moment calculations were carried out. At concentrations below 0.6 mol/kg water, SHG data of $FeCl_3$ solutions reveal destructive interference and a nonresonant electric-field response due to the structural ordering effect from the $[FeCl_2(H_2O)_4]^+$ complex. At concentrations above 3 mol/kg water, with 800 and 860 nm laser excitation, SHG response of $FeCl_3$ showed trends that fit to Frumkin-Fowler-Guggenheim adsorption model as opposed to the Langmuir model. With the excitation of 760 nm, the trend of SH E-field exhibited two

different slopes. The different trend suggests the surface adsorption of $[FeCl_3(H_2O)_3]^0$ at the excitation of 800 and 860 nm, where the presence of $[FeCl_4]^-$ is suggested with SHG excitation at 760 nm. However, the interfacial existence of $[FeCl_2(H_2O)_4]^+$ complex is not ruled out. In Chapter 3, the presence of acidified $FeCl_2$ ($FeCl_2$-HCl) species is identified by a systematic study using UV/Visible absorption, Raman spectroscopy, and SHG. UV/Visible absorption spectra and speciation curves of acidified $FeCl_2$ solutions determined the existence of a dominant species in the acidified solution. Raman spectroscopy reveals a perturbed hydrogen-bonding network of water molecule at high concentration. In SHG measurements, the SH E-field of acidified $FeCl_2$ solution showed a trend that follows the Langmuir adsorption model. Evaluation of the data and resonance then suggests the presence of $[FeCl(H_2O)_5]^+$ within the aqueous interface. Overall, these studies show that the iron (III) chloride solutions retain speciation at the air-aqueous interface, of which adsorption of the $[FeCl_3(H_2O)_3]$ complex is suggested through resonance analysis. On the other hand, SHG response of iron (II) chloride solution shows a trend that can fit to a simple Langmuir adsorption model. Our spectroscopic measurements suggest that $[FeCl(H_2O)_5]^+$ is predominant at the solution interface, and the higher Cl:Fe species, $[FeCl_2(H_2O)_4]$, is not likely formed in solution interface.

Dedication

This dissertation is dedicated to Nien-Ching Han, who has constantly supported me throughout this process.

Acknowledgments

Perusing a doctoral degree is never easy, but I found this journey is way more enjoyable and valuable. First, I would like to acknowledge my advisor Professor Heather Allen for her great support, help, and encouragement. As a role model of a successful researcher and teacher, she shows me how an enthusiastic, responsible, and ideal advisor should be. I would like to thank my colleagues in the Allen group, I felt fun and motivated working with Allen lab members. I would like to thank Dr. Tehseen Adel and Dr. Jennifer Neal for their knowledge and creativity. I would like to acknowledge Dr. Kimberly Carter-Fenk, Maria Vazquez de Vasquez, and Mickey Rogers for their support in preparing the document and writing. I acknowledge the postdoctoral researchers in the Allen group, Dr. Lu Lin for his great knowledge of nonlinear optics, Dr. Stephen Baumler, Dr. Ankur Saha, and Dr. Kamal Ray for their knowledge and attitude in research. I would like to thank Dr. Elizabeth Alexander for her support and knowledge while I was working as an instrumentation teaching associate. I would also like to thank my undergraduate researcher Zuqi Liu who helped with some experimental measurements.

I would like to thank my friend and collaborator Professor Ka Un Lao for his support in theoretical aspect. I would like to thank my roommate Jaehoon Yang for sharing your life experience and knowledge in simulation. I would also like to thank my

family for their support and my parents for the great freedom of my determination.

Lastly, I would like to thank my fiancé, Dr. Nien-Ching Han, for her constant support and love over these years, my Ph.D. life became more enjoyable and meaningful with you.

Vita

2010…… B.A. Chemistry, National Tsing Hua University, Hsinchu, Taiwan

2013…… M.A. Chemistry, National Tsing Hua University, Hsinchu, Taiwan

2013…… Technician, National Tsing Hua University, Hsinchu, Taiwan

2014-2016…… Research Assistant, Academia Sinica, Taipei, Taiwan

2016-2021…… Graduate Teaching Associate, Department of Chemistry and Biochemistry, The Ohio State University

2021-2022…… Graduate Research Associate, Department of Chemistry and Biochemistry, The Ohio State University

Publications

Adel, T.; **Ng, K.C.**; Vazquez de Vasquez, M.G; Velez-Alvarez J.; Allen, H.C. Insight into the Ionizing Surface Potential Method and Aqueous Sodium Halide Surfaces. *Langmuir* **2021**, *37*, 7863-7874.

Grooms, A.J.; Neal, J.F.; **Ng, K.C.**; Zhao, W.; Flood, A.H.; Allen, H.C. Thermodynamic Signatures of the Origin of Anti-Hofmeister Selectivity for Phosphate at Aqueous Interfaces. *J. Phys. Chem. A* **2020**, *124,* 5621-5630.

Lin, L.; Husek, J.; Biswas, S.; Baumler, S.M.; Adel, T.; **Ng, K.C.**; Baker, L.R.; Allen, H.C. Iron(III) Speciation Observed at Aqueous and Glycerol Surfaces: Vibrational Sum Frequency and X-ray. *J. Am. Chem. Soc.* **2019**, *141*, 13525-13535.

Fields of Study

Major Field: Chemistry

Table of Contents

List of Tables

List of Figures

List of Abbreviations

CAD	Computer-aided design
CCD	Charge-coupled device
CW	Continuous wave
DFT	Density functional theory
EDL	Electrical double layer
EM	Electron multiplier
EMCCD	Electron-multiplying charge-coupled device
ESS	Energy storage system
FFG	Frumkin-Fowler-Guggenheim
LJ-XPS	Liquid-jet X-ray photoelectron spectroscopy
LMCT	Ligand to metal charge transfer
MD	Molecular dynamic
QE	Quantum efficiency
RFBs	Redox flow batteries
RPE	Resonant photoelectron spectroscopy
SHG	Second harmonic generation
STP	Standard temperature and pressure
UV	Ultraviolet
VSFG	Vibrational sum-frequency generation

XAFS	X-ray absorption find structure
XANES	X-ray absorption near-edge structure spectroscopy
XAS	X-ray absorption
XPS	X-ray photoelectron spectroscopy
XRD	X-ray diffraction
XUV-RA	Extreme ultraviolet reflection-absorption

Chapter 1. Introduction

1.1.1 Introduction of Iron

Iron is the most abundant transition metal on Earth and plays an important role in natural and industrial processes. The abundance of iron is ~32% by mass from geological analysis and consists of 80% in the core of Earth.[1–3]

Additionally, there is also a huge variety of Fe in ocean. The primary source of iron in ocean is from dust.[4] There are 41.0 Tg per year of iron from dust emitted from mineral and 8.4 Tg per year of total iron is deposited over global oceans.[5] Iron can also become airborne, where atmospheric iron in aerosols are generated by dessert dust. About 95% of this iron aerosol represents the global atmospheric budget.[6] The iron-contained aerosol is insoluble. However, the aerosol participates the atmospheric cycle and become more soluble for marine consumption.[7] Soluble iron is the most utilized transition metal in biology too. Iron is a vital element for the synthesis of chlorophyl for bio organisms.[8] In the biological cycle, environmental and bio-released iron is taken up by phytoplankton in seawater. The consumed iron is produced in a form of excess iron-binding ligands by the phytoplankton.[9] Dissolved iron occurs as +2 and +3 oxidation state in seawater, the presence of iron (II) cation initiates the Fenton reaction naturally in the ocean.[10–12]

Iron is widely used in industry because of its low cost, low toxicity and general stability.[13] It is shown that the consumption of iron ore reached 2,315 million tons in

2019.[14] 98% of the iron ore is used in the steel market.[15] Iron is also widely used in industrial purposes such as wastewater treatment,[16,17] manufacturing,[18] and technology.[19–21] In wastewater treatment, iron cation reacts with hydrogen peroxide to remove the organic compounds.[22] Iron chloride is the common etchant that is used in printed circuit boards.[23] Iron chloride is also used in iron oxide nanoparticle synthesis and can be used as a contrast agent in magnetic resonance imaging[24,25] and site-specific drug delivery.[26,27] Besides the applications of iron nanoparticles, iron is extensively used in coordination chemistry.[28,29] In addition, iron (II) and (III) chloride are used as a material for energy storage.[30–34] For example, the all-iron redox flow battery exploits the redox potential of iron (II) and (III) ions at both sides of the electrodes, and is low cost and efficient.[31] Overall, iron is used in a diverse set of natural and industrial applications..

1.1.2 Iron in Solution Chemistry

Iron is a transition metal with various oxidation states from -2 to +7. In compound forms, it usually exhibits +2 and +3 states with hydrated forms at ambient temperature such as iron (III) chloride hexahydrate ($FeCl_3 \cdot 6H_2O$) or iron (II) chloride tetrahydrate ($FeCl_2 \cdot 4H_2O$). The appearance of iron compounds is usually colored because of the ligand-to-metal charge transfer process between iron and the bonded ligands.[35,36]

In neutral solution, inorganic salt solution of iron compounds undergoes speciation. The number of species is found and stability constants of iron complexes are determined from prior studies. Experimental techniques such as ultraviolet (UV)/Visible absorption, Raman spectroscopy, and X-ray absorption have been used to investigate iron solutions.[37–

[46] Speciation of $FeCl_3$ solution has been confirmed as three classified species. For instance, iron (III) chloride ($FeCl_3$) aqueous solution speciates into three groups: (A) Fe-Cl species: $[Fe(H_2O)_6]^{3+}$, $[FeCl(H_2O)_5]^{2+}$, $[FeCl_2(H_2O)_4]^{+}$, $[FeCl_3(H_2O)_3]^{0}$, and $[FeCl_4]^{-}$, (B) mononuclear hydrolysis products form by stepwise deprotonation: $[Fe(H_2O)_5(OH)]^{2+}$, $[Fe(H_2O)_4(OH)_2]^{+}$, $[Fe(H_2O)_3(OH)_3]_{(aq)}$, $[Fe(H_2O)_2(OH)_4]^{-}$, and (C) polynuclear hydrolysis products: $[Fe_2(H_2O)_8(OH)_2]^{4+}$, $[Fe_3(H_2O)_{10}(OH)_4]^{5+}$. Hydrolysis products usually have low solubility and thus become precipitate.[47] It is shown that speciation of Fe-Cl species is sensitive to the environment. For instance, at 25 ºC and concentration below 1 mol/kg water, $[Fe(H_2O)_6]^{3+}$ and $[FeCl(H_2O)_5]^{2+}$ are dominant in the solution. However, for 4 mol/kg water, $[FeCl_4]^{-}$ and $[FeCl_3(H_2O)_3]^{0}$ becomes equivalent, with a minor portion of $[FeCl_2(H_2O)_4]^{+}$ in the solution.[48] Temperature also alters the population of iron (III) species. Previous work showed that the relative concentration of $[FeCl_4]^{-}$ increased at high concentration.[49]

Structure of the species depends on the hydration of water. From density functional theory (DFT) calculation with polarizable continuum model, it is suggested that the calculated structure of $[Fe(H_2O)_6]^{3+}$, $[FeCl(H_2O)_5]^{2+}$, $[FeCl_2(H_2O)_4]^{+}$ are octahedral complexes, and the averaged second solvation shell is around 23. For bipyramidal $[FeCl_3(H_2O)_3]^{0}$, there are 21 water molecules in the second solvation shell. For tetrahedral $[FeCl_4]^{-}$, hydration number is 20.[50]

It is reported that speciation of iron (II) chloride solutions is relatively simple. Results from stability constant measurements suggest the existence of $[Fe(H_2O)_6]^{2+}$, $[FeCl(H_2O)_5]^{+}$, $[FeCl_2(H_2O)_4]^{0}$, $[FeCl_4]^{2-}$ in the solution.[51–55] It is also shown that the

formation of hydrolysis products also occur: $[Fe(OH)]^{+}$ and $Fe(OH)_2$.[56,57] Note that tetrahedrally complexed $[FeCl_4]^{2-}$ is only formed in high temperatures and/or concentrated solution.[49,54] Solvation effect of iron (II) species is less investigated, but the hydrated number of water molecules for $[FeCl(H_2O)_5]^{+}$ is 7,[58] which is less than a half of iron (III) complexes.

The studies of speciation of iron (III) and iron (III) are well developed, but speciation of iron complexes at air-aqueous surface is less understood.

1.1.3 Interface study

Surface tension is the first experimental evidence of the difference between bulk and interface. Gibbs adsorption equation shows that an increase in surface tension of inorganic salt solution represents the ions is expelled from the interface.[59–61] The theoretical viewpoint of this expression was proposed that a point charge from a dielectric medium is expelled by an image charge from another dielectric medium.[62,63]

However, previous work on gas uptake experiment suggested the halide anion must be present on the liquid surface, which contradicted the results from surface tension.[64] Further molecular dynamic simulation (MD) with polarization potentials showed supportive results to the experimental evidence.[65,66] Results of MD shows that highly polarizable anions are preferentially adsorbed on the surface. When ions are polarized at the interface, the anisotropic environment allows the anions to create a dipole. Interfacial anions are less solvated, but interact with surrounding water molecules to compensate the reduced solvation.[63] It was considered the halide anions are expelled from surface by

surface tension. However, with the polarizable model, highly polarizable anions such as iodide and bromide, showed an adsorption behavior to the surface.[67]

Previous works on vibrational sum-frequency generation (VSFG) have shown that surface enhancement of polarizable anion in the OH stretch region, suggested an increased on interfacial depth.[68–71]

Second harmonic generation spectroscopy (SHG), an analogous technique to VSFG, was also used to probe the electrical dipole of the anions for the surface study.[72–76]

Another surface sensitive technique called liquid-jet X-ray photoelectron spectroscopy (LJ-XPS) is beneficial to aqueous sampling and detected in X-ray. Ghosal *et al.* also suggested that the bromide anion is enriched at the aqueous surface using LJ-XPS experiments.[77]

There are only a few studies focused on the interfacial species of iron. Previous work reported by Allen, Baker and coworkers used VSFG and proposed the solvation at aqueous surface of Fe(III) complexes ($[FeX_2(H_2O)_4]^+$ (x = Cl, OH or H_2O)) at concentrations above 1.5 mol/kg water.[78] The hydration shell O-H stretching modes of the $[FeX_2(H_2O)_4]^+$ (X = Cl, H_2O or OH) species were identified by the indirect probe by VSFG. Additionally, the surface enhancement of iron to chloride is about 1.7 determined by ambient pressure XPS.[78] Brandes *et al.* suggested that the ferrocyanide $[Fe(CN)_6]^{4-}$ was observed on solution surface, and the increased SFG intensity of OH stretch is due to the formation of electrical double layer (EDL) by highly charged anions.[79]

LJ-XPS and resonant photoelectron spectroscopy of iron (III) chloride solutions revealed the $[FeCl(H_2O)_5]^{2+}$ species is the dominant interfacial complex at low

concentrations, followed by the second abundant species $[FeCl_2(H_2O)_4]^+$. Nevertheless, monovalent $[FeCl_2(H_2O)_4]^+$ is the most abundant, followed by the approximately equal amount of $[FeCl(H_2O)_5]^{2+}$ and $[FeCl_3(H_2O)_3]$ species.[80] Another LJ-XPS experiments on iron (III) hydrolysis products reported by Seidel *et al.* showed the formation of oligomers when the ration of [OH]:[Fe] is less than 0.25. At higher [OH]:[Fe] ratio, aggregated Fe-OH oligomers were observed from the K-edge bands of iron chloride.[81]

LJ-XPS of $FeCl_2$ reported by Bruce *et al.* suggested that $[FeCl(H_2O)_5]^+$ is strongly repelled from surface after the formation of complex, as well as a decreased Cl^- concentration was observed.[82]

1.2 Motivation

It is challenging to distinguish iron species when it undergoes speciation as iron (III) chloride is potentially diverse into 11 iron complexes. The goal of this dissertation is to observe the complexity of iron chloride species at the aqueous surface by SHG and the adsorption behavior of cations on surface. We could apply the experience of analyzing SHG signal to other simpler electrolyte system after unveiled the complex SHG signal of iron chloride solution. In the studies in the following chapters, we hypothesize that the speciation of iron (III) and iron (II) chloride solutions at air-aqueous is different than the iron speciation in the bulk. Furthermore, these studies provide a new insight of interfacial response of iron species in SHG, redox Fe (II)/(III) cations, and even transition metal salt solutions.

Chapter 2. Iron (III) Chloro Complexation at the Air-Aqueous $FeCl_3$ Interface via Second Harmonic Generation Spectroscopy

Manuscript submitted: Ka Chon Ng,[†] Tehseen Adel,[†] Ka Un Lao,[‡] Meredith G. Varmecky,[†] Zuqi Liu,[†] Mouad Arrad,[§] Heather C. Allen[*,†]

[†]Department of Chemistry & Biochemistry, The Ohio State University, Columbus, OH 43210, United States

[‡]Department of Chemistry, Virginia Commonwealth University, Richmond, VA 23284, United States

[§]Department of Process Engineering, National School of Mines of Rabat (ENSMR), BP 753 Agdal, Rabat, Morocco

Abstract

Renewable energy sources are an attractive solution for reducing greenhouse gas emissions; yet, these renewable energies require energy storage. Among large-scale energy storage systems, the iron redox flow battery is a candidate because of its low-cost, long lifetime, and safety. Aqueous interfaces are the gateway to many electrochemical reactions, including those that involve soluble Fe (III). However, interfacial iron complexation and iron surface prevalence are not well understood, especially under the inherently acidic conditions of $FeCl_3$ solutions. In this study, we investigate interfacial Fe (III) species using second harmonic generation (SHG) combined with surface tension and UV/Visible absorption. Surface selective techniques such as SHG have been widely applied to unveil

the unique surface properties within the air-aqueous interface. Here, we perform SHG with excitation at 760, 800 and 860 nm. For 800 and 860 nm, kinetics of interfacial $FeCl_3$ molecules follows the Frumkin-Fowler-Guggenheim adsorption model. For 760 nm, we observe two different interfacial concentration regimes marked by two distinctly different SHG trends. Below the 3.0 mol/kg water concentration of $FeCl_3$, nonresonant SHG behavior is observed, similar to the E-field generated from an aqueous sodium iodide surface, but much larger in magnitude than aqueous NaCl and NaBr solution surfaces. Above 3.0 mol/kg water, an increase in the SHG slope is observed, significantly larger than that of the aqueous sodium halide electrolyte surfaces. Through further evaluation of symmetry and resonant SHG behavior, we determine the existence of the neutral $[FeCl_3(H_2O)_3]$ complex at the air-aqueous interface.

2.1 Introduction

Transition metal salts are prevalent and have important applications in various technologies that include lubrication, catalysis, and electrochemical applications.[29,83,84] Although being largely used in industry, the properties of transition metal salts in aqueous environments are not completely understood. One important application for transition metal salts is the storage of energy.[85–87] As renewable energy harvesting has become a promising method to generate sustainable energy, the production of such energy sources is often not steady over time. Based on the demand of a stable and constant need for energy, an effective energy storage system (ESS) is vital. ESSs plays a role of platform that can do both storage of energy surplus and provide continuous energy.

Redox flow batteries (RFBs) consist of an electrochemical cell where the energy is generated via reduction and oxidation cells and is bridged by a membrane. RFBs have many advantages of large-scale energy storage. Compared to lithium-ion batteries, RFBs have greater lifetime, flexibility, safety, and lower cost.[33] Although the charge/discharge efficiency of RFBs (75% to 85%) are lower than Li-ion batteries (~95%),[88,89] they have longer lifetimes (~10,000 cycles),[90] high durations of energy supply,[91] are thermally secure and operate properly from 15 to 55 ºC,[92] and are easy to recharge and to halt operation.[32] Among different types of RFBs, iron RFBs has shown the advantages of being nontoxic and affordable.[30,33,93,94] Catalysis of iron RFBs have been well characterized. For example, iron (III) chloride solution is commonly used in iron RFBs, and have focused on optimizing the characteristics of solutions at the electrode surface.[30,93] Another study showed metal deposition at the negative electrode, lowering the efficiency of charging.[31] Noble and coworkers revealed that sorbed $FeCl_4^-$ in anion-exchange membranes caused a decrease of ionic conductivity in all-iron RFBs at high $FeCl_3$ concentration (> 1.4 M).[34] Understanding iron (III) chloride solution interfacial interactions provides input for maximizing operation efficiency of iron RFBs.

Studying salts of Fe (III) in aqueous environments is challenging due to high complex speciation and inherent acidity. Only recently have such studies been conducted at the air-aqueous interface.[78,80,81] Yet, prior investigations on much simpler electrolyte solutions are extensive.[69,72,74,76,95,96] Studies over the last two decades indicate the surface enrichment of anions and complexes at the air-aqueous interface using different experimental techniques such as microjet X-ray photoelectron spectroscopy (XPS) of

liquids,[97] vibrational sum-frequency generation (VSFG),[68,98] second harmonic generation (SHG),[72,74,75] and molecular dynamics (MD) simulation.[67] In 2001, anion enrichment at aqueous surfaces was predicted to arise from polarizability and size effects, although the current mechanism is under debate. Anion surface enrichment for bromide and iodide anions was supported by VSFG studies that showed an increase in the interfacial depth.[69] Ghosal *et al.* also suggested that the bromide anion is enriched at the aqueous surface using liquid-jet XPS experiments.[77]

For iron complexation at aqueous surfaces, prior studies of $FeCl_3$ aqueous solutions suggested the surface propensity of specific Fe (III)-chloro complexation products.[78,80,81] Thürmer *et al.* using LJ-XPS and resonant photoelectron spectroscopy (RPE) concluded that the divalent $[FeCl(H_2O)_5]^{2+}$ species is the dominant interfacial complex at low concentrations. This is despite the monovalent $[FeCl_2(H_2O)_4]^{+}$ species being the second most abundant complex in the solution phase. However, starting at 1.5 mol/kg water $FeCl_3$, the monovalent $[FeCl_2(H_2O)_4]^{+}$ is indicated to become the most abundant, followed by the divalent $[FeCl(H_2O)_5]^{2+}$ and neutral $[FeCl_3(H_2O)_3]$ species.[80] In a different study, Seidel *et al.* using LJ-XPS revealed that interfacial Fe-OH oligomers are formed when the [OH]:[Fe] ratio is less than 0.25.[81] By observing the K-edge absorption characteristics of the 1s to 3d transition for iron chloride, symmetry information of ferric complexes were determined. At higher [OH]:[Fe] ratios, Fe-OH oligomers were observed to aggregate.[81] Consistent with Thürmer *et al.*, Allen, Baker, and coworkers using extreme ultraviolet reflection-absorption (XUV-RA) and angle-resolved X-ray photoelectron spectroscopy studies measured the Fe 2p edge signal that identified the ratio of Fe:Cl within the air-glycerol interface to be 1:2.[78]

In addition, using VSFG they proposed the solvation at the aqueous planar surface of Fe (III) complexes ($[FeX_2(H_2O)_4]^+$ (X = Cl, OH or H_2O)) at concentrations above 1.5 mol/kg water. XPS and VSFG provide different yet complementary information, and in addition their probe depths differ substantially.[78] In their study, VSFG indirectly probed the aqueous $FeCl_3$ surface speciation in which the hydration shell O-H stretching modes of the $[FeX_2(H_2O)_4]^+$ (X = Cl, H_2O or OH) species were identified.[78] Additionally, the surface enrichment of Fe (III) relative to that of chloride was also observed to be nearly twice the concentration compared to a bulk solution of glycerol, a proxy for water, using angle resolved and ambient pressure XPS.[78]

In the study presented here, SHG is applied to $FeCl_3$ aqueous solution surfaces and analyze the contribution of the interfacial electric dipole response revealing a nonlinear trend. SHG, similar to SFG, is a surface specific technique that reports on the interfacial electric dipole. Moreover, SHG can effectively excite an interfacial species (i.e. the $FeCl_3$ ions and complexes in this study) when the molecules/ions are resonantly enhanced with the same or doubled frequencies of the fundamental light source. Here, sub-molal to concentrated solutions of $FeCl_3$ are studied, in which a subset of $FeCl_x^{3-x}$ ($x = 0 \sim 4$) complex electronic transitions are resonant with wavelengths used. Thus, the SHG data allows a new view of the aqueous $FeCl_3$ solution surface, one that has not been reported prior in the literature.

As a first experiment, the surface tension of aqueous $FeCl_3$ solutions is measured and compare to NaCl and acidified NaCl solution. We follow with analysis of the UV/Visible spectra of aqueous iron chloride solutions and evaluate the spectra to provide

an understanding of resonant versus nonresonant SHG for the $FeCl_3$ solutions. The effect of the molar absorptivity is determined as it relates to the interpretation of the SHG response. SHG from each solution surface at 20 °C without pH adjustment for concentrations ranging from 1.0 mmol/kg water to 5.5 mol/kg water was then measured. The Gibbs free energy of adsorption (ΔG) is determined for complexes of $FeCl_3$. Combining this data and with the insight that SHG is insensitive to centrosymmetric species, e.g. $[FeCl_2(H_2O)_4]^+$ and $[Fe(H_2O)_6]^{3+}$, our results then provide a unique determination of $FeCl_3$ complexation within the air-aqueous interface. Based on our combined results, our series of studies point to the existence of the neutral Fe complex $[FeCl_3(H_2O)_3]$ at the air-aqueous $FeCl_3$ interface. This determination does not rule out the existence of previously identified monovalent $[FeCl_2(H_2O)_4]^+$ species, nor the $[FeCl_4]^-$, and moreover we expect such species to be interfacially present although not detectable due to SHG symmetry rules.[78]

2.2 Experimental Section

2.2.1 Solution Preparation

Before solution preparation, all glassware was cleaned by an established acid cleaning method. The acid cleaning solution was prepared by mixing 8 grams of ammonium peroxydisulfate powder (Certified ACS) per 500 mL of sulfuric acid (Fisher Chemical, Certified ACS Plus). Glassware was immersed into the acid cleaning solution for at least two hours to remove any organics and metals, followed by rinsing with copious amounts of Milli-Q water (18.2 MΩ, Milli-Q Advantage A10). The glassware was dried in an oven until

all the remaining water was removed. Ferric chloride hexahydrate ($FeCl_3 \cdot 6H_2O$, ACROS 99+%, Analysis) was used without further purification. Sodium chloride (NaCl, ACROS 99+%, Analysis) was baked in the oven at 650 °C for 6 hours, sodium bromide (NaBr, ACROS 99.5%, Analysis) and sodium iodide dihydrate ($NaI \cdot 2H_2O$, ACROS 99+%, Analysis) were baked in the oven at 600 °C 6 hours to remove any of the organic impurities.[99] The pH of $FeCl_3$ solutions was measured to be from pH of 4 to pH of -1.3. The purity of the 3 mol/kg water $FeCl_3$ solutions was confirmed with vibrational sum frequency spectroscopy measurement in the C-H stretching modes around 2900 cm^{-1} to ensure no detectable residue of the organic species present on the aqueous surface.[78] Acidified sodium chloride solution was prepared by adding hydrochloric acid into NaCl solution. The pH values that were used for these NaCl solutions were determined from the measured pH of $FeCl_3$ solutions at the same concentration.

2.2.2 Surface Tension

Surface tension measurements were made using a platinum Wilhelmy plate with a Biolin Scientific Sigma 703 D force tensiometer. Measurements were carried out in an acid-cleaned glass dish. Before sample measurement, 10 mL ultrapure water was pipetted and measured, then the surface tension of water was calibrated to the surface tension value at the corresponding temperature.[100] The water was removed with a fresh pipette and replaced with the sample solution. Surface tension measurements were reproduced in triplicate for

all concentrations. All measurements were carried out at an average of 20.5 °C and 25% relative humidity.

2.2.3 UV/Visible Absorption

UV/visible absorption experiments were carried out using a PerkinElmer Lambda 950 UV/Vis/NIR spectrometer. Absorption spectra of $FeCl_3$ were taken with a series of spacers to control the absorption path length to adjust a whole range of concentration from $1x10^{-3}$ to 2 mol/kg water by applying spacers with thickness from 1 cm to 6 μm. UV/Visible spectra were normalized to the path length and a comparison of relative molar absorptivity was calculated for each concentration. Hydrolysis products of $FeCl_3$ were observed at low concentration (below 0.01 mol/kg water) within 4 hours. To avoid formation of hydroxides, iron chloride solutions were freshly prepared and were measured after they were completely dissolved in neat water.

2.2.4 Second Harmonic Generation Spectroscopy

The SHG instrument (Figure 1) was described previously although some modifications have been made and are discussed briefly below.[101] The instrument uses a reference channel at ~400 nm to monitor any fluctuations caused by the potential unstable laser power and output mode.[102,103] A single charge-coupled device (CCD) camera was used to collect both signal and reference channels at the same time. This collection method eliminates uncertainty due to both laser power and mode. A broadband Ti: sapphire laser

(Tsunami, Spectra-Physics) has a frequency centered at 805 (bandwidth of 20 nm) with a pulse width of sub 50 fs and 82 MHz repetition rate. The laser beam is initially pumped by a continuous wave (CW) laser (Millennia Vs, Spectra-Physics) with a pump power of 5.00 W. The average output power from the Tsunami was around 850 mW and the average power of excitation was ~ 600 mW. SHG measurements were completed with p-in/p-out excitation/detection polarizations with exposure times of each data point at 90 seconds. The SHG signal and reference data were collected and binned separately, followed by calibration of the reference channel and then normalized to the ratio of 1.0, which is fixed as the SHG signal of water. The SHG data are plotted as the square root of the SHG signal intensity, referred as the SHG E-field. SHG were averaged by three trials. Details of calculating the effective surface second order susceptibility $\chi_{s,eff}^{(2)}$, coherence length and alignment procedure of SHG are noted in Appendix A, B, and C, respectively.

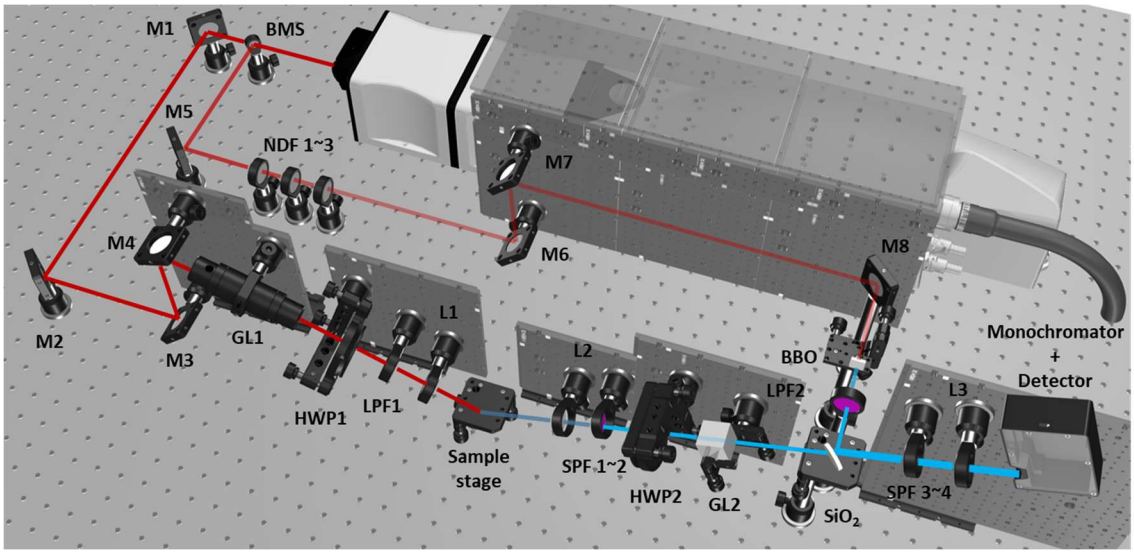

Figure 1 Schematic representation of the second harmonic generation spectroscopic instrument. BMS: 85/15 beam splitter. M1 ~ M8 are dielectric mirrors. GL1, GL2 are 800 nm and 405 nm Glan-laser polarizer. HWP1, HWP2 are 800 achromatic half-wave plate and 405 nm half-wave plate. L1~L3 are +75 mm, +100 mm, and +50 mm plano-convex lenses with antireflective coating between 650 to 1050 nm. LPF1~2: 690 nm long pass filter, SPF1~4 are 785 nm short pass filters. SiO_2 is silica plate, NDF1~3 are neutral density filters. BBO is BBO crystal. The incident angle of 805 nm beam is 67.2º. The graphical computer-aided design (CAD) is constructed from 3DOpticX.

2.2.5 Computation

The most stable geometries of $[Fe(H_2O)_6]^{3+}$, $[FeCl(H_2O)_5]^{2+}$, $[FeCl_2(H_2O)_4]^{+}$, $[FeCl_3(H_2O)]$, $[FeCl_3(H_2O)_2]$, $[FeCl_3(H_2O)_3]$, and $[FeCl_4]^{-}$, and the corresponding dipole moments were calculated at the level of M06/def2-TZVPPD using Q-Chem v. 5.1[104] where M06[105] has been recommended for transition-metal chemistry and dipole moment predictions.[106,107]

2.3 Results and Discussion

Fe (III) chloride speciation in aqueous solutions has been investigated extensively over decades[38,41,48,108] using various experimental techniques including that of UV/Visible absorption, Raman spectroscopy, X-ray diffraction (XRD), X-ray absorption spectroscopy (XAS), and X-ray absorption fine structure spectrometry (XAFS).[37,40,42,43,45,48,108–113] Techniques of surface tension, UV/Visible absorption, and second harmonic generation spectroscopy were used to illustrate the unexpected surface tension values/trends, the potential SHG resonances, and the SHG response, respectively. These finding is correlated with interfacial speciation. Comparison to monovalent sodium halide salt measurements is to provide baseline behavior given that we expect the experimental results from interfacial $FeCl_3$ speciation to be complex and nontrivial to interpret.

2.3.1 Surface Tension Measurements

The intensity of intermolecular forces within the interface can be estimated from the surface tension measurements of aqueous solutions. While surfactant molecules decrease the surface tension of water, electrolytes increase the surface tension. Here, consistent with the expectation for electrolytes in solution, a surface tension increase was observed with increasing concentration and ionic strength of aqueous $FeCl_3$ (Figure 2a). Evaluating these measurements using the Gibbs adsorption equation, one might suggest that the Fe species are depleted from the surface.[59–61] However, Tobias and others have shown this to be an oversimplification and that depletion of an ion can be integrated over a larger interfacial region and can coexist with enrichment nearer to the topmost surface layers.[65,67,114,115] XPS experiments, SHG and SFG also support the idea of surface enrichment of several ions.[72,77,81,96,116] Using surface tension data, Pegram *et al.* developed a partitioning coefficient to describe the ion equilibrium between the surface-bulk phases.[117,118] For 1.0 M NaCl, the estimated surface concentration of chloride was determined to be nearly 0.70, which is different from the bulk concentration, with sodium depletion from the near surface region. However, Pegram *et al.* concluded that the 0.70:1 surface-to-bulk ratio indicates that chloride is moderately excluded from the surface. Although for aqueous NaBr and NaI, surface enrichment of the halide has been predicted and confirmed by others,[62,67,69,74,77] large surface excess of chloride is less clear. In general, the partitioning coefficient is related to the solution concentration but also the ion's valence state, and that this behavior is further impacted by the anions counter cation, e.g. sodium versus ferric.

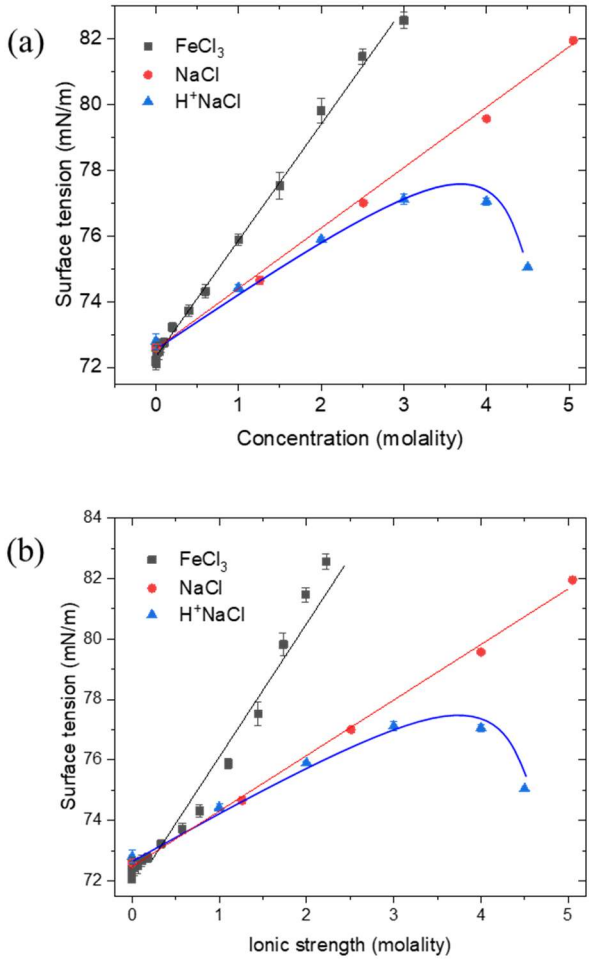

Figure 2 (a) Surface tension of $FeCl_3$, NaCl, and acidified NaCl. $FeCl_3$ speciation exhibits dominance of Cl^- and $FeCl_2^+$ (90%).[77] (b) Surface tension measurement of $FeCl_3$, NaCl and acidified NaCl in speciation calibrated ionic strength. Note that the ionic strength of $FeCl_3$ is calculated from the concentration of speciation of $FeCl_3$ complexes; $FeCl_2^+$ species is dominant in calibrated concentration. Solid lines are visual guides.

In our experiments on aqueous ferric chloride solution surfaces, the surface tension increment of aqueous $FeCl_3$ (3.3 mN/m·(mol/kg water)$^{-1}$) is higher than NaCl (1.8 mN/m·(mol/kg water)$^{-1}$) at the same concentrations; note that speciation of $FeCl_3$ complicates comparison using ionic strength. In addition, the $FeCl_3$ surface tension data points are linear and similar in magnitude to salts such as $MgCl_2$ in which solvent shared ion pairs are formed in the interfacial region.[119,120] It is also noted that $FeCl_3$ solutions are highly acidic and one might expect that the surface tension should resemble that of an acid or an acidified salt. In general, acid solutions decrease the surface tension of water. In Figure 2a and the ionic strength plot in Figure 2b, we observe this expected turnover of the acidified NaCl as pH is decreased (Table 1). Although, to our surprise, the $FeCl_3$ surface tension does not decrease despite a pH lower than 1. Although perplexing, there is an interesting anticorrelation of our surface tension data to the suppressed OH stretch signal intensity as reported by Lin *et al.* such that it was indicated that symmetrically complexed water molecules within the interfacial $[FeCl_2(H_2O)_4]^+$ was responsible for the lack of intensity.[78,121] Given the large magnitude and linear surface tension behavior, and the lack of acidic surface tension response, we used SHG spectroscopy to report on the interfacial electric dipole response. Prior, we explored the potential for resonance SHG behavior using UV/Visible absorption spectroscopy.

Table 1 Measured pH of freshly prepared (HCl) acidified NaCl solution.

Concentration of NaCl (molality)	**pH**
4.5	-1.125
4	-0.703
3	-1.211
2	0.183
1	0.782

2.3.2 UV/Visible Absorption of Ferric Chloride

UV/Visible absorption spectroscopy probes the electronic transition of the ligand to metal charge transfer (LMCT) process and is informative concerning the speciation of $FeCl_3$ solutions.[28] Thus, UV/Visible absorption is expected to reflect the composition of the ferric species due to their absorption of LMCT as per Beer-Lambert law. The spectra also provide information on the resonant enhancement of the SHG given that our incident beam is from 760 to 860 nm and the SHG occurs from 380 to 430 nm. Resonance effects any of these wavelengths will aid in understanding the chemical origin of the SHG signal.

In Figure 3a, the UV/Visible was used to measured extinction coefficient of $FeCl_3$ aqueous solutions as a function of concentration. The inset of Figure 3a shows the absorptivity at 380, 400, and 430 nm for comparison to the absorptivity speciation plot in Figure 3b. Given that the molar absorptivity plot (Figure 3b) at three wavelengths and our measured extinction coefficient (inset of Figure 3a) does not manifest the same value, the measurements imply more than one species contribute to the UV/Visible spectra. Among the iron (III) species, non-octahedral species $[FeCl_3(H_2O)_x]$ and $[FeCl_4]^-$ possess the strongest molar absorptivities compared to other octahedral complexes. We thus note that the UV/Visible absorption is determined by the strong extinction of these 3 species: $[FeCl_2(H_2O)_4]^+$, $[FeCl_3(H_2O)_x]$ and $[FeCl_4]^-$.

The contribution from hydroxide species is negligible in these solutions, less than 1% of the solution concentration due to the low pH. However, the $[Fe(H_2O)_4(OH)_2]^+$ and $[Fe_2(OH)_2]^{4+}$ have a resonance from 380 to 430 nm.[47,122]

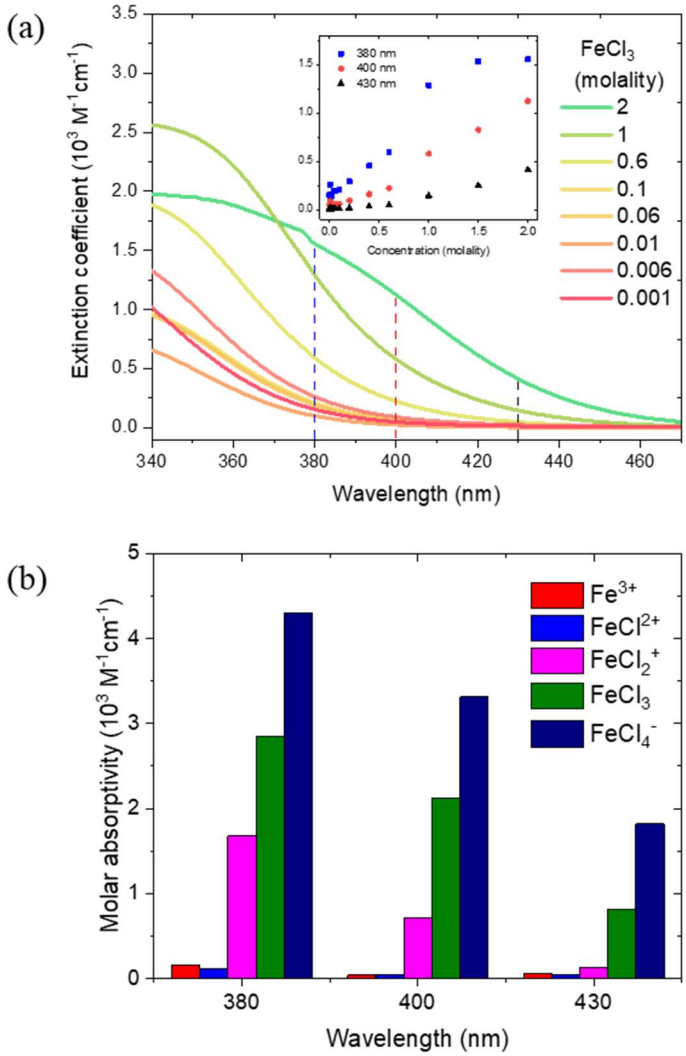

Figure 3 (a) Extinction coefficient of $FeCl_3$ in aqueous solution (inset, the absorptivity at 380 (blue), 400 (red) and 430 nm (black) versus concentration). (b) Molar absorptivity of Fe complex speciation with corresponding wavelengths from Liu *et al.*[47] Note that $[FeCl_3(H_2O)_x]$ and $[FeCl_4]^-$ have the strongest absorption and therefore will be SHG resonant. The $[FeCl_2(H_2O)_4]^+$ is also resonant, but much weaker. The overall trend of molar absorptivity decreases from 380 to 430 nm.

2.3.3 Speciation, Ion Pairing and Hydration of $FeCl_3$ in Solution

Unlike simple salts, such as sodium chloride, ferric chloride undergoes speciation to form complexes of chloride, water, and hydroxyl under aqueous conditions,[37,41,123] and in solution is known to form $Fe(H_2O)^{3+}$, $[FeCl(H_2O)_5]^{2+}$, $[FeCl_2(H_2O)_4]^{+}$, $FeCl_3$ and $[FeCl_4]^{-}$ ions. The hexa-aqua Fe(III) ion will undergo hydrolysis to form $[Fe(OH)(H_2O)_5]^{2+}$, $[Fe(OH)_2(H_2O)_4]^{+}$, and $[Fe(OH)_3(H_2O)_3]$, a process that is pH dependent. At higher concentrations, the hydrolysis product abundance is low.[40,41,47,113,124] Speciation curves of iron (III) species were determined with the complex formation with the ligands of H_2O, Cl^-, and OH^-. Fe(III)-chloro speciation curves in Figure 4 were calculated using the measured pH values of $FeCl_3$ solutions shown in Table 2; the literature equilibrium constants used in these calculations were taken from Baumler *et al.*.[44]

The speciation plot of Figure 4 shows that the octahedral species of $[Cl(H_2O)_6]^-$ has the highest solution concentration and is followed by $[FeCl_2(H_2O)_4]^{+}$, $[FeCl(H_2O)_5]^{2+}$, and $[Fe(H_2O)_6]^{3+}$. An asymmetric mixed octahedral or tetrahedral/trigonal bipyramidal $[FeCl_3(H_2O)_x]$ (x = 1 (tetrahedral), x = 2 (trigonal bipyramidal), x = 3 (octahedral)) contributes less at low concentration but becomes more significant at high concentration. Tetrahedral $[FeCl_4]^-$ is the least concentrated species, although it is relatively more abundant at higher concentrations. Table 3 summarizes the speciation products that are formed by deprotonation from $[Fe(H_2O)_6]^{3+}$ and the formation of all ferric complexes that strongly depend on the pH value of the solution. As shown in Figure 5, speciation curves of iron (III) hydroxides are enriched when the pH is above 3.0. In this study, the selected

concentrations for the aqueous $FeCl_3$ have inherently low pH (0.1 M $FeCl_3$, pH = 1.8). Thus, we assume that the impact of hydrolysis products on our measurements is minimal.

Ion pairing and ion hydration are considered as competitive effects although both play a role in hydration of iron complexes.[70,125] Havenith and coworkers determined the number of hydration water molecules ($n_{hydration}$) for $FeCl^{2+}$ and $FeCl_2^+$ to be 21 and 17, respectively.[58] From their data, we estimated the minimum number of affected water molecules from our speciation curves (Table 4). In our calculations, Fe species in the solution phase are completely hydrated by water molecules at low concentration of $FeCl_3$ solution. However, at high concentration (> 2 mol/kg water), the number of water molecules present is not sufficient to fully hydrate all the Fe complexes.

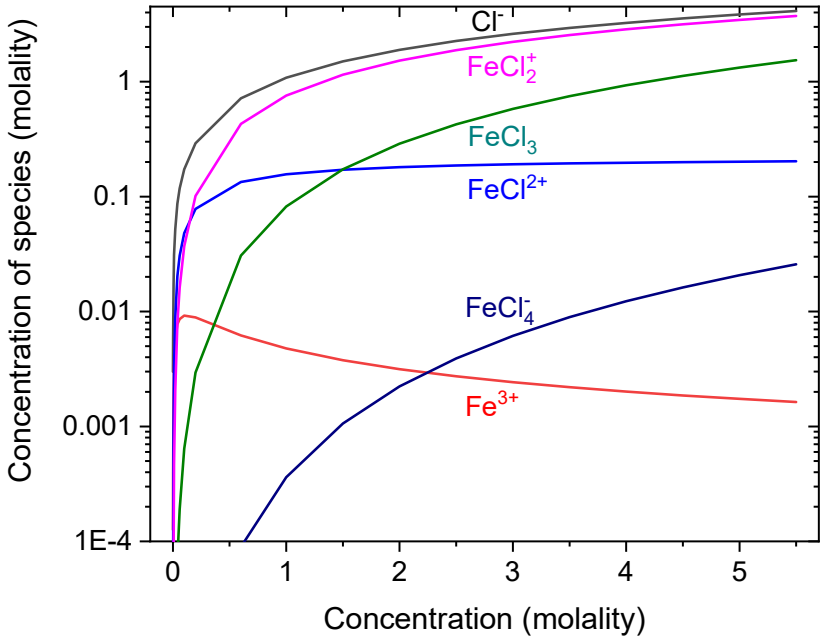

Figure 4 Speciation curves for Fe species versus concentration. Calculations were made using ChemEQL software. $[Cl(H_2O)_6]^-$ is in black $[Fe(H_2O)_6]^{3+}$ in red, $[FeCl(H_2O)_5]^{2+}$ in blue, $[FeCl_2(H_2O)_4]^+$ in magenta, $[FeCl_3(H_2O)_x]$ in green and $[FeCl_4]^-$ in dark blue.

Table 2 Measured pH of freshly prepared $FeCl_3$ solution.

Concentration (molality)	pH
5.5	-1.262
5	-1.062
4.5	-0.846
4	-0.631
3	-0.241
2.5	-0.043
2	0.192
1.5	0.440
1	0.702
0.6	0.923
0.4	1.279
0.2	1.577
0.1	1.706
0.06	2.049
0.04	2.136
0.02	2.421
0.01	2.711
0.006	2.930
0.004	3.179
0.002	3.480
0.001	3.715

Table 3 Species, symmetry, SHG active (noncentrosymmetric), and SHG resonance at 400 nm of iron (III) chloride aqueous solution. Group I is most significant to the SHG E-field; Group II can contribute to the SHG E-field, but not significantly; Group III and IV are not active.

Ion Species	Symmetry	SHG	Resonant at
$[FeCl_3(H_2O)_x]$ where x= 1, 2, 3	T_d (1); Trig. bipy. (2); O_h (3) [48]	Yes	Yes
$[Fe(H_2O)_4(OH)_2]^+$	*cis*-/*trans*- O_h [122]	Yes / No	Yes
$[FeCl(H_2O)_5]^{2+}$	O_h [48,50]	Yes	No
$[Fe(H_2O)_5(OH)]^{2+}$	O_h [48]	Yes	No
$Fe(OH)_3$ (aq)	O_h [122]	Yes	No
$[FeCl_2(H_2O)_4]^+$	*trans*- O_h [48]	No	Yes
$[FeCl_4]^-$	T_d [48]	No	Yes
$[Fe_2(OH)_2]^{4+}$	O_h [122]	No	Yes
$[Fe(H_2O)_2(OH)_4]^-$	O_h [122]	No	No
$[Fe_3(OH)_4]^{5+}$	O_h [122]	No	No
$[Cl(H_2O)_6]^-$	O_h [123]	No	No
$[Fe(H_2O)_6]^{3+}$	O_h [126,127]	No	No

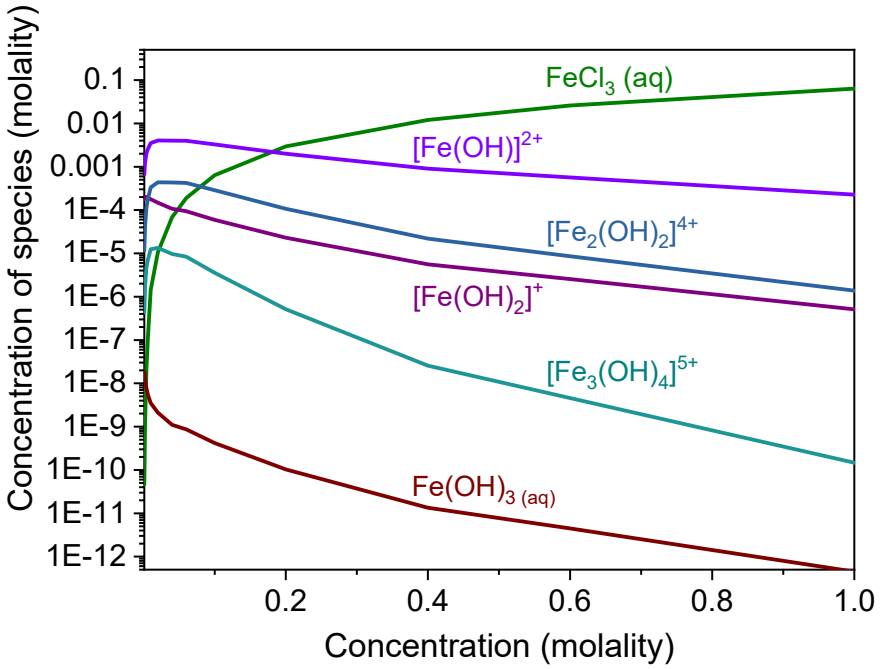

Figure 5 Speciation curves of hydrolysis products ($FeCl_3$ (aq) is plotted for comparison).

Table 4 Extracted molality of species from iron speciation plot. From this data calculation of minimum number of water molecules required for hydration $FeCl_3$ complexes. From prior literature, the hydration water molecule numbers are 5 for chloride anion, 21.4 for $FeCl^{2+}$ and 16.9 for $FeCl_2^+$.[125] The hydration numbers of water molecules for Fe^{3+}, $FeCl_3$ and $FeCl_4^-$ are 24, 21 and 20 by assuming the number of water molecules of first and second hydration shell.[50] We note that from this data, and based on a 55.5 mol/kg water of H_2O at 25 °C, it is clear that there are not enough water molecules in solutions with concentrations at and above 3 mol/kg water Fe species to meet the required number for full solvation.

$$\text{Required } [H_2O] \text{ for full hydration} \sim 5 \times [Cl^-] + 24 \times [Fe^{3+}] + 21.4 \times [FeCl^{2+}] + 16.9 \times [FeCl_2^+] + 21 \times [FeCl_3] + 20 \times [FeCl_4^-]$$

Concentration (mol/kg water)	Concentration of species (mol/kg water)						Required H_2O (mol/kg water)
$FeCl_3$	Cl^-	Fe^{3+}	$FeCl^{2+}$	$FeCl_2^+$	$FeCl_3$	$FeCl_4^-$	
5	3.84	0.00	0.20	3.45	1.32	0.02	110
4	3.25	0.00	0.20	2.86	0.93	0.01	88.6
3	2.60	0.00	0.19	2.22	0.57	0.00	67.0
2	1.89	0.00	0.18	1.53	0.29	0.00	45.3
1	1.08	0.01	0.15	0.76	0.08	0.00	23.4
0.1	0.17	0.01	0.05	0.04	0.00	0.00	2.75

2.3.4 Second Harmonic Generation Spectroscopy

The symmetry of the Fe complex matters such that an SHG active interfacial molecule is one that has a net electric dipole and a noncentrosymmetric structure. Because of SHG selection rules, species that contain a center of symmetry such as $[Fe(H_2O)_6]^{3+}$, $[FeCl_2(H_2O)_4]^{+}$, and $[FeCl_4]^{-}$, are not expected to contribute significantly to the SHG intensity. Moreover, among the ferric complexes, $[FeCl(H_2O)_5]^{2+}$ and $[FeCl_3(H_2O)_x]$ possess an electric dipole and thus should provide a second-order nonlinear response. To confirm a dipole response from the complex species in solution, we used density functional theory at the level of M06/def2-TZVPPD to estimate the electric dipole moments of these ferric complexes (Table 5 and Figure 6). Combining the results from UV/Visible absorption and speciation, we then expect the SHG active species to satisfy both resonance and symmetry conditions (Table 3).

Table 5 Dipole moments in Debye of the iron species at the level of M06/def2-TZVPPD.

Iron Species	**Dipole moment**
$[Fe(H_2O)_6]^{3+}$	0.0000
$[FeCl(H_2O)_5]^{2+}$	6.5395
$[FeCl_2(H_2O)_4]^{+}$	0.0000
$[FeCl_3(H_2O)]$	4.7004
$[FeCl_3(H_2O)_2]$	2.7522
$[FeCl_3(H_2O)_3]$	2.1689
$[FeCl_4]^{-}$	0.0000

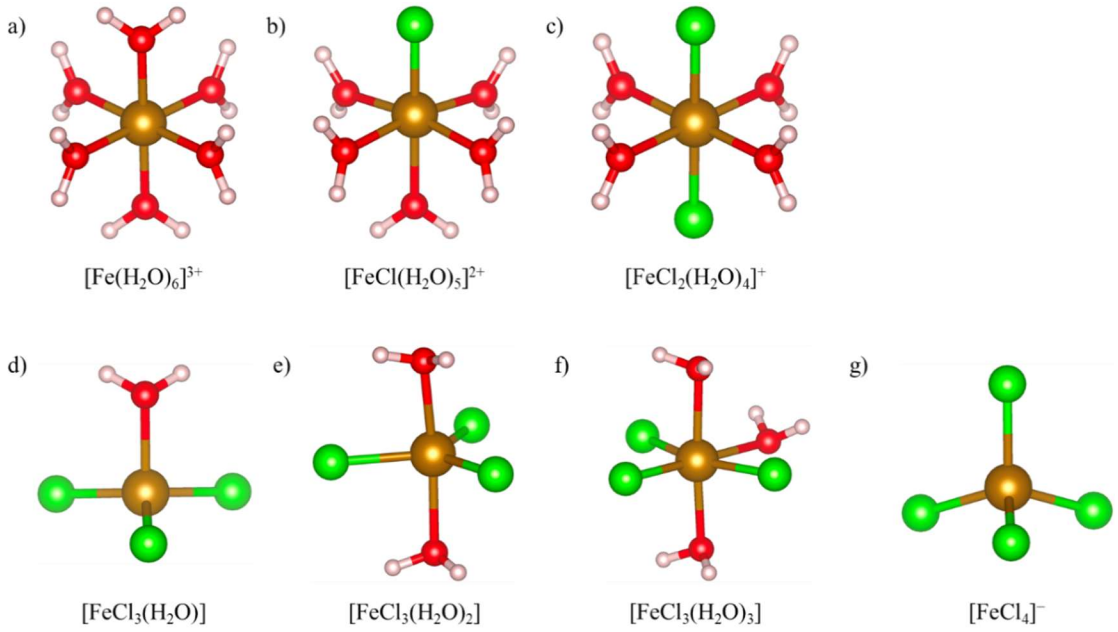

Figure 6 Optimized geometries of iron (III) species at the level of M06/def2-TZVPPD. a) $[Fe(H_2O)_6]^{3+}$, b) $[FeCl(H_2O)_5]^{2+}$, c) $[FeCl_2(H_2O)_4]^{+}$, d) $[FeCl_3(H_2O)]$, e) $[FeCl_3(H_2O)_2]$, f) $[FeCl_3(H_2O)_3]$, g) $[FeCl_4]^{-}$.

In Figure 7a, the SHG measurement of ferric chloride is shown and compared to the nonresonant signal from the NaCl solution surface (See Appendix A for SHG theory and calculation of effective second-order susceptibility), noting that our comparison to the simple halide salt is not to say they are similar, but to provide a baseline response. The SHG intensity has good agreement in the trend and normalized intensity of the sodium halide solutions with previous experiments carried out by Bian *et al.* for the p-in/p-out polarization combination.[95,96] As in the Bian *et al.* study, an increase in the SHG E-field (the square root of the SHG intensity) with increasing concentration of NaCl indicates a greater structural ordering of water by chloride anions in the interfacial region.[95] The SHG electric field of the $FeCl_3$ solution similarly shows a significant increase at higher concentrations.

Examining the low concentration region (< 0.2 mol/kg water) for $FeCl_3$ and (Figure 7b), the fluctuation of the NaCl SHG signal remains only slightly above that of water (normalized to the SHG of neat water, which is a value of 1). The resonant SH electric field from the $FeCl_3$ solutions displays a constant field strength but smaller than the SHG E-field from the NaCl solutions. (This interpretation holds even when plotting SHG vs. ionic strength) It is important to note that the SHG E-field from the $FeCl_3$ solutions is slightly lower than that from water. Here, we suggest that there are two possibilities: first, the nonlinear E-field of $FeCl_3$ is affected by the significant change of refractive index. We estimate the nonlinear second-order correction factor $\chi^{(2)}_{ppp}$ by assuming $\chi_{xxx} = \chi_{yyy} = \chi_{zzz}$ (Figure 8). The nonlinear Fresnel correction factor of $FeCl_3$ indicates a significant decrease of 15% compared to a 5% drop from NaCl. Second, we propose a nonresonant

SH intensity from the low $FeCl_3$ concentrations is due to the destructive interference from SHG inactive and nonresonant species.[72] Thürmer *et al.* using XPS indicated that both $[FeCl(H_2O)_5]^{2+}$ and $[FeCl_2(H_2O)_4]^{+}$ are dominant on the aqueous surface below 1.5 mol/kg water. However, neither the $[FeCl(H_2O)_5]^{2+}$ nor the $[FeCl_2(H_2O)_4]^{+}$ fulfills the SHG selection rule and the resonant condition around 400 nm and therefore are not identifiable from Figure 7b. We then conclude that destructive interference is the likely cause.

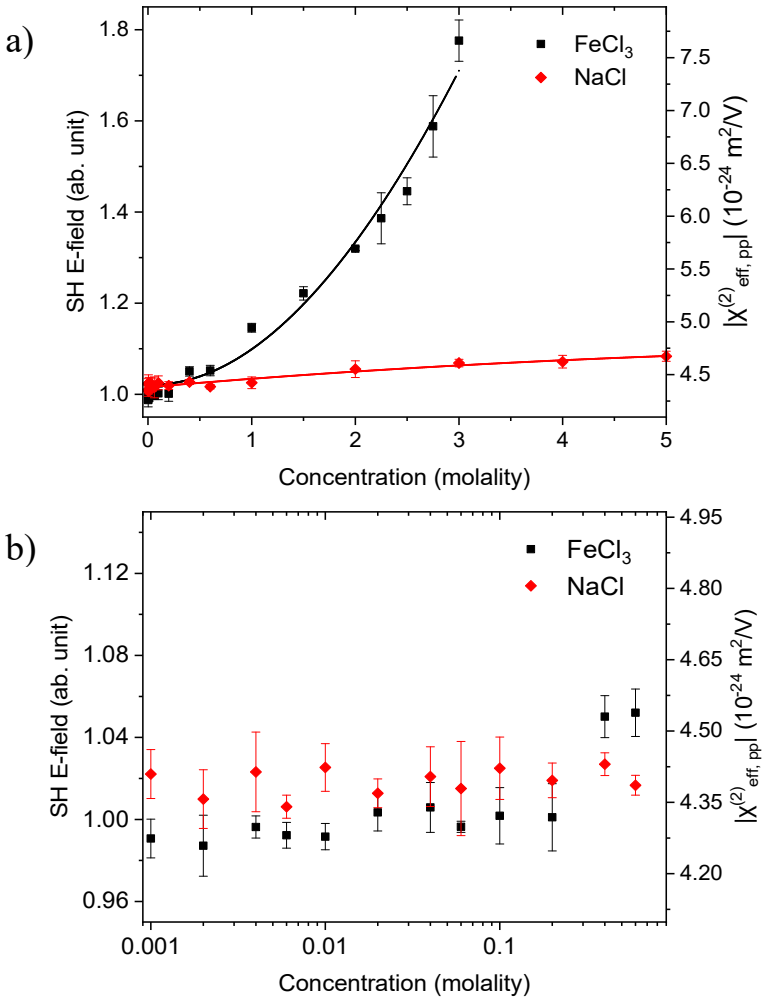

Figure 7 a) SH E-field of $FeCl_3$ (black) and NaCl (red) solutions with a fundamental excitation of 800 nm the curves of visual guide. The signal of neat water is normalized to 1. b) SH E- field of $FeCl_3$ (black) and NaCl (red) in the low concentration range from $1x10^{-3}$ to 0.6 m.

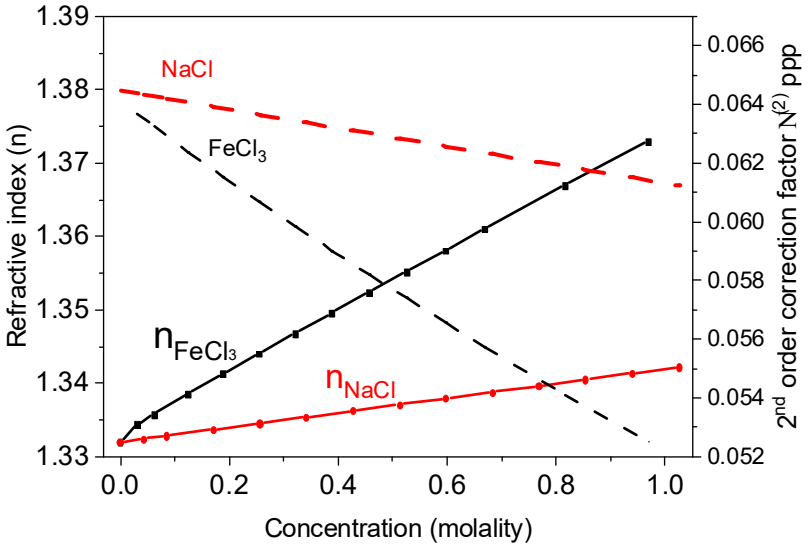

Figure 8 Refractive indices of $FeCl_3$ and NaCl and their Interfacial nonlinear Fresnel correction factors. The refractive indices of $FeCl_3$ and NaCl are from Jamett *et al.* and Leyendekkers *et al.*.[127,128]

SHG response of $FeCl_3$ solutions is observed with wavelength dependency. In Figure 9, we measured the SHG of $FeCl_3$ by the excitation wavelengths of 760, 800 and 860 nm to explore differences in resonance behavior (Figure 3b) and correlate these differences with $FeCl_3$ speciation. $FeCl_3$ solutions reach saturation at relatively high concentrations except as shown in the 760 nm (blue) excitation data.

If we assume resonances contribute to the SHG signal, we can include this term in addition to nonresonant solvent and solute molecules to the total SHG signal response. We also note that the SHG electric field (E_{SHG}) is proportional to the surface coverage (θ) of the total interfacial molecules:[128]

$$\sqrt{I_{SHG}} \propto E_{SHG} \propto \chi^{(2)}_{s,eff} = \chi^{(2)}_{NR,water} + \chi^{(2)}_{R,FeCl_3} = \chi^{(2)}_{NR,water} + \chi^{(2)}_{R,FeCl_3}\theta \quad (2.1)$$

Where I_{SHG} is intensity of second harmonic generation photons, $\chi^{(2)}_i$ is the second-order susceptibility ($i = s,eff, NR,water, R,FeCl_3$ are surface effective, nonresonant water signal and resonant $FeCl_3$ susceptibility, respectively). Note that the surface coverage θ is concentration dependent. Then the SH E-field is normalized by the nonresonant response of water molecules:

$$E_{SHG,Normalized} = 1 + B\theta \quad (2.2)$$

Where the constant $B = \chi^{(2)}_{R,FeCl_3}/\chi^{(2)}_{NR,water}$. Considering the exchange of the Fe (III) species and water molecules, the equilibrium equation and the corresponding equilibrium constant K are stated:[74]

$$Fe^{3+}{}_{Bulk} + H_2O_{Surface} \rightleftharpoons Fe^{3+}{}_{Surface} + H_2O_{Bulk} \quad (2.3)$$

$$K = \frac{[Fe]_{Surface}[H_2O]_{Bulk}}{[Fe]_{Bulk}[H_2O]_{Surface}} = e^{\frac{-\Delta G_{ads}}{RT}} \quad (2.4)$$

Where $[Fe]$ is the concentration of $FeCl_3$ species, ΔG_{ads} is Gibbs free energy of adsorption. When applying for the total surface number N_s^{total} to the surface number of iron species $N_{S,Fe}$, one can obtain the relationship between the surface number of iron and the total surface number of the interfacial species as $N_s^{max} = [Fe]_{Surface} + [H_2O]_{Surface}$. Also, total surface coverage θ is defined as the surface number of iron species divided by the total surface number of species. Surface coverage can be rewritten as:

$$\theta = \frac{N_{S,Fe}}{N_s^{total}} = \frac{[Fe]_{Surface}}{[Fe]_{Surface}+[H_2O]_{Surface}} = \frac{K'[Fe]_{Bulk}}{1+K'[Fe]_{Bulk}} \quad (2.5)$$

Eq. 2.5 is the typical form of Langmuir adsorption model, where $K' = K/[H_2O]_{Bulk} = K/55.5(M)$. With modifications, Frumkin-Fowler-Guggenheim (FFG) model includes a term of lateral interaction w that can be expressed as:

$$K'_{FFG}[Fe]_{Bulk} = \frac{\theta}{1-\theta} e^{-w\theta} \quad (2.6)$$

Where *w* is the interaction parameter. Positive value of *w* corresponds to an attractive lateral interaction and negative value indicates repulsive interaction between adsorbates. By using Eq.2.2, one can fit the SH data of $FeCl_3$ with Langmuir and FFG models (see Appendix D for FFG fitting instruction). As shown in Fig. 9a, the FFG model performs best relative to the Langmuir model. In Fig. 9b, the FFG model shows a good agreement for 800 and 860 nm. However, the FFG model fails to reproduce the data at 760 nm, suggesting further discussion is needed. Our determined values of the Gibbs free energy of

adsorption are negative, and thus agree with the $FeCl_y$ surface enhancement observed by Lin *et al.*.[78] We also note that the interaction parameter also shown in Table 6 for the fits indicates significant lateral interaction, although it is not clear what that interaction is exactly.

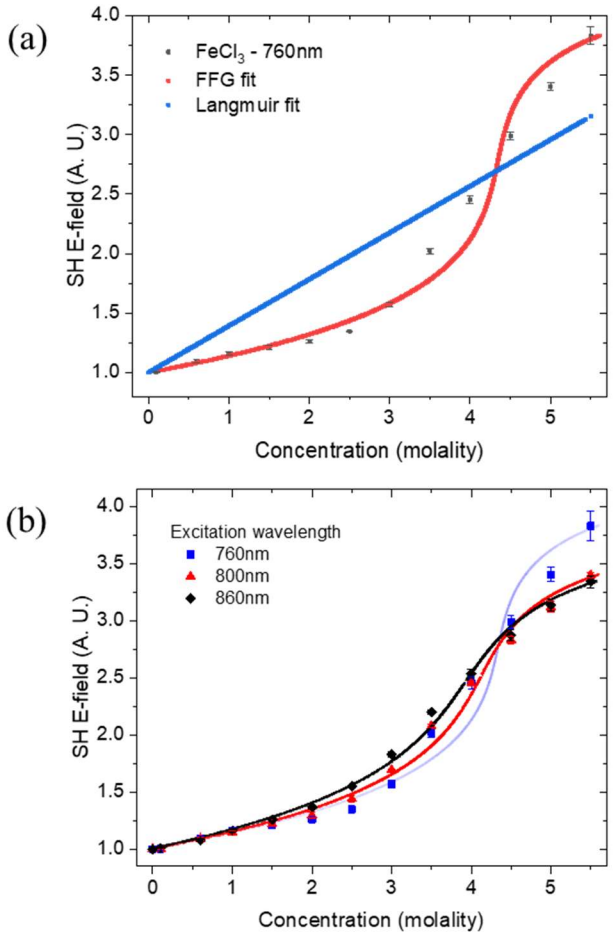

Figure 9 (a) Frumkin-Fowler-Guggenheim (red), Langmuir (blue) fitting models of $FeCl_3$ and (b) SH E-field (arbitrary units) data from 0.1 to 5.5 mol/kg of aqueous $FeCl_3$ solution surfaces. Fundamental wavelength excitation of (blue) 760 nm, (red) 800 nm and (black) 860 nm. Error bars represent one standard deviation. Solid curves are fitting results from the Frumkin-Fowler-Guggenheim (FFG) model. The 760 nm FFG model fits poorly, although the 800 and 860 nm trendline fits very well (see Table 6 for fit parameters and R^2 values).

Table 6 Fitting parameters and results of FFG model for $FeCl_3$ solution.

Excitation wavelength (nm)	K_{FFG}	ΔG_{ads} (kcal/mol)	w	B	R^2
760	1.96	-0.39	3.7	3.5	0.986
800	2.39	-0.51	3.4	3.1	0.995
860	2.75	-0.59	3.2	3.0	0.997

As shown in Figure 10, we contrast the SHG of nonresonant inorganic salt solutions of NaCl, acidified NaCl (pH 0.782 to 0.183), NaBr, and NaI data to the resonant aqueous $FeCl_3$ species at different three wavelengths. We observe that the SHG E-field increases with increasing concentration for all salts. We also observe an SHG increase such that NaCl < acidified NaCl < NaBr < NaI revealing surface activity of the halides in addition to hydronium for the acidified NaCl solution. For both the aqueous NaCl and NaBr, the SHG E-field has excellent agreement with the study from Bian *et al.*.[96] Bian attributed the increase in nonresonant SHG largely to the change of the surface water structure of the first solvation shell of ions.[74] Bian *et al.* also proposed that the effect of the electrical double layer (EDL) was small and not observable in their nonresonant SHG study.[95] The SHG of acidified NaCl is highly different from the SHG of $FeCl_3$ solution, suggestive that the interfacial E-field of $FeCl_3$ is not from net H_3O^+ noting that the $FeCl_3$ solution is highly acidic.

Looking at the SHG resonant response from Figure 10, we can assume that the contribution of EDL $\chi^{(3)}$ effect is negligible due to these high concentrations (Debye length has been completely screened).[129] Lin *et al.* observed a minimal SFG intensity at OH stretching region, suggesting there is no surface charge and then removing the possibility of $\chi^{(3)}$ contribution.[78]

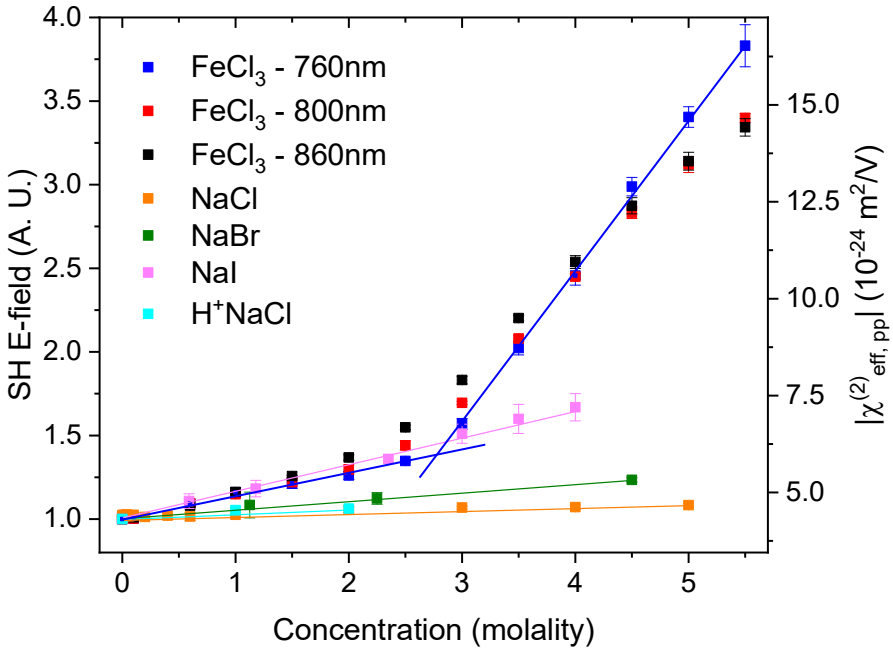

Figure 10 SHG E-field of $FeCl_3$ at different excitation wavelength (blue, 760 nm, red, 800 nm and black, 860 nm) and other inorganic salt solutions. (orange) NaCl, (cyan) acidified NaCl, (green) NaBr and (pink) NaI. Solid lines are a guide to the eye.

The SHG E-field from the $FeCl_3$ solution concentrations of less than 3 mol/kg water follows that of the nonresonant NaI solution. The SHG E-field trend is then deconvoluted into a second slope for concentrations above 3 mol/kg water. The two slopes differ by a factor of ~7 inferring nonresonance from the $FeCl_3$ solution in this lower concentration range and a completely different mechanism giving rise to the second higher concentration slope.

The first slope reveals a nonresonant SHG E-field and is suggestive that centrosymmetric and nonresonant $FeCl_3$ complex species exist in the interfacial region from 0.1 to 3 mol/kg water at the expense of the resonant species. In this concentration regime, we suggest that the SHG intensity is attributed to the structural change of interfacial water molecules, from the second solvation shell and the solvent-shared water in ion pairs from the SHG nonresonant Fe species based on arguments by Lin *et al.* that reported the existence of a second solvation shell of the centrosymmetric iron complex $[FeX_2(H_2O)_4]^+$ (X = Cl, OH or H_2O) in the interfacial region.[78] As noted above, the nonresonant response also includes the nonlinear response from the interfacial water molecules. The second slope is significantly steeper implying a dramatic change in the number density of the Fe, specifically resonant species.

With the comparison of the $FeCl_3$ solution SHG E-field to that from NaI, from prior literature,[69,74] it is known that iodide is strongly surface active and its counter cation interfacial distribution peaks spatially below that of iodide, giving rise to charge separation within the air/water interface. Interfacial charge separation aligns water molecules such that their electric dipoles are more oriented parallel to the surface normal (i.e. structural

ordering of the net electric dipole) of the air/aqueous interface. Additionally, it has been established that iodide has a higher surface propensity than bromide,[68,69] and this is borne out in our SHG measurements as well. Thus, through the same argument with regard to charge separation effectively orienting the water dipoles, we assert that one or more iron species in solution has a significant surface propensity and that the interfacial organization of the complex (or complexes) and their counterions then align water dipoles in the charge separated region. Thus, for $FeCl_3$ concentrations less than 3 mol/kg water, this water dipole alignment derived from surface activity of iron complex surface activity is responsible for the SHG E-field response that is observed to be similar to the E-field response from iodide. Bringing together the two ideas, we conclude that for $FeCl_3$ concentrations less than 3 mol/kg water, and shown by the first slope, the SHG E-field that we observe is due to both the water from a solvated iron complex and the water alignment from charge separation within the interface.

With the concentration of $FeCl_3$ solutions above 3.0 mol/kg water, the second slope suggests that the surface number density of resonant Fe (III) species increases substantially. The question is which iron complex (or complexes) is responsible for the more the slope increase. To answer this question, we first recognize that only 3 of the 5 iron complexes are SHG resonant (Figure 3b): the $[FeCl_2(H_2O)_4]^+$, $[FeCl_3(H_2O)_x]$, and $[FeCl_4]^-$ species. Of these species $[FeCl_2(H_2O)_4]^+$ and $[FeCl_4]^-$ are centrosymmetric and thus SHG inactive. This leaves only the species $[FeCl_3(H_2O)_x]$ as observable by SHG. Thus, we conclude that the neutral $[FeCl_3(H_2O)_x]$ complex is the driver for the dramatic increase in SHG E-field for $FeCl_3$ concentrations above 3 mol/kg water. Formation of contact ion pairs and insufficient

solvation of water molecules in $FeCl_3$ solution might change the electrical dipole of Fe species, and SHG of $FeCl_3$ solutions is potentially affected. We, also suggest that in addition to the identified $[FeCl_3(H_2O)_x]$ species, the monovalent $[FeCl_2(H_2O)_4]^+$ that was previously proposed by Lin *et al.* coexists with the neutral $[FeCl_3(H_2O)_x]$.[78] Although $[FeCl_4]^-$ is SHG silent as well due to the lack of electric dipole, other spectroscopic techniques are needed to rule out this species or to confirm its existence within the interface. Yet, Liu *et al.* reported $[FeCl_4]^-$ is dominant in $FeCl_3$ solution when $[Cl]^-$ is above 12 mol/kg water.[48] At an $FeCl_3$ glycerol solution surface, angle resolved XPS data revealed an increased ratio of Cl:Fe (III) at high $FeCl_3$ concentrations.[78] This was suggestive of a higher ratio Cl:Fe species existing at the aqueous interface, such as the $[FeCl_4]^-$. Thus, for the excitation of 760 nm, interfacial $[FeCl_4]^-$ may contribute to the SH response for solutions above 4.0 mol/kg water.

2.4 Conclusion

Aqueous $FeCl_3$ solution surfaces were investigated to shed light on the identity of interfacial iron complexation species. The surface tension of the $FeCl_3$ solutions suggests complex behavior. $FeCl_3$ solutions are highly acidic (pH 4 to pH -1.3); yet, acidity effects do not explain the surface tension trend. UV/Visible absorption data reveal resonance information for wavelengths 380 to 430 nm. $[FeCl_2(H_2O)_4]^+$, $[FeCl_3(H_2O)_x]$, and $[FeCl_4]^-$ were identified as resonant for the second harmonic generation experiments. The SHG data was then fit to the Frumkin-Fowler-Guggenheim adsorption model with the 400 and 430

nm data fitting very well. The 380 nm data, and deviation from the fit, points to the existence of yet another possible iron surface complex in the high concentration regime. In the lower concentration regime, below 3 mol/kg water, nonresonance contributions appear to dominate the response and thus obscure any assignment of iron interfacial complex. However, at concentrations above 3 mol/kg water, from combining UV/Visible absorption and second harmonic generation in addition to analysis of symmetry and resonance information, the interfacial $[FeCl_3(H_2O)_x]$ neutral complex is determined. In addition, we propose that $[FeCl_4]^-$ may contribute at concentrations above 4 mol/kg water.

Chapter 3. Interfacial Fe (II) Chloride Adsorption Observed via Second Harmonic Generation Spectroscopy

Manuscript in preparation: Ka Chon Ng and Heather C. Allen

Abstract

Divalent iron is involved in many natural processes such as aquatic chemistry, microbiology, and the interconversion cycle of ferrous to ferric ions. Although studies on reactions and speciation of iron complexes have been well investigated, interfacial properties of iron species are less developed. In this study, we aim to measure the interfacial response of acidified $FeCl_2$ solutions by using ultraviolet (UV)/Visible absorption, Raman spectroscopy, and second harmonic generation spectroscopy (SHG). We first identified a dominant species, $FeCl^+$, using UV/Visible absorption. Additionally, Raman spectroscopy was performed and the results revealed a disruption of hydrogen networking between water molecules, leading to the formation of a dominant complexation of $FeCl^+$ in the solution. Subsequent SHG analysis demonstrated a trend following the Langmuir adsorption model, confirming the surface preference of Fe species. Based on our results of UV/Visible absorption and Raman scattering measurements, we propose that $[FeCl(H_2O)_5]^+$ is observed at air-aqueous surface.

3.1 Introduction

Iron is the most abundant transition metal on Earth and is involved in many natural and industrial processes.[4,130–133] Studies of iron in aqueous solution have been investigated extensively theoretically and experimentally.[11,36,39,122,134–136] Iron is a transition metal which consists of divalent (Fe (II) or Fe^{2+}) and trivalent (Fe (III) or Fe^{3+}) compounds. Both Fe^{2+}/Fe^{3+} compounds undergo speciation and can generate diverse species in the solution.[44,48,78,137,138] Literature has shown that Fe^{3+} is more stable than Fe^{2+}.[139,140] Although divalent iron salts are less stable, understanding Fe (II) is still crucial because such species are involved in many natural processes including aquatic chemistry, microbiology, and ferrous wheel.[141,142]

Iron (II) speciation is confirmed by many research groups, but it is limited to bulk phase investigations. For instance, speciation was examined by a potentiometric method,[51] a thermal method,[143] and several spectroscopic methods.[43,144–146] The species in $FeCl_2$ solution are $[Fe(H_2O)]^{2+}$, $[FeCl(H_2O)_5]^{+}$, neutral $[FeCl_2(H_2O)_4]^{0}$, and $[FeCl_4]^{-}$.[143,147] However, the presence of interfacial $FeCl_2$ species is less understood. It has been confirmed that physical and chemical properties of a solution at the air-aqueous interface differs from the bulk phase.[64,66,68,69,148] Hence, there is a need to improve better understanding of interfacial species of Fe (II) chloride. Previously, Bruce *et al.* carried out the liquid-jet X-ray photoelectron spectroscopy (LJ-XPS) of $FeCl_2$ by adding Cl^- into $FeSO_4$ solutions.[82] Their results suggested a strong propensity of $[FeCl(H_2O)_5]^{+}$ complex in bulk phase, as well as a decreased total Cl^- concentration on the surface. As this is the only XPS study of

$FeCl_2$ solution, interfacial properties of aqueous ferrous solutions are still not fully understood.

In this study, surface tension experiments of acidified $FeCl_2$ solutions were measured as a macroscopic picture of the interface. Acidified $FeCl_2$ solutions made by adding an aliquot of aqueous HCl were used to avoid oxidation and formation of $FeCl_3$. Characteristics of $FeCl_2$ solutions in bulk phase were analyzed by UV/Visible absorption and Raman scattering spectroscopy. Additionally, stability constants from literature were used to determine iron (II) speciation. Then, SHG, which is a surface-sensitive technique, was used to monitor the presence of $FeCl_2$ species. Our results show that SHG response of $FeCl_2$ solutions exhibited an enhancement from 0.1 to 3 mol/kg water, following the trend of Langmuir type adsorption. Fitted data suggests a spontaneous adsorption of $FeCl_2$ to the aqueous surface. Combining all the evidence from this study, we systematically observe the adsorption of $FeCl^+$ species to the acidified aqueous solution surface.

3.2 Materials and Methods

3.2.1 Materials

Acid cleaning method was applied for all glassware for sample preparation. Piranha solution was prepared by adding 8 grams of ammonium peroxydisulfate powder (Fisher Chemical, Certified ACS) into 500 mL of sulfuric acid (Fisher Chemical, Certified ACS Plus). Glassware was rinsed by Milli-Q water (18.2 MΩ, Milli-Q Advantage A10) before immersed into the Piranha solution. The glassware was soaked for at least two hours. Acid cleaned glassware was rinsing with copious amount of Milli-Q water before it was dried in

an oven for overnight. Ferrous chloride tetrahydrate ($FeCl_2 \cdot 4H_2O$, Thermo Scientific 99+%) was used without treatment. Sodium chloride (NaCl, ACROS 99+%, Analysis) was baked in at 650 °C for at least 5 hours.

Aqueous $FeCl_2$ solution experienced formation of precipitate, corresponding to its hydrolysis products. To avoid forming precipitation, acidified $FeCl_2$ solution was prepared by dissolving $FeCl_2 \cdot 4H_2O$ powder into 1 mol/kg water hydrochloric acid (measured pH = -0.008) (HCl, Fisher Chemical, Certified ACS) and then equilibrated overnight. Sample preparation of $FeCl_2$ solutions with Milli-Q water and HCl is shown in Figure 11. The pH of the acidified $FeCl_2$ solutions in HCl were measured for a range from 0.059 to -1.275 (Table 7).

Figure 11 Solution preparation of $FeCl_2$ and $FeCl_2$-HCl (acidified $FeCl_2$).

Table 7 pH values of $FeCl_2$-HCl (pH = -0.008) solutions.

Concentration of $FeCl_2$-HCl (molality)	**pH**
3	-1.275
2	-0.863
1	-0.359
0.6	-0.217
0.4	-0.118
0.2	-0.039
0.1	-0.052
0.06	0.047
0.04	-0.044
0.02	0.041
0.01	0.059
0 (1m HCl)	-0.008
0 (Water)	5.55

3.2.2 Instrumentation

3.2.2.1 Surface Tension

Surface tension measurements were carried out by using a platinum Wilhelmy plate with a Biolin Scientific Sigma 703 D force tensiometer. An acid-cleaned Petri dish was used for a series of experiment from low to high concentrations. Milli-Q water (18.2 MΩ) was first measured to calibrate the value of surface tension at certain temperature. The typical temperature and relative humidity are 20.5 °C and 25%, respectively. Measurements were averaged by triplicate experiment for all the concentrations.

3.2.2.2 UV/Visible Absorption

UV/Visible absorption experiments were carried out using a PerkinElmer Lambda 950 UV/Vis/NIR spectrometer. Absorption spectra of $FeCl_2$-HCl were taken with a quartz cuvette that referenced to Milli-Q water to a spectral range from 250 to 800 nm. Molar absorptivity was calculated by normalized to each concentration of the solutions.

3.2.2.3 Raman Scattering Spectroscopy

Unpolarized Raman spectra of samples were taken with Renishaw InVia Raman Microscope. Raman scattering measurements were carried out by using a 632.8 nm He-Ne laser (100 mW, Renishaw RL633) and a grating with 1800 lines/mm. For measuring aqueous samples in this study, 632.8 nm laser was reflected by a silver mirror and then focused by a lens with a focal length of +15 mm. The laser power before excitation is around 6 mW. Samples were measured within a 1x1 cm quartz cuvette and the laser is

focused at 2 mm from the cuvette surface to minimize the background scattering by quartz. Unpolarized Raman spectra were collected with the exposure time of 10 s/pixel and no background subtraction was employed.

3.2.2.4 Second Harmonic Generation Spectroscopy

A lab built SHG instrumentation was described previously, see the prior chapter. A femtosecond broadband Ti:sapphire laser (Tsunami, Spectra-Physics) was used with a centered wavelength at 805 nm (bandwidth of 20 nm), pulse width of sub 50 fs and the repetition rate of 82 MHz. The average output power of the laser was around 850 mW. The laser was aligned to a series of the dielectric mirrors, half-wave-plate, Glan-laser polarizer, filter, and focused on the aqueous surface with a power of 600 mW. SHG measurement was collected with p-in/p-out (perpendicular to sample surface) polarization for excitation/detection. 10% of the output power the laser was separated by a beam splitter and this laser is aligned to a reference channel to calibrate the sample signal and reduce the fluctuation from the laser. Signal photon (403 nm) was introduced to a monochromator (SR303i, Shamrock) with a slit of 0.5 mm and a grating of 300 l/mm, blazed at 500 nm. Signal of sample and reference was collected separately by an electron-multiplying CCD (EMCCD) (Newton DU970PBV, Andor) with an electron multiplication of 200. Signal was collected with an exposure time of 90 seconds and normalized by the intensity from reference channel. For further comparison of data, SHG signal was normalized by neat water to the ratio of 1.0. Each data point was averaged from three trials.

3.3 Results and Discussion

3.3.1 Surface Tension of Acidified $FeCl_2$ Solutions

Surface tension of acidified $FeCl_2$ ($FeCl_2$-HCl) provides a thermodynamic macroscopic viewpoint of the interface and is usually served as complementary information of a molecule prior to surface sensitive analysis. Generally, the surface tension of salt solutions at the air-aqueous interface have shown a positive correlation to concentration.[149] Increasing surface tension values are observed when solute is expelled from the interface.[59] In control experiments, NaCl is used as a simple halide salt and $FeCl_3$ is selected as a multivalent salt. In Figure 12, surface tension values of $FeCl_2$-HCl, $FeCl_3$ and NaCl show positive surface tension with incremental changes in slope, suggesting a negative surface excess in the following order: $FeCl_3$ (3.51 mN/m per mol/kg water)> $FeCl_2$-HCl (2.24)> NaCl (1.83). It is interesting that the surface tension increments show a positive correlation with increasing valence of the cation. A similar trend is found from Jarvis *et al.* as $Sr^{2+} > Mg^{2+} > Ba^{2+} > Na^+ > Li^+ > K^+ > NH_4^+$ in chloride solution.[150] Although surface tension of electrolytes had been studied extensively in the last decades, it is shown to differ from other surface sensitive techniques such as VSFG and XPS.[69,78,98,119,151] In this study, we used SHG spectroscopy to measure the interfacial response of $FeCl_2$-HCl solutions, and further compare to our control salt solutions to reveal new interfacial information of $FeCl_2$-HCl at the air-aqueous interface.

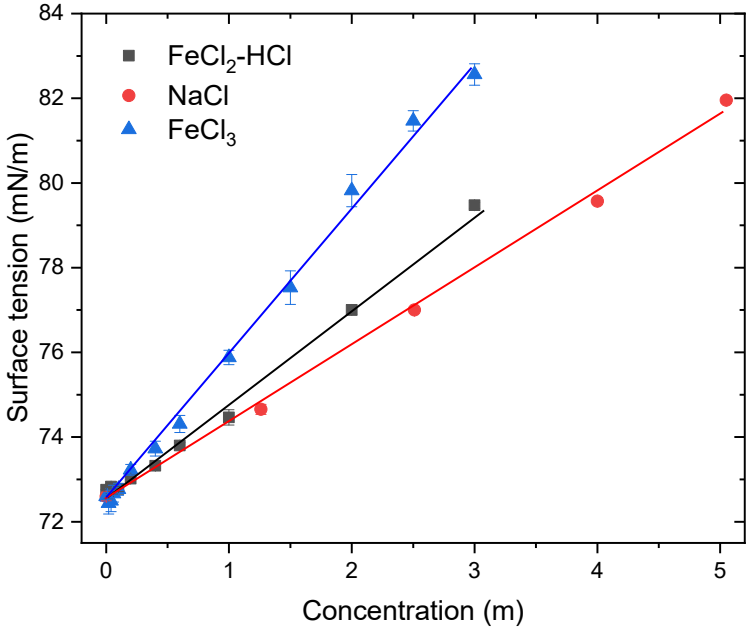

Figure 12 Surface tension of (black) $FeCl_2$-HCl, (red) NaCl, and (blue) $FeCl_3$ solutions. Lines are used to guide the eye.

3.3.2 UV/Visible Absorption of Acidified $FeCl_2$ Solutions

We sought to identify the electronic transition properties of acidified $FeCl_2$ using UV/Visible absorption measurements. Although Ferric chloride ($FeCl_3$) has been well characterized, neutral $FeCl_2$ solution is difficult to assign a UV/Visible extinction coefficient because it precipitates at low concentrations. Figure 13a exhibits UV/Visible absorption spectra of $FeCl_2$ solutions. Extinction of $FeCl_2$ is measured at 300 nm at 0.01 mol/kg water. However, precipitation of neutral $FeCl_2^0$ and hydroxides formed and caused a severe scattering in solution from 0.06 mol/kg water. In addition, the absorption band is shifted from 300 to 340 nm, however, whether the change is due to precipitation or the $FeCl_2$ solution is indistinguishable. To avoid formation of precipitation, 1 mol/kg water HCl, with pH -0.008, is used as solvent to dissolve the $FeCl_2$ powder. Figure 13b shows UV/Visible absorption spectra of acidified $FeCl_2$. We observed a consistent absorption peak at 370 nm without peak shift, implying no structural change was observed in the solution. Previously, Heinrich *et al.* examined the UV spectra of $FeCl_2$ solution and assigned the charge transfer process of $FeCl_2$ at ~40000 cm^{-1}, or ~250 nm,[54] further supported by Zhao *et al.* from their UV/Visible spectroscopic study.[147] Here we propose the UV/Visible absorption at 370 nm due to the electronic transition of $FeCl_2$ in HCl solution. We also calculated the molar absorptivity of the $FeCl_2$-HCl to compare the speciation properties to $FeCl_3$. Figure 13c shows the molar absorptivity of $FeCl_2$-HCl solution from 0.001 to 0.04 mol/kg water is around 100 $M^{-1}cm^{-1}$. The extinction coefficient of $FeCl_2$ exhibits a similar value to 60 $M^{-1}cm^{-1}$, as reported by Zhao *et al.*.[147] It is also apparent that $FeCl_2$-HCl did not show any significant changes in molar absorptivity,

implying that $FeCl_2$ does not have a diverse speciation compared to $FeCl_3$ solution. In addition, the measured molar absorptivity of $FeCl_3$ solutions at 370 nm is around 350 $M^{-1}cm^{-1}$. It is reported that $FeCl_3$ is formed via oxidation of $FeCl_2$ without HCl, but the formation of $FeCl_3$ is not likely happened in acidic conditions.[54] Thus, formation of $FeCl_3$ in the solution should be ruled out.

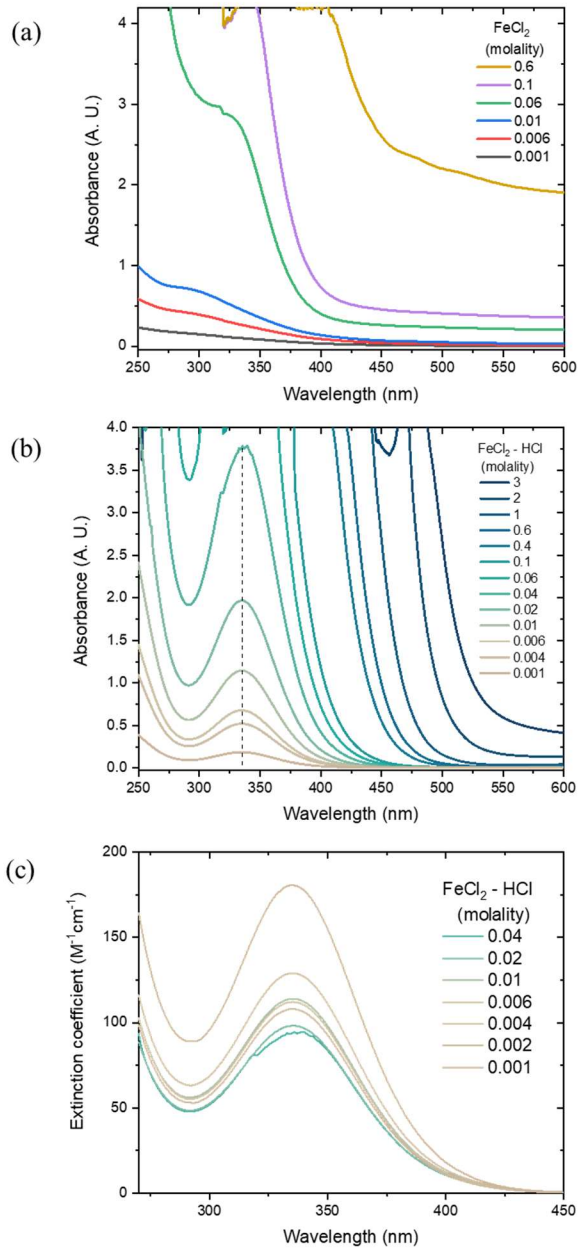

Figure 13 (a) UV/Visible absorption spectra of $FeCl_2$ solution with the presence of precipitate, (b) UV/Visible absorption spectra of $FeCl_2$-HCl solution, and (c) molar absorptivity of $FeCl_2$-HCl solution from $1x10^{-3}$ to 0.04 mol/kg water. Note that an unusual discontinuity around 320 nm is due to the change of UV/Visible light source.

3.3.3 Speciation Curves and Ion Pairing of $FeCl_2$-HCl Solution

Iron (II) chloride speciates into octahedral complexes such as $[Fe(H_2O)_6]^{2+}$, $[FeCl(H_2O)_5]^{+}$, and neutral $[FeCl_2(H_2O)_4]^{0}$. However, the formation of tetrahedral $[FeCl_4]^{2-}$ was only observed in $FeCl_2$ solutions at specific conditions such as concentrated chloride and/or at high temperature.[147,152] In this study, speciation curves of $FeCl_2$-HCl were generated using the software package, ChemEQL. The value of equilibrium constant (log$K$) for $Fe^{2+} + Cl^{-} \rightleftharpoons FeCl^{+}$ is 0.14.[134] Figure 14a exhibits speciation curves with up to 3 mol/kg water. $FeCl^{+}$ is dominant in the solution, where Fe^{2+} is around 0.01 mol/kg water. We applied the equilibrium constant, log$K$($FeCl_2^{0}$) = 6.79 x 10^{-2}, that was reported by Lee *et al.*,[52] and found that the concentration of this neutral species exists in low proportion (10% of $FeCl^{+}$) in the solution. In addition, the equilibrium constant of $FeCl_4^{2-}$ from Brugger and coworkers was fit from X-ray absorption near-edge structure spectroscopy (XANES) to produce a value of log$K$($FeCl_4^{2-}$) = -6.25. Because the equilibrium constant is relatively small for $FeCl_4^{2-}$, the speciation curve can only be observed below 10^{-5} mol/kg water. Therefore, $FeCl_4^{2-}$ is only present in solution at high $[Cl^{-}]$ and/or at high temperature.[49,144]

We also examined hydrolysis products such as $FeOH^{+}$, $Fe(OH)_2$, $Fe(OH)_3^{-}$, and $Fe(OH)_4^{2-}$, as shown in Figure 14b. Because the solution contains HCl at pH -0.008 and the concentrations of each of the hydroxides are below 10^{-12} mol/kg water, the formation of hydrolysis products is unfavorable.

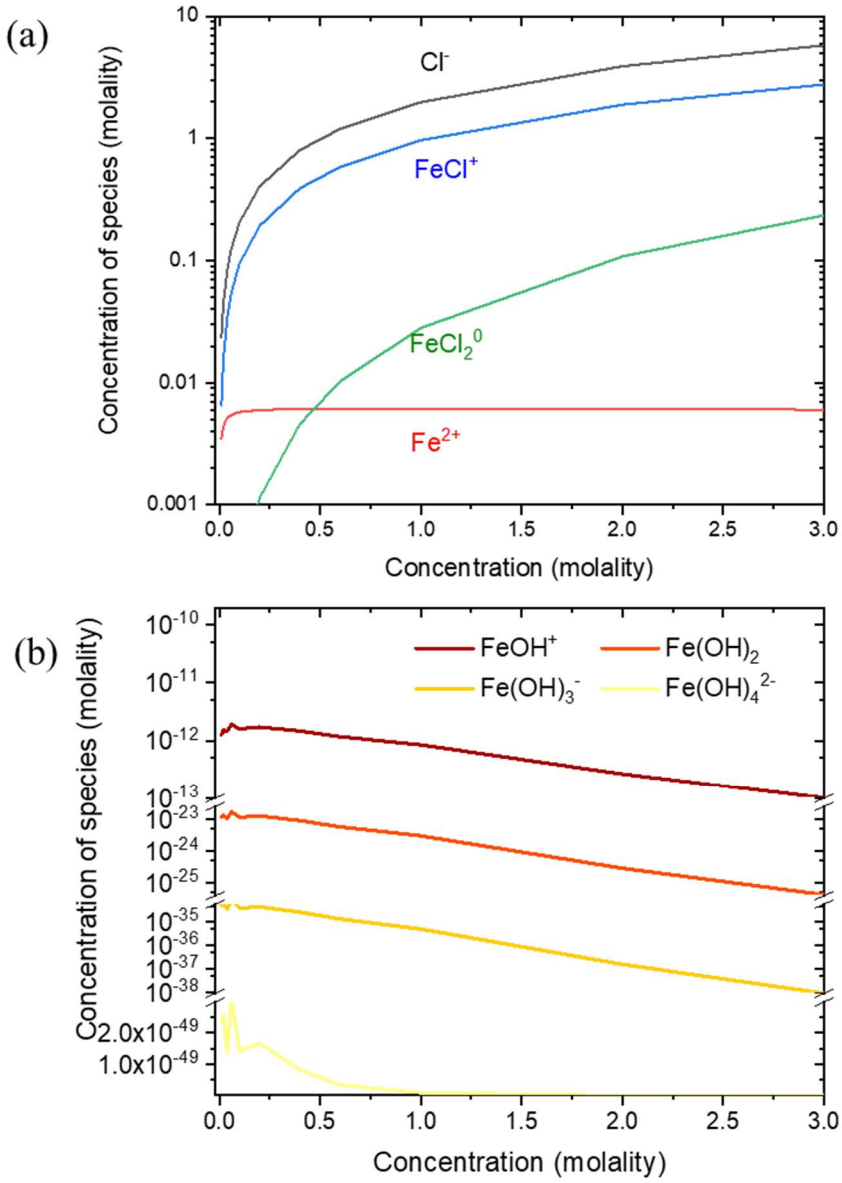

Figure 14 Speciation curves of $FeCl_2$-HCl solutions. For Fe-Cl species: (black) chloride anion, (red) Fe^{2+}, (blue) $FeCl^+$ and (green) $FeCl_2$. (b) Fe-OH species of (brown) $FeOH^+$, (red) $Fe(OH)_2$, (orange) $Fe(OH)_3^-$ and (yellow) $Fe(OH)_4^{2-}$.

3.3.4 Raman Spectra of $FeCl_2$-HCl Solution

Raman spectroscopy has literature precedence in analyzing the interaction between ions and molecules via vibrational signatures.[44,69,70] However, Raman spectroscopy at these particular $FeCl_2$-HCl solution concentrations has not been studied extensively. We measured Raman scattering spectra of $FeCl_2$-HCl solutions and compared to our control experiments of HCl and $FeCl_3$ solutions. In Figure 15a, Raman spectra of all solutions have shown characteristic features in three regions: Fe region from 300 to 500 cm^{-1}, OH bending at 1640 cm^{-1}, and OH stretching from 3000 to 3700 cm^{-1}. The first region allows us to determine the interaction by Fe-Cl stretch at 318 cm^{-1} and Fe-OH_2 stretch around 480 cm^{-1}.[44] The peak at 318 cm^{-1} confirms the existence of the $FeCl_2$ in the solution. The inset of Figure 15a shows an increase of Fe-Cl stretch at 318 cm^{-1} from 1 to 3 mol/kg water, indicating more Fe-Cl bonds formed at higher concentrations. However, there is no apparent difference in frequency shift, suggesting that the structure of the major species was not perturbed by surrounding water molecules. Fe-OH_2 stretch at around 480 cm^{-1} remains unchanged at all concentrations, indicating that the hydration environment of Fe to the surrounding water molecules is not perturbed.[44] It is interesting that each of the Fe-Cl stretch, Fe-OH_2 stretch, and OH bending vibrational modes maintain the same intensity after 2 mol/kg water. In addition, as shown in Figure 15b, no apparent change in the OH bending mode is found at 1640 cm^{-1}, suggesting that the OH bending mode is not sensitive to $FeCl_2$ and HCl solutions.

There are significant changes in Raman intensity for the OH stretch from 2800 to 3800 cm^{-1}. In Figure 15a, neat water showed three peaks centered at ~3230, ~3400, and

3630 cm^{-1}. The two main peaks at 3230 and 3400 cm^{-1} are assigned to the symmetric hydrogen-bonding network and asymmetric stretch of disordered hydrogen-bonding network.[69,153,154] The insignificant shoulder at 3630 cm^{-1} corresponds to the least hydrogen bonded water.[155,156] As a control experiment, Raman spectra of 1 and 3 mol/kg water HCl solutions indicate an enhanced Raman intensity for the OH asymmetric stretch mode, suggesting an increase in OH transition moment strength.[71] On the other hand, a decrease in intensity at 3200 cm^{-1} was observed in the control HCl experiment, which corresponds to the breaking of symmetric OH structure by introducing ions in neat water.[69,121] Difference Raman spectra in the OH stretch region were generated to compare the changes in $FeCl_2$ solutions. In Figure 15c, all acid and acidified solutions were compared to neat water spectrum. The OH stretch for the 1 to 3 mol/kg water $FeCl_2$-HCl solutions showed a simultaneous decrease in intensity for 3240, 3430 and 3630 cm^{-1}. Similarly, Wall *et al.* observed a decrease in intensity for the OH stretch band for multivalent cation species such as $CuCl_2$, $BeCl_2$, $SnCl_2$, $PrCl_3$ and $LaCl_3$.[157] Unlike the change in HCl solution, we suggest that the hydrogen-bonding network was perturbed by $FeCl_2$ because of the formation of the $FeCl_2$ hydration complex at higher concentrations.

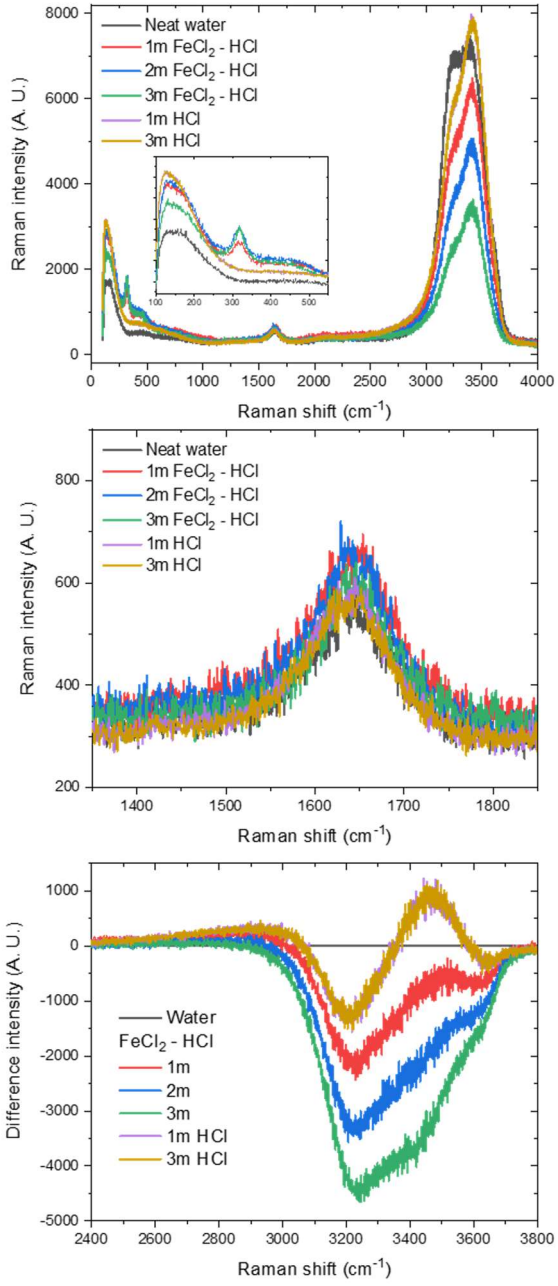

Figure 15 (a) Unpolarized Raman spectra and (b) Difference Raman spectra of $FeCl_2$-HCl and HCl. Note that the Raman spectra of 1m and 3m HCl are overlapped completely.

3.3.5 Second Harmonic Generation Spectroscopy of Acidified $FeCl_2$ Solution

Second harmonic generation (SHG) was used to identify the nonlinear response of interfacial resonant species. Here, the SHG of $FeCl_2$-HCl solutions were measured from 0.1 to 3 mol/kg water. All measured SHG intensity (I_{SHG}) is converted into SH E-field response (E_{SHG}) by the square root of its intensity. We assume that the number of resonant species in $FeCl_2$ solutions is present proportionally to the concentration of $FeCl_2$, and the fractional surface $FeCl_2$ concentration, or surface coverage (θ), is proportional to the SH E-field, as shown in Eq. 3.1.

$$\sqrt{I_{SHG}} \propto E_{SHG} \propto \chi^{(2)}_{s,eff} = \chi^{(2)}_{NR,water} + \chi^{(2)}_{R,FeCl_2} = \chi^{(2)}_{NR,water} + \chi^{(2)}_{R,FeCl_2}\theta \quad (3.1)$$

Where $\chi^{(2)}_{s,eff}$ is the second order susceptibility of total interfacial species in the solution. $\chi^{(2)}_{NR,water}$ is the nonresonant SHG response of the interfacial water molecules, $\chi^{(2)}_{R,FeCl_2}$ is the second order susceptibility of $FeCl_2$ solutions. Normalized SH E-field is obtained by dividing the SHG E-field of neat water. Then, we further simplify the equation into Eq. 3.2:

$$E_{SHG,Normalized} = 1 + B\theta \quad (3.2)$$

Where B is the constant of the ratio between resonant and nonresonant susceptibilities, $B = \chi^{(2)}_{R,FeCl_3}/\chi^{(2)}_{NR,water}$.

The trend of SHG showed a growth from low concentration and then reached the highest SHG response at around 1.2. We propose Langmuir adsorption model to fit the SHG data by using Eq. 3.3. Details of deriving the equations can refer to Chapter 2.3.4:

$$\theta = \frac{N_{S,Fe}}{N_S^{total}} = \frac{[Fe]_{Surface}}{[Fe]_{Surface}+[H_2O]_{Surface}} = \frac{K'[Fe]_{Bulk}}{1+K'[Fe]_{Bulk}} \quad (3.3)$$

Where $K' = K/[H_2O]_{Bulk} = K/55.5(M)$. K is the equilibrium constant in the following equation:

$$K = \frac{[Fe]_{Surface}[H_2O]_{Bulk}}{[Fe]_{Bulk}[H_2O]_{Surface}} = e^{\frac{-\Delta G_{ads}}{RT}} \quad (3.4)$$

Figure 16a shows the Langmuir fit to the $FeCl_2$ data in good agreement (R^2 = 0.993). The equilibrium constant K of $FeCl_2$ is 22.19 and the corresponding free energy of adsorption (ΔG_{ads}) is -1.81 kcal/mol. This finding indicates the evidence of surface adsorption of $FeCl_2$ in solution. We further compare to other salt solutions. As shown in Figure 16b, $FeCl_2$ solution revealed an anomalous trend, indicating that SHG signal was perturbed by the arbitrary distributed precipitate within the solutions. In contrast, linear trends of $FeCl_3$ and NaCl were observed in their SHG responses. As proposed in the previous chapter, the linear SHG signal of $FeCl_3$ was due to the structural ordering of nondetectable $[FeCl_2(H_2O)_4]^+$ species. Lin *et al.* also proposed the presence of $[FeCl_2(H_2O)_4]^+$ near the surface.[78] Here, SHG of NaCl solution is assigned to a nonresonant response and infers interfacial structural ordering, similarly observed by Wang and coworkers.[95] It is proposed that the electrical double layer is generated by cations and anions within the interfacial layer, and an electric field is created by charge separation. Further, the electric field alters the orientation of adjacent water molecules and causes an increased SHG intensity.[74]

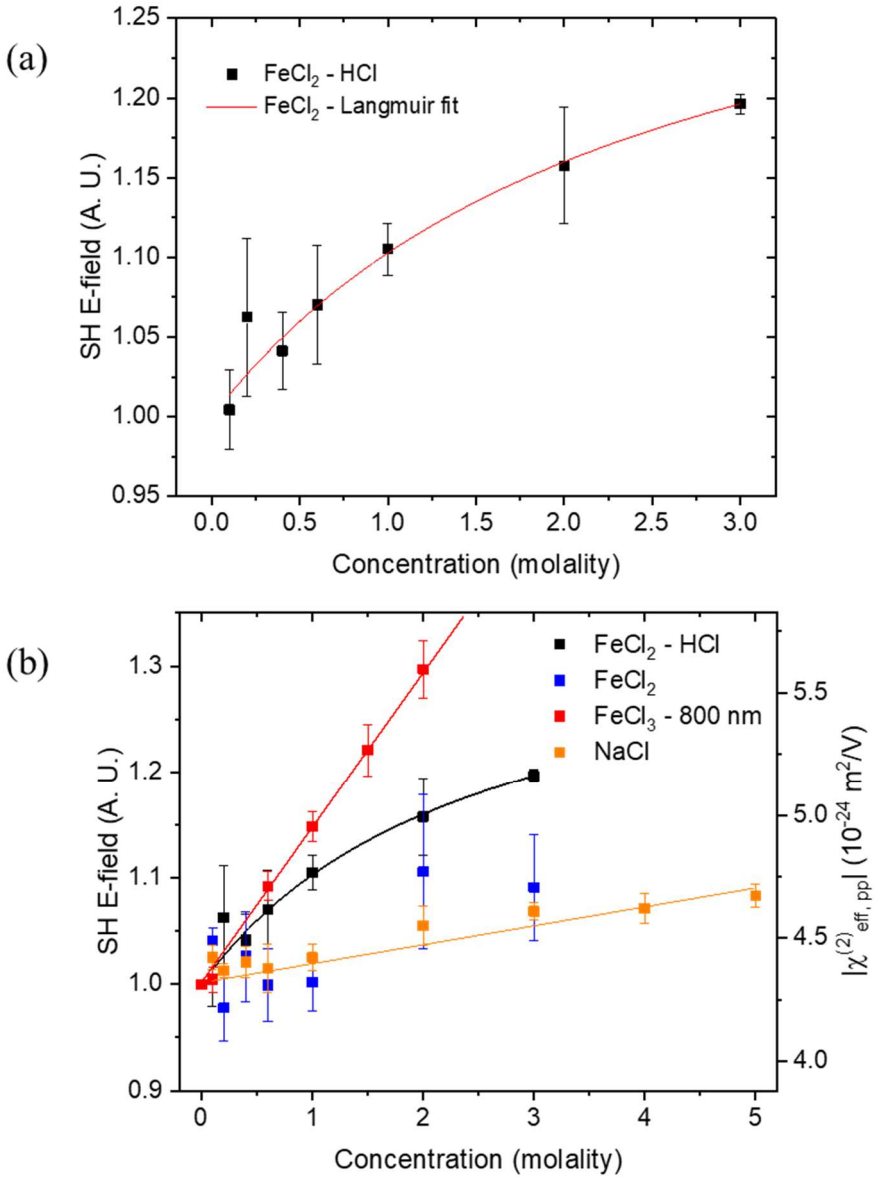

Figure 16 (a) SH electric-field of $FeCl_2$-HCl (black) and (red) data fitting with Langmuir adsorption model. (b) SH electric-field data of (black) $FeCl_2$-HCl with fitting curve, (red) $FeCl_3$ excited at 800 nm, (blue) $FeCl_2$ without acidified solution and (orange) NaCl solution.

3.3.6 Identification of Interfacial Species for Acidified $FeCl_2$ Solutions

We combine the experimental results from UV/Visible absorption and Raman measurements with the SHG data to propose the surface adsorption phenomenon. From UV/Visible measurements, single species are dominant in bulk at all concentrations which is identified by speciation curves. The speciation plot suggested that $FeCl^+$ contributes to the corresponding UV/Visible absorption at around 350 nm.

Raman scattering spectroscopy provided insights into solution structure. We observed a significant decrease in the OH stretch band and there is no proton continuum structure at the tailing of the OH band around 3000 cm^{-1}. The spectral findings suggests that $FeCl_2$ structure becomes more uniform in solution. Based on the speciation curves, we proposed that more $FeCl^+ + Cl^-$ ion pair is predominantly formed in the solution.

In addition to the presence of iron (II) ion pairs, SHG revealed an adsorption trend of $FeCl_2$-HCl. Our fitted free energy of adsorption (-1.8 kcal/mol) is similar to the adsorption of NaI (-0.8 kcal/mol), as suggested by Petersen *et al.*.[74] However, Bruce *et al.* reported that Fe-Cl species prefer bulk solvation when complexation of Fe-Cl complexes are formed.[82] Although our results contradict with Bruce *et al*, the intrinsic differences between the two solution systems may be the reason for this inconsistency.

3.3.7 Conclusion

Systematic studies of acidified $FeCl_2$ solutions reveal the surface adsorption of $FeCl_2$ species from $FeCl_2$-HCl solution to the air-aqueous interface. Speciation data from $FeCl_2$ informs on surface iron (II). Iron exhibits a primary species, more than 90 mole %,

from metal-ligand charge transfer in UV/Visible absorption measurements, $FeCl^{+}$. Breaking of the hydrogen bonding network in solution was observed in Raman spectroscopy. Preferential adsorption of $FeCl^{+}$ species is revealed from the SHG measurements and fitting of the square root of the SHG data to a Langmuir adsorption model.

Chapter 4. Conclusion and Future Perspective

This dissertation reported the observation and proposed species of iron (III) and iron (II) complexes at air-aqueous interface. A systematic evaluation of iron chloride solutions is tested with different techniques.

UV/Visible spectra of iron (III) chloride solutions showed various absorbance, and the molar absorptivity varies at high concentrations, suggesting that the iron speciation is verified by ligand-to-metal charge transfer process at 350 nm. Speciation curves of iron (III) chloride were generated with pH values from 3.7 to -1.62 and showed a positive correlation to the increased molar absorptivity. Calculation of dipole moment suggested that $[FeCl(H_2O)_5]^{2+}$ and $[FeCl_3(H_2O)_3]$ possess permanent dipole. Furthermore, based on our molar absorptivity data, $[FeCl(H_2O)_5]^{2+}$ showed no absorption around 400 nm, meaning that $[FeCl(H_2O)_5]^{2+}$ is not resonantly enhanced by SHG. In SHG experiments, at mmol/kg water level, $FeCl_3$ solutions showed destructive interference to the water dipole, or due to its high refractive index, causing a decrease in SHG E-field. At medium concentration (below 3 mol/kg water), SHG of $FeCl_3$ excited at 800 and 860 nm showed a good fitting result by FFG adsorption model ($R^2 \sim 0.995$). The value of free energy of adsorption is around -0.55 kcal/mol, suggesting a weak adsorption on surface. Also, fitted interaction energy indicated an attractive interaction between iron complexes. For the SHG data excited at 760 nm, SHG of $FeCl_3$ exhibited an increment of E-field with increased concentration. With the similarity to control experiments of halide solutions, we propose the linear trend is because of the SHG nonresonant Fe-Cl species. At the middle concentration (0.6 to 3 mol/kg water), the presence of $[FeCl(H_2O)_5]^{2+}$ and $[FeCl_2(H_2O)_4]^{+}$,

was suggested and those Fe-Cl complexes performed a structural ordering at the interface. From 3 to 5 mol/kg water, the second slope has around 7-fold to the first slope. The second trend is proposed to be a different structural ordering effect, and it is because of the adsorption of $[FeCl_3(H_2O)_3]$ on surface. Besides, we proposed that $[FeCl_4]^-$ contributes to the increase of SH E-field response. From our calculation of hydration number of water molecules, it is expected that the surrounding water molecules are not sufficient to maintain a full hydration shell at high concentrations of $FeCl_3$. As a result, we proposed that the speciation still occurs at the $FeCl_3$ aqueous interface.

In addition to $FeCl_3$, acidified iron (II) chloride solution exhibited a relatively simpler trend. Molar absorptivity from UV/Visible spectra does not change with concentration, suggesting that there is no speciation in the solution. Additionally, speciation curves indicated that the primary iron (II) complex is $[FeCl(H_2O)_5]^+$, and less than 10% belongs to the neutral $[FeCl_2(H_2O)_4]$. Raman scattering spectra showed a significant decrease in Raman intensity of symmetric and asymmetric OH stretch, implying that the hydrogen-bonding network is broken. Additionally, data of SHG of acidified $FeCl_2$ solutions followed the Langmuir adsorption model. A free energy of adsorption fitted by the model is -1.8 kcal/mol, suggesting the adsorption of $FeCl_2$-HCl is more favorable than $FeCl_3$ species. It is worth noting that, due to being symmetrical and low concentration in speciation, $[FeCl_2(H_2O)_4]$ is not expected to contribute to the Langmuir adsorption behavior on surface. As a result, adsorption of $[FeCl(H_2O)_5]^+$ to the aqueous surface is proposed.

Compared to the results of our surface tension experiments, SHG measurments suggest that both $FeCl_3$ and acidified $FeCl_2$ species are preferentially adsorbed on surface. These contradictory results reenforced the fact that surface tension assays are more suitable for measuring macroscopic force of molecules, while SHG is more sensitive at detecting interfacial response of molecules.

Although our work has showed the presence of iron (III) and iron (II) chloride at the aqueous interface, knowledge on analyzing a single interfacial species that can be isolated by experimental control from solution is still lacking. Hence, future direction to this project can be selectively monitor less iron species by modifying experiment conditions. Additionally, variables/conditions such as pH value, temperature, and the ratio of Fe:Cl in solutions could all be manipulated and examined as they may provide different outcomes. For example, (1) adjusting pH values of solution might perturb the equilibrium of Fe complexes, hence by gradually adjusting the pH, SHG response is possible to assign the Fe species by comparing the trend. (2) It is known that temperature affects the concentration of Fe complexes, thus changing the temperature can detect one major species. For instance, $FeCl_2^+$ is dominant at 1.5 mol/kg water at 25 ºC, whereas the most abundant $FeCl_2^+$ is shifted to 0.7 mol/kg water at 90 ºC. (3) Modifying the Fe:Cl ratio is beneficial for specific complex such as $FeCl_4^-$, as it is indicated that $FeCl_4^-$ occurs at high Cl^- concentration. By keeping the concentration of iron at constant, interfacial response of $FeCl_4^-$ can be monitored. Lastly, we can also broaden our insights on preferential adsorption of the anion identity by testing different halide identities. For example, future studies could compare the interfacial response between Cl^-, Br^-, and I^-. It is reported that

largely polarizable anions such as Br^- and I^- contributes stronger SHG response in halide solutions. However, it is needed to confirm the speciation of Fe-halide complexes.

In conclusion, we showed for the first time that the adsorption behavior of iron (III) and iron (II) chloride species were observed by SHG within aqueous interfaces. Furthermore, with the supporting evidence from UV/Visible absorption and Raman spectroscopy, our SHG results suggest the complexity of species on iron (III) chloride surface and adsorption of $[FeCl(H_2O)_5]^+$ on aqueous iron (II) chloride surface. These studies provide an example of understanding the interfacial complexity and adsorption of multivalent cations on aqueous surface.

Bibliography

(1) McDonough, W. F.; Sun, S. -s. Composition of the Earth. *Physics of the Earth*. 1995, pp 223–253. https://doi.org/10.1017/cbo9780511812910.003.

(2) Allègre, C. J.; Poirier, J. P.; Humler, E.; Hofmann, A. W. The Chemical Composition of the Earth. *Earth Planet. Sci. Lett.* **1995**, *134* (3–4), 515–526. https://doi.org/10.1016/0012-821X(95)00123-T.

(3) Fleischhacker, A. S.; Kiley, P. J. Iron-Containing Transcription Factors and Their Roles as Sensors. *Curr. Opin. Chem. Biol.* **2011**, *15* (2), 335–341. https://doi.org/10.1016/j.cbpa.2011.01.006.

(4) Jickells, T. D.; An, Z. S.; Andersen, K. K.; Baker, A. R.; Bergametti, C.; Brooks, N.; Cao, J. J.; Boyd, P. W.; Duce, R. A.; Hunter, K. A.; Kawahata, H.; Kubilay, N.; LaRoche, J.; Liss, P. S.; Mahowald, N.; Prospero, J. M.; Ridgwell, A. J.; Tegen, I.; Torres, R. Global Iron Connections between Desert Dust, Ocean Biogeochemistry, and Climate. *Science (80-.).* **2005**, *308* (5718), 67–71. https://doi.org/10.1126/science.1105959.

(5) Wang, R.; Balkanski, Y.; Boucher, O.; Bopp, L.; Chappell, A.; Ciais, P.; Hauglustaine, D.; Peñuelas, J.; Tao, S. Sources, Transport and Deposition of Iron in the Global Atmosphere. *Atmos. Chem. Phys.* **2015**, *15* (11), 6247–6270. https://doi.org/10.5194/acp-15-6247-2015.

(6) Mahowald, N. M.; Engelstaedter, S.; Luo, C.; Sealy, A.; Artaxo, P.; Benitez-Nelson, C.; Bonnet, S.; Chen, Y.; Chuang, P. Y.; Cohen, D. D.; Dulac, F.; Herut, B.; Johansen, A. M.; Kubilay, N.; Losno, R.; Maenhaut, W.; Paytan, A.; Prospero, J. M.; Shank, L. M.; Siefert, R. L. Atmospheric Iron Deposition: Global Distribution, Variability, and Human Perturbations. *Ann. Rev. Mar. Sci.* **2009**, *1*, 245–278. https://doi.org/10.1146/annurev.marine.010908.163727.

(7) Nickovic, S.; Vukovic, A.; Vujadinovic, M. Atmospheric Processing of Iron Carried by Mineral Dust. *Atmos. Chem. Phys.* **2013**, *13* (18), 9169–9181. https://doi.org/10.5194/acp-13-9169-2013.

(8) Street, J. H.; Paytan, A. Iron, Phytoplankton Growth, and the Carbon Cycle. *Met. Ions Biol. Syst.* **2005**, *43*, 153–193. https://doi.org/10.1201/9780824751999.CH7.

(9) Tagliabue, A.; Bowie, A. R.; Boyd, P. W.; Buck, K. N.; Johnson, K. S.; Saito, M. A. The Integral Role of Iron in Ocean Biogeochemistry. *Nature* **2017**, *543* (7643), 51–59. https://doi.org/10.1038/nature21058.

(10) Winterbourn, C. C. *The Biological Chemistry of Hydrogen Peroxide*, 1st ed.; Elsevier Inc., 2013; Vol. 528. https://doi.org/10.1016/B978-0-12-405881-1.00001-X.

(11) White, E. M.; Vaughan, P. P.; Zepp, R. G. Role of the Photo-Fenton Reaction in the Production of Hydroxyl Radicals and Photobleaching of Colored Dissolved Organic Matter in a Coastal River of the Southeastern United States. *Aquat. Sci.* **2003**, *65* (4), 402–414. https://doi.org/10.1007/s00027-003-0675-4.

(12) Ensing, B.; Buda, F.; Baerends, E. J. Fenton-like Chemistry in Water: Oxidation Catalysis by Fe(III) and H2O2. *J. Phys. Chem. A* **2003**, *107* (30), 5722–5731.

https://doi.org/10.1021/jp0267149.
(13) Teixeira, A. P. C.; Tristão, J. C.; Araujo, M. H.; Oliveira, L. C. A.; Moura, F. C. C.; Ardisson, J. D.; Amorim, C. C.; Lago, R. M. Iron: A Versatile Element to Produce Materials for Environmental Applications. *J. Braz. Chem. Soc.* **2012**, *23* (9), 1579–1593. https://doi.org/10.1590/S0103-50532012005000039.
(14) • Iron ore consumption worldwide 2010-2019 | Statista https://www.statista.com/statistics/1168853/apparent-iron-ore-consumption-worldwide/ (accessed Mar 16, 2022).
(15) Iron Ore Statistics and Information | U.S. Geological Survey https://www.usgs.gov/centers/national-minerals-information-center/iron-ore-statistics-and-information (accessed Mar 16, 2022).
(16) Martínez-Huitle, C. A.; Scialdone, O.; Rodrigo, M. A. *Electrochemical Water and Wastewater Treatment*; Elsevier Science, 2018. https://doi.org/10.1016/C2016-0-04297-3.
(17) Luo, H.; Zeng, Y.; He, D.; Pan, X. Application of Iron-Based Materials in Heterogeneous Advanced Oxidation Processes for Wastewater Treatment: A Review. *Chem. Eng. J.* **2021**, *407* (September 2020), 127191. https://doi.org/10.1016/j.cej.2020.127191.
(18) Bizzo, W. A.; Figueiredo, R. A.; De Andrade, V. F. Characterization of Printed Circuit Boards for Metal and Energy Recovery after Milling and Mechanical Separation. *Materials (Basel).* **2014**, *7* (6), 4555–4566. https://doi.org/10.3390/ma7064555.
(19) Kobayashi, S.; Makino, A. Enzymatic Polymer Synthesis: An Opportunity for Green Polymer Chemistry. *Chem. Rev.* **2009**, *109* (11), 5288–5353. https://doi.org/10.1021/CR900165Z.
(20) Xu, C.; Xu, K.; Gu, H.; Zheng, R.; Liu, H.; Zhang, X.; Guo, Z.; Xu, B. Dopamine as A Robust Anchor to Immobilize Functional Molecules on the Iron Oxide Shell of Magnetic Nanoparticles. **2004**. https://doi.org/10.1021/ja0464802.
(21) Zürcher, S.; Wäckerlin, D.; Bethuel, Y.; Malisova, B.; Textor, M.; Tosatti, S.; Gademann, K. Biomimetic Surface Modifications Based on the Cyanobacterial Iron Chelator Anachelin. *J. AM. CHEM. SOC* **2006**, *128*, 1064–1065. https://doi.org/10.1021/ja056256s.
(22) Al-Abadleh, H. A. Review of the Bulk and Surface Chemistry of Iron in Atmospherically Relevant Systems Containing Humic-like Substances. *RSC Adv.* **2015**, *5* (57), 45785–45811. https://doi.org/10.1039/c5ra03132j.
(23) Sisso, O.; Dor, S.; Eliyahu, D.; Sabatani, E.; Eliaz, N. Corrosion Inhibition of Copper in Ferric Chloride Solutions with Organic Inhibitors. *npj Mater. Degrad.* **2020**, *4* (1). https://doi.org/10.1038/s41529-020-00139-0.
(24) Pouliquen, D.; Le Jeune, J. J.; Perdrisot, R.; Ermias, A.; Jallet, P. Iron Oxide Nanoparticles for Use as an MRI Contrast Agent: Pharmacokinetics and Metabolism. *Magn. Reson. Imaging* **1991**, *9* (3), 275–283. https://doi.org/10.1016/0730-725X(91)90412-F.
(25) Ali, A.; Zafar, H.; Zia, M.; ul Haq, I.; Phull, A. R.; Ali, J. S.; Hussain, A.

Synthesis, Characterization, Applications, and Challenges of Iron Oxide Nanoparticles. *Nanotechnol. Sci. Appl.* **2016**, *9*, 49. https://doi.org/10.2147/NSA.S99986.
(26) Lemire, J. A.; Harrison, J. J.; Turner, R. J. Antimicrobial Activity of Metals: Mechanisms, Molecular Targets and Applications. *Nat. Rev. Microbiol.* **2013**, *11* (6), 371–384. https://doi.org/10.1038/nrmicro3028.
(27) Estelrich, J.; Escribano, E.; Queralt, J.; Busquets, M. A. Iron Oxide Nanoparticles for Magnetically-Guided and Magnetically-Responsive Drug Delivery. *Int. J. Mol. Sci.* **2015**, *16* (4), 8070. https://doi.org/10.3390/IJMS16048070.
(28) Cotton, S. A. Iron(III) Chloride and Its Coordination Chemistry. *J. Coord. Chem.* **2018**, *71* (21), 3415–3443. https://doi.org/10.1080/00958972.2018.1519188.
(29) Cotton, F. A. A Millennial Overview of Transition Metal Chemistry. *J. Chem. Soc. Dalt. Trans.* **2000**, No. 13, 1961–1968. https://doi.org/10.1039/b001668n.
(30) Bock, R.; Kleinsteinberg, B.; Selnes-Volseth, B.; Burheim, O. S. A Novel Iron Chloride Red-Ox Concentration Flow Cell Battery (Icfb) Concept; Power and Electrode Optimization. *Energies* **2021**, *14* (4), 1–12. https://doi.org/10.3390/en14041109.
(31) Manohar, A. K.; Kim, K. M.; Plichta, E.; Hendrickson, M.; Rawlings, S.; Narayanan, S. R. A High Efficiency Iron-Chloride Redox Flow Battery for Large-Scale Energy Storage. *J. Electrochem. Soc.* **2016**, *163* (1), A5118–A5125. https://doi.org/10.1149/2.0161601jes.
(32) Clemente, A.; Costa-Castelló, R. Redox Flow Batteries: A Literature Review Oriented to Automatic Control. *Energies* **2020**, *13* (17), 1–31. https://doi.org/10.3390/en13174514.
(33) Zhang, H.; Sun, C. Cost-Effective Iron-Based Aqueous Redox Flow Batteries for Large-Scale Energy Storage Application: A Review. *J. Power Sources* **2021**, *493* (July 2020). https://doi.org/10.1016/j.jpowsour.2020.229445.
(34) McGrath, M. J.; Patterson, N.; Manubay, B. C.; Hardy, S. H.; Malecha, J. J.; Shi, Z.; Yue, X.; Xing, X.; Funke, H. H.; Gin, D. L.; Liu, P.; Noble, R. D. 110th Anniversary: The Dehydration and Loss of Ionic Conductivity in Anion Exchange Membranes Due to FeCl4- Ion Exchange and the Role of Membrane Microstructure. *Ind. Eng. Chem. Res.* **2019**, *58* (49), 22250–22259. https://doi.org/10.1021/acs.iecr.9b04592.
(35) Reinen, D. The Correlation between Structure and Color of Iron Oxide-Type Solids, Sustainable Pigments with Gentle Hues. *Zeitschrift für Anorg. und Allg. Chemie* **2014**, *640* (14), 2677–2683. https://doi.org/10.1002/ZAAC.201400384.
(36) Stefansson, A.; Lemke, K. H.; Seward, T. M. Iron (III) Complexation in Hydrothermal Solutions - an Experimental and Theoretical Study. *Proc. 15th Int. Conf. Prop. Water Steam* **2008**, No. Iii.
(37) Rabinowitch, E.; Stockmayer, W. H. Association of Ferric Ions with Chloride, Bromide and Hydroxyl Ions (A Spectroscopic Study). *J. Am. Chem. Soc.* **1942**, *64* (2), 335–347. https://doi.org/10.1021/ja01254a034.
(38) Gamlen, A.; Jordan, D. A Spectrophotonzetric Study of the Iron(III) Chloro-

Complexes. *J. Chem. Soc.* **1953**, *75*, 1435–1443.
(39) Marcus, Y. The Anion Exchange of Metal Complexes-IV. The Iron(III)-Chloride System. *J. Inorg. Nucl. Chem.* **1960**, *12* (3–4), 287–296. https://doi.org/10.1016/0022-1902(60)80375-2.
(40) Byrne, R. H.; Kester, D. R. Ultraviolet Spectroscopic Study of Ferric Equilibria at High Chloride Concentrations. *J. Solution Chem.* **1981**, *10* (1), 51–67. https://doi.org/10.1007/BF00652780.
(41) Flynn, C. M. Hydrolysis of Inorganic Iron(III) Salts. *Chem. Rev.* **1984**, *84* (1), 31–41. https://doi.org/10.1021/cr00059a003.
(42) Marston, A. L.; Bush, S. F. Raman Spectral Investigation of the Complex Species of Ferric Chloride in Concentrated Aqueous Solution. *Appl. Spectrosc.* **1972**, *26* (6), 579–584. https://doi.org/10.1366/000370272774351732.
(43) Kanno, H.; Hiraishi, J. A Raman Study of Aqueous Solutions of Ferric Nitrate, Ferrous Chloride and Ferric Chloride in the Glassy State. *J. Raman Spectrosc.* **1982**, *12* (3), 224–227. https://doi.org/10.1002/jrs.1250120305.
(44) Baumler, S. M.; Hartt, W. H.; Allen, H. C. Hydration of Ferric Chloride and Nitrate in Aqueous Solutions: Water-Mediated Ion Pairing Revealed by Raman Spectroscopy. *Phys. Chem. Chem. Phys.* **2019**, *21* (35), 19172–19180. https://doi.org/10.1039/c9cp01392j.
(45) Brady, G. W.; Robin, M. B.; Varimbi, J. The Structure of Ferric Chloride in Neutral and Acid Solutions. *Inorg. Chem.* **1964**, *3* (8), 1168–1173. https://doi.org/10.1021/ic50018a023.
(46) Brubaker, G. R.; Peterson, R. A. Stability of the Monochloroiron(III) Cation in Aqueous Solutions between 298 and 398 K. *Inorganica Chim. Acta* **1989**, *155* (1), 139–144. https://doi.org/10.1016/S0020-1693(00)89293-2.
(47) Stefánsson, A. Iron (III) Hydrolysis and Solubility at 25 Degrees C. *Environ. Sci. Technol.* **2007**, *41* (17), 6117–61123.
(48) Liu, W.; Etschmann, B.; Brugger, J.; Spiccia, L.; Foran, G.; McInnes, B. UV-Vis Spectrophotometric and XAFS Studies of Ferric Chloride Complexes in Hyper-Saline LiCl Solutions at 25-90 °C. *Chem. Geol.* **2006**, *231* (4), 326–349. https://doi.org/10.1016/j.chemgeo.2006.02.005.
(49) Liu, W.; Etschmann, B.; Foran, G.; Shelley, M.; Brugger, J. Deriving Formation Constants for Aqueous Metal Complexes from XANES Spectra: Zn2+ and Fe2+ Chloride Complexes in Hypersaline Solutions. *Am. Mineral.* **2007**, *92* (5–6), 761–770. https://doi.org/10.2138/am.2007.2225.
(50) Stefánsson, A.; Lemke, K. H.; Seward, T. M. Iron(III) Chloride Complexation in Hydrothermal Solutions: A Combined Spectrophotometric and Density Functional Theory Study. *Chem. Geol.* **2019**, *524*, 77–87. https://doi.org/10.1016/j.chemgeo.2019.05.039.
(51) Palmer, D. A.; Hyde, K. E. An Experimental Determination of Ferrous Chloride and Acetate Complexation in Aqueous Solutions to 300°C. *Geochim. Cosmochim. Acta* **1993**, *57* (7), 1393–1408. https://doi.org/10.1016/0016-7037(93)90001-D.
(52) Lee, M. S. Chemical Equilibria in Ferrous Chloride Acid Solution. *Met. Mater. Int.*

2004, *10* (4), 387–392. https://doi.org/10.1007/BF03185990.
(53) Luin, U.; Arčon, I.; Valant, M. Structure and Population of Complex Ionic Species in FeCl2 Aqueous Solution by X-Ray Absorption Spectroscopy. *Molecules* **2022**, *27* (3), 1–13. https://doi.org/10.3390/molecules27030642.
(54) Heinrich, C. A.; Seward, T. M. A Spectrophotometric Study of Aqueous Iron (II) Chloride Complexing from 25 to 200°C. *Geochim. Cosmochim. Acta* **1990**, *54* (8), 2207–2221. https://doi.org/10.1016/0016-7037(90)90046-N.
(55) Fein, J. B.; Hemley, J. J.; D'Angelo, W. M.; Komninou, A.; Sverjensky, D. A. Experimental Study of Iron-Chloride Complexing in Hydrothermal Fluids. *Geochim. Cosmochim. Acta* **1992**, *56* (8), 3179–3190. https://doi.org/10.1016/0016-7037(92)90296-U.
(56) Sweeton, F. H.; Baes, C. F. The Solubility of Magnetite and Hydrolysis of Ferrous Ion in Aqueous Solutions at Elevated Temperatures. *J. Chem. Thermodyn.* **1970**, *2* (4), 479–500. https://doi.org/10.1016/0021-9614(70)90098-4.
(57) Baes, C. F.; Mesmer, R. E. *The Hydrolysis of Cations*; Wiley,: New York :, 1976.
(58) Schwaab, G.; Sebastiani, F.; Havenith, M. Ion Hydration and Ion Pairing as Probed by THz Spectroscopy. *Angew. Chemie - Int. Ed.* **2019**, *58* (10), 3000–3013. https://doi.org/10.1002/anie.201805261.
(59) Adamson, A. W.; Gast, A. P. *Physical Chemistry of Surfaces*, Sixth Edit.; Wiley-Interscience, 1997.
(60) Durand-Vidal, S.; Simonin, J.-P.; Turq, P. *Electrolytes at Interfaces*; Springer Netherlands, 2002.
(61) Fawcett, W. R. *Liquids, Solutions, and Interfaces*; Oxford University Press, 2004. https://doi.org/10.1093/oso/9780195094329.001.0001.
(62) Petersen, P. B.; Johnson, J. C.; Knutsen, K. P.; Saykally, R. J. Direct Experimental Validation of the Jones-Ray Effect. *Chem. Phys. Lett.* **2004**, *397* (1–3), 46–50. https://doi.org/10.1016/j.cplett.2004.08.048.
(63) Petersen, P. B.; Saykally, R. J. On the Nature of Ions At the Liquid Water Surface. *Annu. Rev. Phys. Chem.* **2006**, *57* (1), 333–364. https://doi.org/10.1146/annurev.physchem.57.032905.104609.
(64) Hu, J. H.; Shi, Q.; Davidovits, P.; Worsnop, D. R.; Zahniser, M. S.; Kolb, C. E. Reactive Uptake of Cl2(g) and Br2(g) by Aqueous Surfaces as a Function of Br- and I- Ion Concentration. The Effect of Chemical Reaction at the Interface. *J. Phys. Chem.* **1995**, *99* (21), 8768–8776. https://doi.org/10.1021/j100021a050.
(65) Jungwirth, P.; Curtis, J. E.; Tobias, D. J. Polarizability and Aqueous Solvation of the Sulfate Dianion. *Chem. Phys. Lett.* **2003**, *367* (5–6), 704–710. https://doi.org/10.1016/S0009-2614(02)01782-7.
(66) Jungwirth, P.; Tobias, D. J. Specific Ion Effects at the Air/Water Interface. *Chem. Rev.* **2006**, *106* (4), 1259–1281. https://doi.org/10.1021/cr0403741.
(67) Jungwirth, P.; Tobias, D. J. Molecular Structure of Salt Solutions: A New View of the Interface with Implications for Heterogeneous Atmospheric Chemistry. *J. Phys. Chem. B* **2001**, *105* (43), 10468–10472. https://doi.org/10.1021/jp012750g.
(68) Mucha, M.; Frigato, T.; Levering, L. M.; Allen, H. C.; Tobias, D. J.; Dang, L. X.;

Jungwirth, P. Unified Molecular Picture of the Surfaces of Aqueous Acid, Base, and Salt Solutions. *J. Phys. Chem. B* **2005**, *109* (16), 7617–7623. https://doi.org/10.1021/jp0445730.

(69) Liu, D.; Ma, G.; Levering, L. M.; Allen, H. C. Vibrational Spectroscopy of Aqueous Sodium Halide Solutions and Air-Liquid Interfaces: Observation of Increased Interfacial Depth. *J. Phys. Chem. B* **2004**, *108* (7), 2252–2260. https://doi.org/10.1021/jp036169r.

(70) Xu, M.; Larentzos, J. P.; Roshdy, M.; Criscenti, L. J.; Allen, H. C. Aqueous Divalent Metal-Nitrate Interactions: Hydration versus Ion Pairing. *Phys. Chem. Chem. Phys.* **2008**, *10* (32), 4793–4801. https://doi.org/10.1039/b807090n.

(71) Huang, Z.; Hua, W.; Verreault, D.; Allen, H. C. Salty Glycerol versus Salty Water Surface Organization: Bromide and Iodide Surface Propensities. *J. Phys. Chem. A* **2013**, *117* (29), 6346–6353. https://doi.org/10.1021/jp4020228.

(72) Petersen, P. B.; Saykally, R. J. Confirmation of Enhanced Anion Concentration at the Liquid Water Surface. *Chem. Phys. Lett.* **2004**, *397* (1–3), 51–55. https://doi.org/10.1016/j.cplett.2004.08.049.

(73) Petersen, P. B.; Saykally, R. J.; Mucha, M.; Jungwirth, P. Enhanced Concentration of Polarizable Anions at the Liquid Water Surface: SHG Spectroscopy and MD Simulations of Sodium Thiocyanide. *J. Phys. Chem. B* **2005**, *109* (21), 10915–10921. https://doi.org/10.1021/jp050864c.

(74) Petersen, P. B.; Saykally, R. J. Probing the Interfacial Structure of Aqueous Electrolytes with Femtosecond Second Harmonic Generation Spectroscopy. *J. Phys. Chem. B* **2006**, *110* (29), 14060–14073. https://doi.org/10.1021/jp0601825.

(75) Otten, D. E.; Petersen, P. B.; Saykally, R. J. Observation of Nitrate Ions at the Air/Water Interface by UV-Second Harmonic Generation. *Chem. Phys. Lett.* **2007**, *449* (4–6), 261–265. https://doi.org/10.1016/j.cplett.2007.10.081.

(76) Petersen, P. B.; Saykally, R. J. Is the Liquid Water Surface Basic or Acidic? Macroscopic vs. Molecular-Scale Investigations. *Chem. Phys. Lett.* **2008**, *458* (4–6), 255–261. https://doi.org/10.1016/j.cplett.2008.04.010.

(77) Ghosal, S.; Brown, M. A.; Bluhm, H.; Krisch, M. J.; Salmeron, M.; Jungwirth, P.; Hemminger, J. C. Ion Partitioning at the Liquid/Vapor Interface of a Multicomponent Alkali Halide Solution: A Model for Aqueous Sea Salt Aerosols. *J. Phys. Chem. A* **2008**, *112* (48), 12378–12384. https://doi.org/10.1021/jp805490f.

(78) Lin, L.; Husek, J.; Biswas, S.; Baumler, S. M.; Adel, T.; Ng, K. C.; Baker, L. R.; Allen, H. C. Iron(III) Speciation Observed at Aqueous and Glycerol Surfaces: Vibrational Sum Frequency and X-Ray. *J. Am. Chem. Soc.* **2019**, *141* (34), 13525–13535. https://doi.org/10.1021/jacs.9b05231.

(79) Brandes, E.; Karageorgiev, P.; Viswannath, P.; Motschmann, H. Breaking the Symmetry of Ions at the Air-Water Interface. *J. Phys. Chem. C* **2014**, *118*, 26629–26633.

(80) Thürmer, S.; Seidel, R.; Eberhardt, W.; Bradforth, S. E.; Winter, B. Ultrafast Hybridization Screening in Fe3+ Aqueous Solution. *J. Am. Chem. Soc.* **2011**, *133* (32), 12528–12535. https://doi.org/10.1021/ja200268b.

(81) Seidel, R.; Kraffert, K.; Kabelitz, A.; Pohl, M. N.; Kraehnert, R.; Emmerling, F.; Winter, B. Detection of the Electronic Structure of Iron-(III)-Oxo Oligomers Forming in Aqueous Solutions. *Phys. Chem. Chem. Phys.* **2017**, *19* (48), 32226–32234. https://doi.org/10.1039/c7cp06945f.

(82) Bruce, J. P.; Hemminger, J. C. Characterization of Fe2+ Aqueous Solutions with Liquid Jet X-Ray Photoelectron Spectroscopy: Chloride Depletion at the Liquid/Vapor Interface Due to Complexation with Fe2+. *J. Phys. Chem. B* **2019**, *123* (39), 8285–8290. https://doi.org/10.1021/acs.jpcb.9b06515.

(83) Durrant, M. C. Transition Metal Chemistry; Past, Present and Future. *Transit. Met. Chem.* **2019**, *44* (1), 1–3. https://doi.org/10.1007/s11243-019-00306-6.

(84) Malinowski, J.; Zych, D.; Jacewicz, D.; Gawdzik, B.; Drzeżdżon, J. Application of Coordination Compounds with Transition Metal Ions in the Chemical Industry—a Review. *Int. J. Mol. Sci.* **2020**, *21* (15), 1–26. https://doi.org/10.3390/ijms21155443.

(85) Root, C.; Presume, H.; Proudfoot, D.; Willis, L.; Masiello, R. Using Battery Energy Storage to Reduce Renewable Resource Curtailment. *2017 IEEE Power Energy Soc. Innov. Smart Grid Technol. Conf. ISGT 2017* **2017**, 1–5. https://doi.org/10.1109/ISGT.2017.8085955.

(86) Peker, M.; Kocaman, A. S.; Kara, B. Y. Benefits of Transmission Switching and Energy Storage in Power Systems with High Renewable Energy Penetration. *Appl. Energy* **2018**, *228* (April), 1182–1197. https://doi.org/10.1016/j.apenergy.2018.07.008.

(87) Qazi, A.; Hussain, F.; Rahim, N. A. B. D.; Hardaker, G.; Alghazzawi, D.; Shaban, K.; Haruna, K. Towards Sustainable Energy: A Systematic Review of Renewable Energy Sources, Technologies, and Public Opinions. *IEEE Access* **2019**, *7*, 63837–63851. https://doi.org/10.1109/ACCESS.2019.2906402.

(88) Fujimoto, C.; Kim, S.; Stains, R.; Wei, X.; Li, L.; Yang, Z. G. Vanadium Redox Flow Battery Efficiency and Durability Studies of Sulfonated Diels Alder Poly(Phenylene)S. *Electrochem. commun.* **2012**, *20* (1), 48–51. https://doi.org/10.1016/j.elecom.2012.03.037.

(89) Ibrahim, H.; Ilinca, A.; Perron, J. Energy Storage Systems-Characteristics and Comparisons. *Renew. Sustain. Energy Rev.* **2008**, *12* (5), 1221–1250. https://doi.org/10.1016/j.rser.2007.01.023.

(90) Uhrig, M.; Koenig, S.; Suriyah, M. R.; Leibfried, T. Lithium-Based vs. Vanadium Redox Flow Batteries - A Comparison for Home Storage Systems. *Energy Procedia* **2016**, *99* (March), 35–43. https://doi.org/10.1016/j.egypro.2016.10.095.

(91) Jiang, H. R.; Sun, J.; Wei, L.; Wu, M. C.; Shyy, W.; Zhao, T. S. A High Power Density and Long Cycle Life Vanadium Redox Flow Battery. *Energy Storage Mater.* **2020**, *24*, 529–540. https://doi.org/10.1016/j.ensm.2019.07.005.

(92) Zhang, C.; Zhao, T. S.; Xu, Q.; An, L.; Zhao, G. Effects of Operating Temperature on the Performance of Vanadium Redox Flow Batteries. *Appl. Energy* **2015**, *155*, 349–353. https://doi.org/10.1016/j.apenergy.2015.06.002.

(93) Jayathilake, B. S.; Plichta, E. J.; Hendrickson, M. A.; Narayanan, S. R.

Improvements to the Coulombic Efficiency of the Iron Electrode for an All-Iron Redox-Flow Battery. *J. Electrochem. Soc.* **2018**, *165* (9), A1630–A1638. https://doi.org/10.1149/2.0451809jes.

(94) Zhang, C.; Zhang, L.; Yu, G. Eutectic Electrolytes as a Promising Platform for Next-Generation Electrochemical Energy Storage. *Acc. Chem. Res.* **2020**, *53* (8), 1648–1659. https://doi.org/10.1021/acs.accounts.0c00360.

(95) Bian, H. T.; Feng, R. R.; Xu, Y. Y.; Guo, Y.; Wang, H. F. Increased Interfacial Thickness of the NaF, NaCl and NaBr Salt Aqueous Solutions Probed with Non-Resonant Surface Second Harmonic Generation (SHG). *Phys. Chem. Chem. Phys.* **2008**, *10* (32), 4920–4931. https://doi.org/10.1039/b806362a.

(96) Bian, H. T.; Feng, R. R.; Guo, Y.; Wang, H. F. Specific Na+ and K+ Cation Effects on the Interfacial Water Molecules at the Air/Aqueous Salt Solution Interfaces Probed with Nonresonant Second Harmonic Generation. *J. Chem. Phys.* **2009**, *130* (13), 19–21. https://doi.org/10.1063/1.3104609.

(97) Brown, M. A.; Winter, B.; Faubel, M.; Hemminger, J. C. Spatial Distribution of Nitrate and Nitrite Anions at the Liquid/Vapor Interface of Aqueous Solutions. *J. Am. Chem. Soc.* **2009**, *131* (24), 8354–8355. https://doi.org/10.1021/ja901791v.

(98) Hua, W.; Verreault, D.; Allen, H. C. Surface Electric Fields of Aqueous Solutions of NH4NO3, Mg(NO3)2, NaNO3, and LiNO3: Implications for Atmospheric Aerosol Chemistry. *J. Phys. Chem. C* **2014**, *118* (43), 24941–24949. https://doi.org/10.1021/jp505770t.

(99) Hua, W.; Verreault, D.; Adams, E. M.; Huang, Z.; Allen, H. C. Impact of Salt Purity on Interfacial Water Organization Revealed by Conventional and Heterodyne-Detected Vibrational Sum Frequency Generation Spectroscopy. *J. Phys. Chem. C* **2013**, *117* (38), 19577–19585. https://doi.org/10.1021/jp408146t.

(100) Vargaftik, N. B.; Volkov, B. N.; Voljak, L. D. International Tables of the Surface Tension of Water. *Journal of Physical and Chemical Reference Data*. 1983, pp 817–820. https://doi.org/10.1063/1.555688.

(101) Grooms, A. J.; Neal, J. F.; Ng, K. C.; Zhao, W.; Flood, A. H.; Allen, H. C. Thermodynamic Signatures of the Origin of Anti-Hofmeister Selectivity for Phosphate at Aqueous Interfaces. *J. Phys. Chem. A* **2020**, *124* (27), 5621–5630. https://doi.org/10.1021/acs.jpca.0c02515.

(102) Kumal, R. R.; Karam, T. E.; Haber, L. H. Determination of the Surface Charge Density of Colloidal Gold Nanoparticles Using Second Harmonic Generation. *J. Phys. Chem. C* **2015**, *119* (28), 16200–16207. https://doi.org/10.1021/acs.jpcc.5b00568.

(103) Alexandrova, S.; Maslyanitsyn, I. A.; Pamukchieva, V.; Tsvetkov, V. B.; Shigorin, V. D. Second Harmonic Generation in Thin Ge35Sb5S60 Films. *Phys. Wave Phenom.* **2011**, *19* (3), 161–164. https://doi.org/10.3103/S1541308X11030010.

(104) Shao, Y.; Gan, Z.; Epifanovsky, E.; Gilbert, A. T.; Wormit, M.; Kussmann, J.; Lange, A. W.; Behn, A.; Deng, J.; Feng, X.; Ghosh, D.; Goldey, M.; Horn, P. R.; Jacobson, L. D.; Kaliman, I.; Khaliullin, R. Z.; Kuš, T.; Landau, A.; Liu, J.; Proynov, E. I.; Rhee, Y. M.; Richard, R. M.; Rohrdanz, M. A.; Steele, R. P.;

Sundstrom, E. J.; Woodcock, H. L.; Zimmerman, P. M.; Zuev, D.; Albrecht, B.; Alguire, E.; Austin, B.; Beran, G. J. O.; Bernard, Y. A.; Berquist, E.; Brandhorst, K.; Bravaya, K. B.; Brown, S. T.; Casanova, D.; Chang, C. M.; Chen, Y.; Chien, S. H.; Closser, K. D.; Crittenden, D. L.; Diedenhofen, M.; Distasio, R. A.; Do, H.; Dutoi, A. D.; Edgar, R. G.; Fatehi, S.; Fusti-Molnar, L.; Ghysels, A.; Golubeva-Zadorozhnaya, A.; Gomes, J.; Hanson-Heine, M. W.; Harbach, P. H.; Hauser, A. W.; Hohenstein, E. G.; Holden, Z. C.; Jagau, T. C.; Ji, H.; Kaduk, B.; Khistyaev, K.; Kim, J.; Kim, J.; King, R. A.; Klunzinger, P.; Kosenkov, D.; Kowalczyk, T.; Krauter, C. M.; Lao, K. U.; Laurent, A. D.; Lawler, K. V; Levchenko, S. V; Lin, C. Y.; Liu, F.; Livshits, E.; Lochan, R. C.; Luenser, A.; Manohar, P.; Manzer, S. F.; Mao, S. P.; Mardirossian, N.; Marenich, A. V; Maurer, S. A.; Mayhall, N. J.; Neuscamman, E.; Oana, C. M.; Olivares-Amaya, R.; Oneill, D. P.; Parkhill, J. A.; Perrine, T. M.; Peverati, R.; Prociuk, A.; Rehn, D. R.; Rosta, E.; Russ, N. J.; Sharada, S. M.; Sharma, S.; Small, D. W.; Sodt, A.; Stein, T.; Stück, D.; Su, Y. C.; Thom, A. J.; Tsuchimochi, T.; Vanovschi, V.; Vogt, L.; Vydrov, O.; Wang, T.; Watson, M. A.; Wenzel, J.; White, A.; Williams, C. F.; Yang, J.; Yeganeh, S.; Yost, S. R.; You, Z. Q.; Zhang, I. Y.; Zhang, X.; Zhao, Y.; Brooks, B. R.; Chan, G. K.; Chipman, D. M.; Cramer, C. J.; Goddard, W. A.; Gordon, M. S.; Hehre, W. J.; Klamt, A.; Schaefer, H. F.; Schmidt, M. W.; Sherrill, C. D.; Truhlar, D. G.; Warshel, A.; Xu, X.; Aspuru-Guzik, A.; Baer, R.; Bell, A. T.; Besley, N. A.; Chai, J. Da; Dreuw, A.; Dunietz, B. D.; Furlani, T. R.; Gwaltney, S. R.; Hsu, C. P.; Jung, Y.; Kong, J.; Lambrecht, D. S.; Liang, W.; Ochsenfeld, C.; Rassolov, V. A.; Slipchenko, L. V; Subotnik, J. E.; Van Voorhis, T.; Herbert, J. M.; Krylov, A. I.; Gill, P. M.; Head-Gordon, M. Advances in Molecular Quantum Chemistry Contained in the Q-Chem 4 Program Package. *Mol. Phys.* **2015**, *113* (2), 184–215. https://doi.org/10.1080/00268976.2014.952696.

(105) Zhao, Y.; Truhlar, D. G. The M06 Suite of Density Functionals for Main Group Thermochemistry, Thermochemical Kinetics, Noncovalent Interactions, Excited States, and Transition Elements: Two New Functionals and Systematic Testing of Four M06-Class Functionals and 12 Other Function. *Theor. Chem. Acc.* **2008**, *120* (1–3), 215–241. https://doi.org/10.1007/s00214-007-0310-x.

(106) Verma, P.; Truhlar, D. G. Status and Challenges of Density Functional Theory. *Trends Chem.* **2020**, *2* (4), 302–318. https://doi.org/10.1016/j.trechm.2020.02.005.

(107) Hait, D.; Head-Gordon, M. How Accurate Is Density Functional Theory at Predicting Dipole Moments? An Assessment Using a New Database of 200 Benchmark Values. *J. Chem. Theory Comput.* **2018**, *14* (4), 1969–1981. https://doi.org/10.1021/acs.jctc.7b01252.

(108) Møller, M. The Complex Formation of Ferric Ions with Chloride Ions. *J. Phys. Chem.* **1937**, *41* (8), 1123–1128. https://doi.org/10.1021/j150386a010.

(109) Näslund, L. Å.; Cavalleri, M.; Ogasawara, H.; Nilsson, A.; Petterson, L. G. M.; Wernet, P.; Edwards, D. C.; Sandström, M.; Myneni, S. Direct Evidence of Orbital Mixing between Water and Solvated Transition-Metal Ions: An Oxygen 1s XAS and DFT Study of Aqueous Systems. *J. Phys. Chem. A* **2003**, *107* (35), 6869–

6876. https://doi.org/10.1021/jp034296h.
(110) Murata, K.; Irish, D. E.; Toogood, G. E. Vibrational Spectral Studies of Solutions at Elevated Temperatures and Pressures. 11. A Raman Spectral Study of Aqueous Iron(III) Chloride Solutions between 25 and 300 °C. *Can. J. Chem.* **1989**, *67* (3), 517–524. https://doi.org/10.1139/v89-079.
(111) Friedman, H. L. The Visible and Ultraviolet Absorption Spectrum of the Tetrachloroferrate(III) Ion in Various Media. *J. Am. Chem. Soc.* **1952**, *74* (1), 5–10. https://doi.org/10.1021/ja01121a002.
(112) Sharma, S. K. Raman Study of Ferric Chloride Solutions and Hydrated Melts. *J. Chem. Phys.* **1974**, *60* (4), 1355–1357. https://doi.org/10.1063/1.1681206.
(113) Brown, M. F.; Kester, D. R. Ultraviolet Spectroscopic Study of Ferric Iron Solutions. *Appl. Spectrosc.* **1980**, *34* (3), 377–380. https://doi.org/10.1366/0003702804730394.
(114) D'Auria, R.; Tobias, D. J. Relation between Surface Tension and Ion Adsorption at the Air-Water Interface: A Molecular Dynamics Simulation Study. *J. Phys. Chem. A* **2009**, *113* (26), 7286–7293. https://doi.org/10.1021/jp810488p.
(115) Paul, S.; Chandra, A. Dynamics of Water Molecules at Liquid-Vapour Interfaces of Aqueous Ionic Solutions: Effects of Ion Concentration. *Chem. Phys. Lett.* **2003**, *373* (1–2), 87–93. https://doi.org/10.1016/S0009-2614(03)00537-2.
(116) Rashwan, M.; Rehl, B.; Sthoer, A.; Darlington, A. M.; Azam, M. S.; Zeng, H.; Liu, Q.; Tyrode, E.; Gibbs, J. M. Structure of the Silica/Divalent Electrolyte Interface: Molecular Insight into Charge Inversion with Increasing PH. *J. Phys. Chem. C* **2020**, *124* (49), 26973–26981. https://doi.org/10.1021/acs.jpcc.0c09747.
(117) Pegram, L. M.; Record, M. T. Partitioning of Atmospherically Relevant Ions between Bulk Water and the Water/Vapor Interface. *Proc. Natl. Acad. Sci. U. S. A.* **2006**, *103* (39), 14278–14281. https://doi.org/10.1073/pnas.0606256103.
(118) Pegram, L. M.; Record, M. T. Hofmeister Salt Effects on Surface Tension Arise from Partitioning of Anions and Cations between Bulk Water and the Air-Water Interface. *J. Phys. Chem. B* **2007**, *111* (19), 5411–5417. https://doi.org/10.1021/jp070245z.
(119) Götte, L.; Parry, K. M.; Hua, W.; Verreault, D.; Allen, H. C.; Tobias, D. J. Solvent-Shared Ion Pairs at the Air-Solution Interface of Magnesium Chloride and Sulfate Solutions Revealed by Sum Frequency Spectroscopy and Molecular Dynamics Simulations. *J. Phys. Chem. A* **2017**, *121* (34), 6450–6459. https://doi.org/10.1021/acs.jpca.7b05600.
(120) Matubayasi, N.; Takayama, K.; Ito, R.; Takata, R. Thermodynamic Quantities of Surface Formation of Aqueous Electrolyte Solutions X. Aqueous Solution of 2:1 Valence-Type Salts. *J. Colloid Interface Sci.* **2011**, *356* (2), 713–717. https://doi.org/10.1016/j.jcis.2011.01.007.
(121) Levering, L. M.; Roxana Sierra-Hernández, M.; Allen, H. C. Observation of Hydronium Ions at the Air-Aqueous Acid Interface: Vibrational Spectroscopic Studies of Aqueous HCl, HBr, and HI. *J. Phys. Chem. C* **2007**, *111* (25), 8814–8826. https://doi.org/10.1021/jp065694y.

(122) Lopes, L.; De Laat, J.; Legube, B. Charge Transfer of Iron(III) Monomeric and Oligomeric Aqua Hydroxo Complexes: Semiempirical Investigation into Photoactivity. *Inorg. Chem.* **2002**, *41* (9), 2505–2517. https://doi.org/10.1021/ic011029m.
(123) Magini, M.; Radnai, T. X-Ray Diffraction Study of Ferric Chloride Solutions and Hydrated Melt. Analysis of the Iron (III)-Chloride Complexes Formation. *J. Chem. Phys.* **1979**, *71* (11), 4255–4262. https://doi.org/10.1063/1.438233.
(124) Turner, R. C.; Miles, K. E. The Ultraviolet Absorption Spectra of the Ferric Ion and Its First Hydrolysis Product in Aqueous Solutions. *Can. J. Chem.* **1957**, *35* (9), 1002–1009. https://doi.org/10.1139/v57-137.
(125) Böhm, F.; Sharma, V.; Schwaab, G.; Havenith, M. The Low Frequency Modes of Solvated Ions and Ion Pairs in Aqueous Electrolyte Solutions: Iron(Ii) and Iron(Iii) Chloride. *Phys. Chem. Chem. Phys.* **2015**, *17* (29), 19582–19591. https://doi.org/10.1039/c5cp03157e.
(126) Sham, T. K.; Hastings, J. B.; Perlman, M. L. Structure and Dynamic Behavior of Transition-Metal Ions in Aqueous Solution: An EXAFS Study of Electron-Exchange Reactions. *J. Am. Chem. Soc.* **1980**, *102* (18), 5904–5906. https://doi.org/10.1021/ja00538a033.
(127) Wertz, D. L.; Luter, M. D. Evolving Cation Coordination in Aqueous Solutions Prepared from Iron(m) Chloride Hexahydrate. *Inorg. Chem.* **1981**, *20* (9), 3118–3119. https://doi.org/10.1021/ic50223a075.
(128) Subir, M.; Eltouny, N.; Ariya, P. A. A Surface Second Harmonic Generation Investigation of Volatile Organic Compound Adsorption on a Liquid Mercury Surface. *RSC Adv.* **2015**, *5* (30), 23464–23470. https://doi.org/10.1039/c4ra13560a.
(129) Gonella, G.; Lütgebaucks, C.; De Beer, A. G. F.; Roke, S. Second Harmonic and Sum-Frequency Generation from Aqueous Interfaces Is Modulated by Interference. *J. Phys. Chem. C* **2016**, *120* (17), 9165–9173. https://doi.org/10.1021/acs.jpcc.5b12453.
(130) Kappler, A.; Bryce, C.; Mansor, M.; Lueder, U.; Byrne, J. M.; Swanner, E. D. An Evolving View on Biogeochemical Cycling of Iron. *Nat. Rev. Microbiol.* **2021**, *19* (6), 360–374. https://doi.org/10.1038/s41579-020-00502-7.
(131) Schmidt, C.; Behrens, S.; Kappler, A. Ecosystem Functioning from a Geomicrobiological Perspective a Conceptual Framework for Biogeochemical Iron Cycling. *Environ. Chem.* **2010**, *7* (5), 399–405. https://doi.org/10.1071/EN10040.
(132) Jones-lee, A.; Lee, G. F.; Lee, G. F.; Macero, E. El; Macero, E. Role of Iron Chemistry in Controlling the Release of Pollutants. **2005**, *16* (1), 33–41.
(133) Abbate, V.; Hider, R. Iron in Biology. *Metallomics* **2017**, *9* (11), 1467–1469. https://doi.org/10.1039/c7mt90039b.
(134) Stumm, W.; Morgan, J. J. *Aquatic Chemistry : Chemical Equilibria and Rates in Natural Waters*, 3rd ed.; Wiley: New York, 1996.
(135) Takahashi, Y.; Furukawa, T.; Kanai, Y.; Uematsu, M.; Zheng, G.; Marcus, M. A. Seasonal Changes in Fe Species and Soluble Fe Concentration in the Atmosphere

in the Northwest Pacific Region Based on the Analysis of Aerosols Collected in Tsukuba, Japan. *Atmos. Chem. Phys.* **2013**, *13* (15), 7695–7710. https://doi.org/10.5194/acp-13-7695-2013.
(136) Enami, S.; Sakamoto, Y.; Colussi, A. J. Fenton Chemistry at Aqueous Interfaces. *Proc. Natl. Acad. Sci. U. S. A.* **2014**, *111* (2), 623–628. https://doi.org/10.1073/pnas.1314885111.
(137) Jamett, N. E.; Hernández, P. C.; Casas, J. M.; Taboada, M. E. Speciation in the Fe(III)-Cl(I)-H2O System at 298.15 K, 313.15 K, and 333.15 K (25 °C, 40 °C, and 60 °C). *Metall. Mater. Trans. B Process Metall. Mater. Process. Sci.* **2018**, *49* (1), 451–459. https://doi.org/10.1007/s11663-017-1010-0.
(138) Holland, J. G.; Jordan, D. S.; Geiger, F. M. Divalent Metal Cation Speciation and Binding to Surface-Bound Oligonucleotide Single Strands Studied by Second Harmonic Generation. *J. Phys. Chem. B* **2011**, *115* (25), 8338–8345. https://doi.org/10.1021/jp202884n.
(139) Martell, A. E.; Motekaitis, R. J.; Chen, D.; Hancock, R. D.; McManus, D. Selection of New Fe(III)/Fe(II) Chelating Agents as Catalysts for the Oxidation of Hydrogen Sulfide to Sulfur by Air. *Can. J. Chem.* **1996**, *74* (10), 1872–1879. https://doi.org/10.1139/v96-210.
(140) Jain, R.; D., A. D. Thermodynamic Behaviour and Stability Constants of UO22+, Fe3+, Cu2+, Ni2+, Co2+, Fe2+, Mn2+ AND Cd2+ Metal Complexes of 3-Methyl-4-(2-Hydroxyphenyl)-Hydrazono-2-Isoxazolin-5-One. **1982**, *56*, 381–384.
(141) Emerson, D.; Roden, E.; Twining, B. S. The Microbial Ferrous Wheel: Iron Cycling in Terrestrial, Freshwater, and Marine Environments. *Front. Microbiol.* **2012**, *3* (SEP), 383. https://doi.org/10.3389/FMICB.2012.00383/BIBTEX.
(142) Strzepek, R. F.; Maldonado, M. T.; Higgins, J. L.; Hall, J.; Safi, K.; Wilhelm, S. W.; Boyd, P. W. Spinning the "Ferrous Wheel": The Importance of the Microbial Community in an Iron Budget during the FeCycle Experiment. *Global Biogeochem. Cycles* **2005**, *19* (4). https://doi.org/10.1029/2005GB002490.
(143) Millero, F. J.; Hawke, D. J. Ionic Interactions of Divalent Metals in Natural Waters. *Mar. Chem.* **1992**, *40* (1–2), 19–48. https://doi.org/10.1016/0304-4203(92)90046-D.
(144) Sitze, M. S.; Schreiter, E. R.; Patterson, E. V.; Freeman, R. G. Ionic Liquids Based on FeCl3 and FeCl2. Raman Scattering and Ab Initio Calculations. *Inorg. Chem.* **2001**, *40* (10), 2298–2304. https://doi.org/10.1021/ic001042r.
(145) Rustad, D. S.; Gregory, N. W.; Rustad, D. S.; Gregory, N. W. Spectrophotometric Study of Iron(II) Chloride Vapor and of Iron(II) Chloride-Iron(III) Chloride Vapor Mixtures and the Interaction of Iron(II) Chloride with Quartz and Pyrex. *Inorg. Chem.* **1982**, *21* (8), 2929–2933. https://doi.org/10.1021/ic00138a004.
(146) Apted, M. J.; Waychunas, G. A.; Brown, G. E. Structure and Specification of Iron Complexes in Aqueous Solutions Determined by X-Ray Absorption Spectroscopy. *Geochim. Cosmochim. Acta* **1985**, *49* (10), 2081–2089. https://doi.org/10.1016/0016-7037(85)90065-1.
(147) Zhao, R.; Pan, P. A Spectrophotometric Study of Fe(II)-Chloride Complexes in

Aqueous Solutions from 10 to 100°C. *Can. J. Chem.* **2001**, *79* (2), 131–144. https://doi.org/10.1139/cjc-79-2-131.
(148) Garrett, B. C. Ions at the Air / Water Interface. **2004**, No. February, 1146–1148.
(149) Okur, H. I.; Chen, Y.; Wilkins, D. M.; Roke, S. The Jones-Ray Effect Reinterpreted: Surface Tension Minima of Low Ionic Strength Electrolyte Solutions Are Caused by Electric Field Induced Water-Water Correlations. *Chem. Phys. Lett.* **2017**, *684*, 433–442. https://doi.org/10.1016/j.cplett.2017.06.018.
(150) Jarvis, N. L.; Scheiman, M. A. Surface Potentials of Aqueous Electrolyte Solutions. *J. Phys. Chem.* **1968**, *72* (1), 74–78. https://doi.org/10.1021/j100847a014.
(151) Hua, W.; Verreault, D.; Huang, Z.; Adams, E. M.; Allen, H. C. Cation Effects on Interfacial Water Organization of Aqueous Chloride Solutions. I. Monovalent Cations: Li+, Na+, K+, and NH4+. *J. Phys. Chem. B* **2014**, *118* (28), 8433–8440. https://doi.org/10.1021/jp503132m.
(152) Koplitz, L. V.; Mcclure, D. S.; Crerar, D. A. Spectroscopic Study of Chloroiron(II) Complexes in LiCl-DCl-D2O Solutions. *Inorg. Chem.* **1987**, *26* (Ii), 308–313.
(153) Allen, H. C.; Raymond, E. A.; Richmond, G. L. Surface Structural Studies of Methanesulfonic Acid at Air /Aqueous Solution Interfaces Using Vibrational Sum Frequency Spectroscopy. *J. Phys. Chem. A* **2001**, *105* (9), 1649–1655. https://doi.org/10.1021/jp0032964.
(154) Du, Q.; Superfine, R.; Freysz, E.; Shen, Y. R. Vibrational Spectroscopy of Water at the Vapor/Water Interface. *Phys. Rev. Lett.* **1993**, *70* (15), 2313–2316. https://doi.org/10.1103/PhysRevLett.70.2313.
(155) Carey, D. M. Measurement of the Raman Spectrum of Liquid Water. *J. Chem. Phys.* **1998**, *108* (7), 2669–2675. https://doi.org/10.1063/1.475659.
(156) Murphy, W. F.; Bernstein, H. J. Raman Spectra and an Assignment of the Vibrational Stretching Region of Water. *J. Phys. Chem.* **1972**, *76* (8), 1147–1152. https://doi.org/10.1021/j100652a010.
(157) Wall, T. T.; Hornig, D. F. Raman Spectra of Water in Concentrated Ionic Solutions. *J. Chem. Phys.* **1967**, *47* (2), 784–792. https://doi.org/10.1063/1.2140498.
(158) Mizrahi, V.; Sipe, J. E. Phenomenological Treatment of Surface Second-Harmonic Generation. *J. Opt. Soc. Am. B* **1988**, *5* (3), 660. https://doi.org/10.1364/josab.5.000660.
(159) Shen, Y. Optical Second Harmonic Generation At Interfaces. *Annu. Rev. Phys. Chem.* **1989**, *40* (1), 327–350. https://doi.org/10.1146/annurev.physchem.40.1.327.
(160) Woodward, R. I.; Murray, R. T.; Phelan, C. F.; De Oliveira, R. E. P.; Runcorn, T. H.; Kelleher, E. J. R.; Li, S.; De Oliveira, E. C.; Fechine, G. J. M.; Eda, G.; De Matos, C. J. S. Characterization of the Second- and Third-Order Nonlinear Optical Susceptibilities of Monolayer MoS2 Using Multiphoton Microscopy. *2D Mater.* **2017**, *4* (1). https://doi.org/10.1088/2053-1583/4/1/011006.
(161) Boyd, R. W. *Nonlinear Optics*, 3rd Edition.; Academic Press: FL, 2008.
(162) Anderson, S. M. Theoretical Optical Second-Harmonic Calculations for Surfaces.

2016, 148. https://doi.org/10.13140/RG.2.2.35619.66082.
(163) Fischer, P.; Buckingham, A. D. Surface Second-Order Nonlinear Optical Activity. *J. Opt. Soc. Am. B* **1998**, *15* (12), 2951. https://doi.org/10.1364/josab.15.002951.
(164) Geiger, F. M. Second Harmonic Generation, Sum Frequency Generation, and X (3): Dissecting Environmental Interfaces with a Nonlinear Optical Swiss Army Knife. *Annu. Rev. Phys. Chem.* **2009**, *60* (3), 61–83. https://doi.org/10.1146/annurev.physchem.59.032607.093651.
(165) Ohno, P. E.; Chang, H.; Spencer, A. P.; Liu, Y.; Boamah, M. D.; Wang, H. F.; Geiger, F. M. Beyond the Gouy-Chapman Model with Heterodyne-Detected Second Harmonic Generation. *J. Phys. Chem. Lett.* **2019**, *10* (10), 2328–2334. https://doi.org/10.1021/acs.jpclett.9b00727.
(166) Boamah, M. D.; Ohno, P. E.; Lozier, E.; Van Ardenne, J.; Geiger, F. M. Specifics about Specific Ion Adsorption from Heterodyne-Detected Second Harmonic Generation. *J. Phys. Chem. B* **2019**, *123* (27), 5848–5856. https://doi.org/10.1021/acs.jpcb.9b04425.

Appendix A. Deriving the Calculation of Effective Second-Order Susceptibility from CCD Counts

Second harmonic generation from iron (III) chloride solution surfaces comes from the second-order susceptibility ($\chi^{(2)}$) of the interfacial molecules that satisfy the selection rule of noncentrosymmetry. The surface effective second-order susceptibility $\chi^{(2)}_{s,eff}$ is calculated by using the equation developed by Sipe, Shen and de Matos groups with modification of experimental geometry:[158–160]

$$I_{2\omega} = \frac{32\pi^3\omega^2 \sec^2\theta}{\varepsilon_0 c^3 n_1(\omega) n_1(\omega) n_1(2\omega)} \left|\chi^{(2)}_{s,eff}\right|^2 {I_\omega}^2 \quad \text{(Eq. S1)}$$

Here the $I_{2\omega}$ and I_ω are the peak intensity of SH and fundamental photons. ω is the angular frequency of fundamental photon. θ is the incident angle of fundamental beam. ε_0 is the vacuum permittivity. $n_{1,\omega}$ and $n_{1,2\omega}$ are the refractive indices of fundamental and SH photon in air medium, respectively. c is speed of light. The unit of effective second order susceptibility $\chi^{(2)}_{s,eff}$ can be confirmed by applying the units and substituting the peak intensity by electric field into Eq. S1 by the definition $I = \frac{1}{2} c \cdot n \cdot \varepsilon_0 E^2$:

$$(\tfrac{1}{2} c \cdot n \cdot \varepsilon_0) E_{2\omega}^2 = \frac{32\pi^3\omega^2 \sec^2\beta}{\varepsilon_0 c_0^3 n_1(\omega) n_1(\omega) n_1(2\omega)} \left|\chi^{(2)}_{s,eff}\right|^2 (\tfrac{1}{2} c \cdot n \cdot \varepsilon_0)^2 E_\omega^4 \quad \text{(Eq. S2)}$$

After substituting the terms, dimensional analysis is performed:

$$(\tfrac{1}{2}(\tfrac{m}{s}) \cdot n \cdot (\tfrac{F}{m}))(\tfrac{V}{m})^2 = \frac{32\pi^3 \frac{1}{s}^2 \sec^2\beta}{(\frac{F}{m})(\frac{m}{s})^3 n_1(\omega) n_1(\omega) n_1(2\omega)} \left|\chi^{(2)}_{s,eff}\right|^2 (\tfrac{1}{2}(\tfrac{m}{s}) \cdot n \cdot (\tfrac{F}{m}))^2 (\tfrac{V}{m})^4 \quad \text{(Eq. S3)}$$

After elimination of the units, there are two terms remain units:

$$1 = \frac{1}{m^2} \left|\chi^{(2)}_{s,eff}\right|^2 (\tfrac{V}{m})^2 \quad \text{(Eq. S4)}$$

As a result, the unit of squared second order susceptibility is shown in Eq. S5 and the second order susceptibility is in Eq. S6:

$$\left|\chi_{s,eff}^{(2)}\right|^2 = \frac{m^4}{V^2} \quad \text{(Eq. S5)}$$

$$\left|\chi_{s,eff}^{(2)}\right| = \frac{m^2}{V} \quad \text{(Eq. S6)}$$

After the unit is confirmed, the value of $\chi_{s,eff}^{(2)}$ with correct unit is obtained. Note that the general second order induced polarization is considered as a bulk induced polarization $P^{(2)}$, and has a unit of V/m.[161] The corresponding unit of second order susceptibility $\chi^{(2)}$ is m/V, which is defined by the number density in the unit of molecules per unit volume, as shown in Eq. S7:

$$\chi_{\alpha\beta\gamma}^{(2)} = \frac{N}{2\varepsilon_0}\langle i_\alpha j_\beta k_\gamma\rangle\beta_{ijk}^{(2)}, \qquad N\ (unit{:}\frac{molecules}{Volum}) \quad \text{(Eq. S7)}$$

In this study, induced polarizability of molecules on surface $P_{surf}^{(2)}$ has a unit of V.[162] Surface susceptibility is defined as the second order nonlinear contribution of molecules on surface and has a unit of m^2/V and that is from the different unit of surface number density N_{surf}, the number density of molecules per unit area (Eq. S8):[163]

$$\chi_{s,\alpha\beta\gamma}^{(2)} = \frac{N_{surf}}{2\varepsilon_0}\langle i_\alpha j_\beta k_\gamma\rangle\beta_{ijk}^{(2)}, \qquad N_{surf}\ (unit{:}\frac{molecules}{Area}) \quad \text{(Eq. S8)}$$

However, it is difficult to utilize the Eq. S1 to directly calculate the effective second order susceptibility with the peak intensity, because only the average power can be obtained experimentally. Conversion from peak intensity to peak power, and further convert to average power is required. From the relationship between intensity and power, one should get Eq. S9:

$$I_{peak} = \frac{P_{peak}}{\pi r^2} \quad \text{(Eq. S9)}$$

The magnitude of intensity is defined by the area of the laser beam the radius of laser r. However, peak power is determined by the power of a single pulse of laser. Conversion from peak power to average power required the pulse width and repetition rate (Eq. S10):

$$P_{peak} = \frac{P_{avg}}{f\tau} \quad \text{(Eq. S10)}$$

Here f is the repetition rate of the laser pulse (82 MHz), τ is pulse duration (50 fs). To obtain the relationship from peak intensity to average power, Eq. S9 is modified by substituting the Eq. S10, and Eq. S11 is obtained:

$$I_{peak} = \frac{P_{avg}}{f\tau\pi r^2} \quad \text{(Eq. S11)}$$

Then the original equation is rewritten as Eq. S12:

$$\frac{P_{avg,2\omega}}{f\tau\pi(r_{2\omega})^2} = \frac{32\omega^2 \sec^2\theta}{\varepsilon_0 n_{1,\omega}^2 n_{1,2\omega} c^3} \left|\chi_{S,\,eff}^{(2)}\right|^2 \left(\frac{P_{avg,\omega}}{f\tau\pi(r_\omega)^2}\right)^2 \quad \text{(Eq. S12)}$$

Note that the radius of focused fundamental beam on surface is different than SH beam radius that generated from the surface. Since the ideal fundamental beam shape maintains Gaussian distribution, the radius of SH photon is the square root of 2 (Eq. S13):

$$r_{2\omega} = \frac{1}{\sqrt{2}} r_\omega \quad \text{(Eq. S13)}$$

In this case, the radius of SH photon in Eq. S12 can be replaced by the radius of fundamental. The radius of the fundamental is determined experimentally. For example, before laser is focused by a lens, the beam spot is provided from the specification of instrument. Here 2 mm of the laser diameter and a lens with a focal length f = +75 mm is

used for calculation. The focused beam size is obtained by the diffraction limited equation:

$$2w_0 = \frac{4\lambda}{\pi} \times \frac{f}{d} \quad \text{(Eq. S14)}$$

Here w_0 is the focused beam radius, λ is the wavelength of laser (805 nm), d is the diameter of fundamental before focused (2mm). The focused beam radius is calculated as $w_0 = r_\omega$ is 19.2 μm, and this value can be applied to the calculation of effective susceptibility. After acquired the relationship from Eq. S13, the Eq. S12 is updated:

$$\frac{P_{avg,2\omega}}{f\tau\pi(\frac{1}{\sqrt{2}}r_\omega)^2} = \frac{32^{\ 2}\sec^2\theta}{\varepsilon_0 n_{1,\omega}^2 n_{1,2\omega} c^3}\left|\chi_{s,\,eff}^{(2)}\right|^2 (\frac{P_{avg,\omega}}{f\tau\pi(r_\omega)^2})^2 \quad \text{(Eq. S15)}$$

After rearrangement in Eq. S15, the final equation for calculating:

$$P_{avg,2\omega} = \frac{16\omega^2\sec^2\theta}{\varepsilon_0 n_{1,\omega}^2 n_{1,2\omega} c^3 f\tau(\pi r_\omega^2)}\left|\chi_{s,\,eff}^{(2)}\right|^2 P_{avg,\omega}^2 \quad \text{(Eq. S16)}$$

Although Eq. S16 is the equation to calculate the effective susceptibility, the average power of SH photon is determined from CCD counts. Yet, the CCD counts of 403 nm photons require a conversion from photon counts to CCD counts. A series of attenuation and conversion is calculated from the sample surface to CCD by Figure A1:

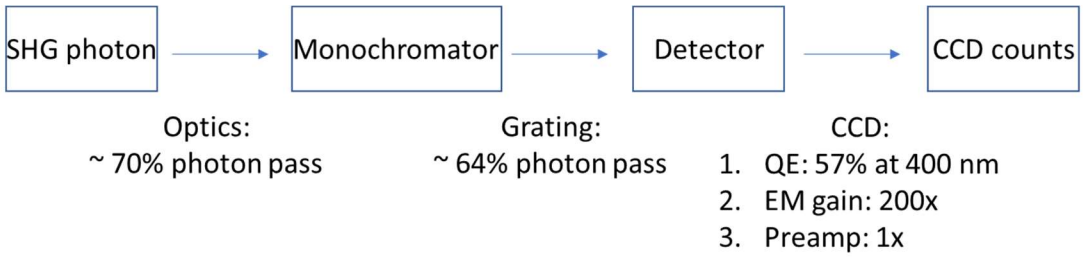

Figure A1 Calculation of SH photon from sample surface to CCD.

Here the SH photon loss from optics is measured as around 30%, including all the optics from L2 to L3 in Figure 1. The remaining 70% of SH photons entered the monochromator. Grating efficiency shows around 65% of the 403 nm photons is diffracted by a grating with 300 lines/mm and blazed at 500 nm (see Figure A2). The SH photons are eventually detected by CCD.

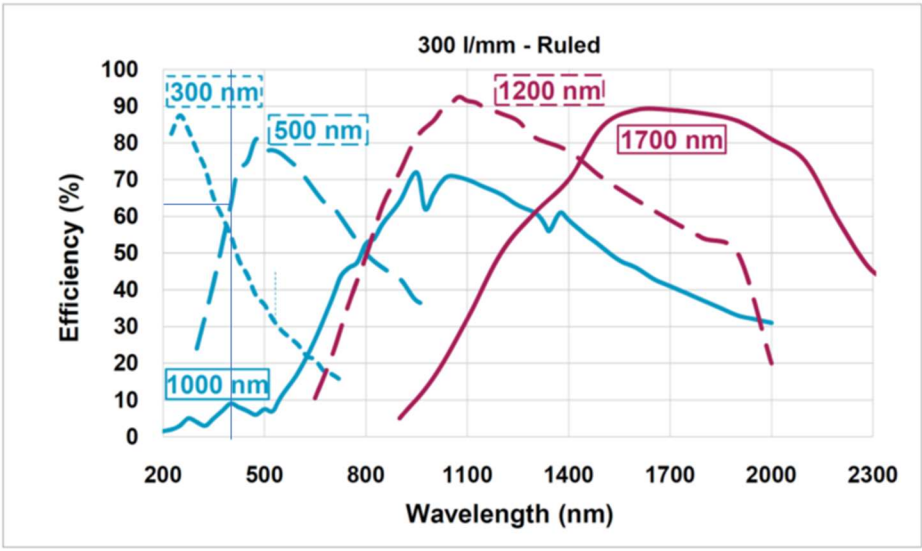

Figure A2 Grating efficiency of 300 lines/mm with different blazed wavelengths. Note that the efficiency of photon at 400 nm with 500 nm blazed grating is indicated as solid lines. (From Richardson grating)

When the SH photons are detected by CCD, a portion of the photons are sensed by the quantum efficiency (QE) of the CCD, then magnified by electron multiplier (EM gain) and pre-amplifier. Figure A3 shows a process of determining the original signal counts

and Figure A4 shows the quantum efficiency of the CCD. Typical experimental parameters such as exposure time, pre-amp gain and EM gain are indicated in Figure A5.

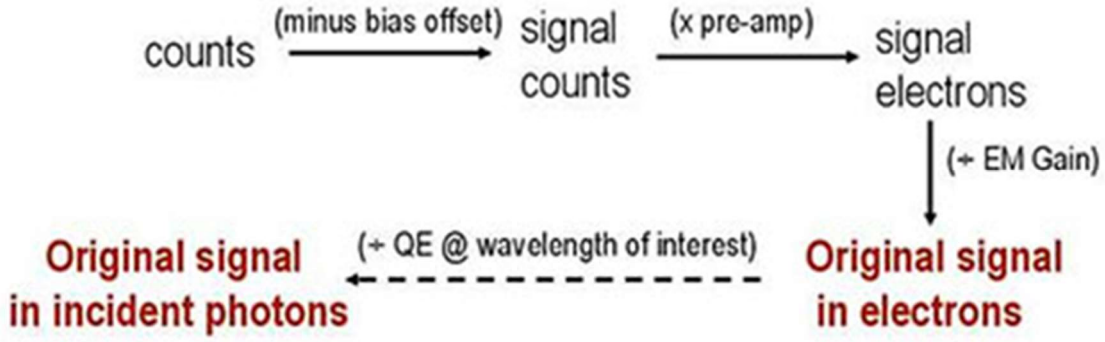

Figure A3 Conversion from photon counts to CCD counts. (From Andor website)

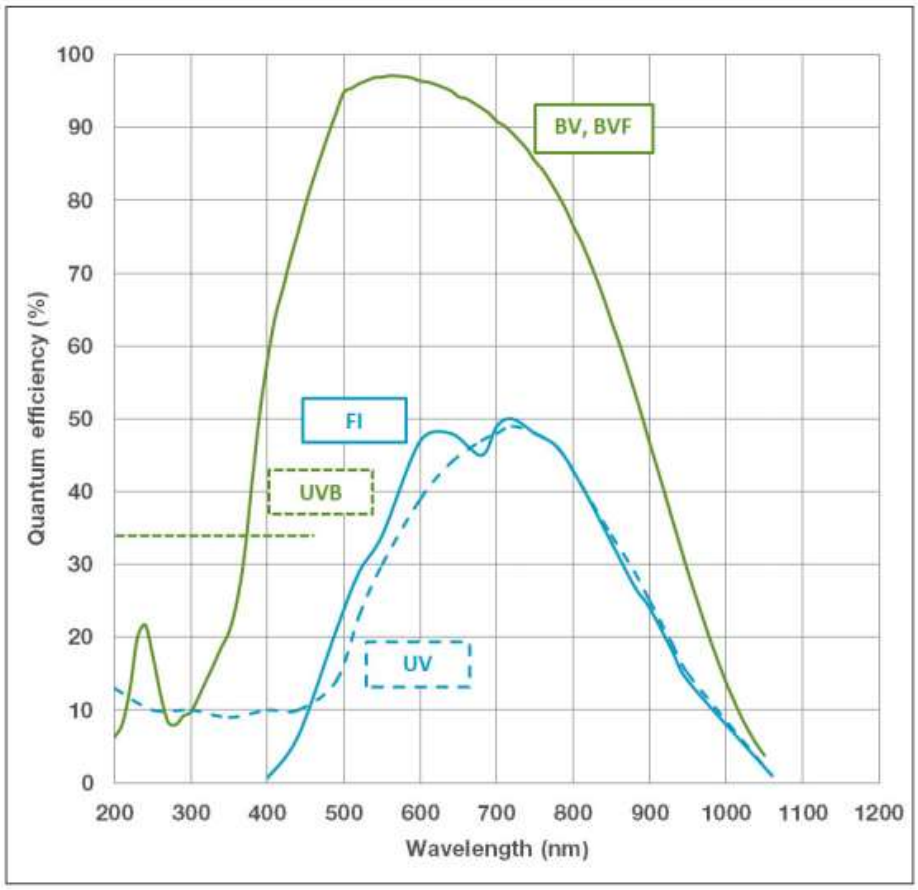

Figure A4 Quantum efficiency of Andor Newton EMCCD. Here CCD with a model of 970BV is used from our laboratory.

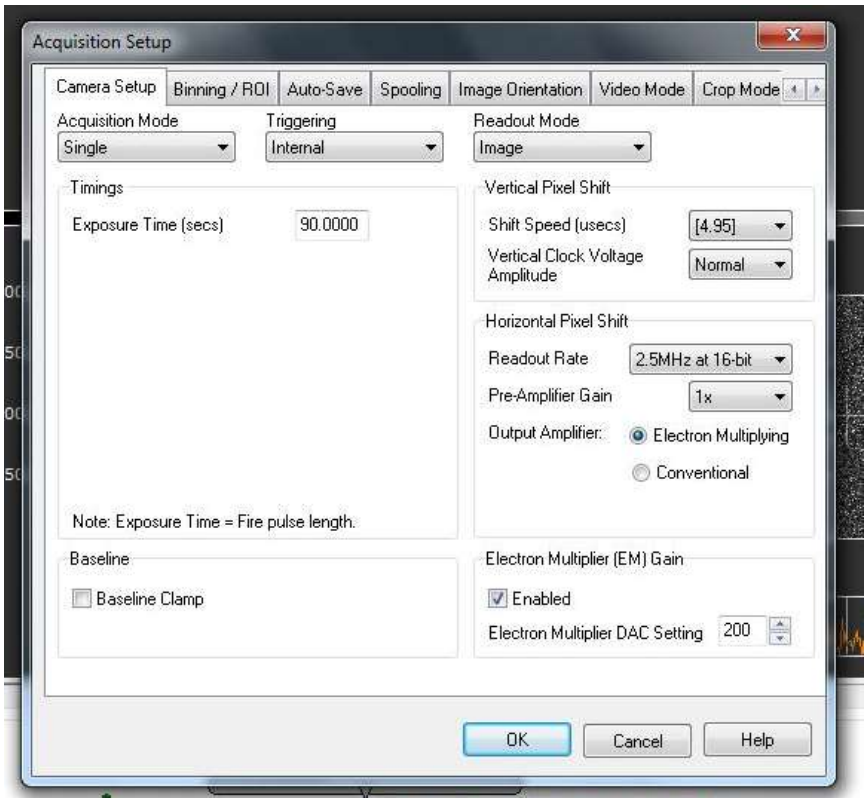

Figure A5 Acquisition setup of EMCCD in Andor SOLIS program.

An instrumentation factor F is considered in the process of photon conversion. For example, with the condition noted above, photon counts from sample surface can be back calculated from instrumentation factor (Eq. S17):

$$F = 1 \div Optics \div Grating \div QE \div EM\ gain \div (Pre - amp)$$

$$F = 1 \div 70\% \div 64\% \div 57\% \div 200 \div 1 = 0.01958 \quad \text{(Eq. S17)}$$

And the actual photons generated from surface can be obtained by multiplying the instrumentation factor to CCD counts. Finally, the conversion from CCD counts to average power of SH photons can be calculated (note that the unit of CCD counts is count per second):

$$P_{avg,2\omega} = \frac{E}{t} = \frac{hc}{\lambda} \times CCD\ (\frac{counts}{s}) \times F \quad \text{(Eq. S18)}$$

$$CCD \times \frac{hcF}{\lambda} = \frac{16\omega^2 \sec^2\theta}{\varepsilon_0 n_{1,\omega}^2 n_{1,2\omega} c^3 f \tau (\pi r_\omega^2)} \left|\chi_{s,eff}^{(2)}\right|^2 P_{avg,\omega}^2 \quad \text{(Eq. S19)}$$

By applying all the parameters into Eq. S19, the effective second order susceptibility $\chi_{s,eff}^{(2)}$ can be calculated. Note that the uncertainty of the susceptibility comes from the estimated photon reduction of optics because it is difficult to measure the SH photons experimentally.

$\chi_{s,eff}^{(2)}$ is the effective second-order susceptibility of the surface species, which includes interfacial iron complexes and the water molecules. Under the selection rule of second-order nonlinear processes, the bulk water solution, which is considered a centrosymmetric medium, does not generate a second harmonic E-field. In the interfacial region, the SHG E-field can arise from resonance and non-resonance conditions:

$$\chi_{s,eff}^{(2)} = \chi_{water}^{(2)} + \chi_{ion}^{(2)} \quad \text{(Eq. S20)}$$

$$\chi_{s,eff}^{(2)} = \chi_{NR,water}^{(2)} + \chi_{R,FeCl_3}^{(2)} + \chi_{EDL}^{(2)} \quad \text{(Eq. S21)}$$

where $\chi_{NR,water}^{(2)}$ is the non-resonant second-order susceptibilities of water and chloride anions, the $\chi_{R,FeCl_3}^{(2)}$ is the total signal of iron chloride solution on the surface. $\chi_{EDL}^{(2)}$ is the nonlinear susceptibility of electrical double layer (EDL), and the $\chi_{EDL}^{(2)}$ is related to the third-order nonlinear susceptibility and interfacial potential ($\chi_{EDL}^{(2)} = \chi^{(3)}\Phi(0)$). While the presence of ions in solution, the $\chi^{(3)}$ term is shown to have a significant contribution, and can be separated from the overall SHG signal. [129,164–166] However, at high

concentration (> 1M), the contribution of EDL becomes negligible compared to resonant susceptibility $\chi^{(2)}_{R,FeCl_3}$.

Appendix B. Calculation of Coherence Length

Coherence length determines the probing depth of SHG and it is inversely proportional to phase mismatching. Further details or calculation can be found regarding the two terms. Here, the calculation of coherence length is mainly refer to Roke and coworker[129] (*J. Phys. Chem. C* **2016**, *120*, 9165-9173) and the supporting information equation S7 from Ohno *et al.*[165] (*J. Phys. Chem. Lett.* **2019**, *10*, 2328-2334).

Here, we first need to consider the vector of the direction of fundamental and SH photons. For a reflection geometry, as shown in Figure B1, the direction of z axis is set to point from air to the solution phase.

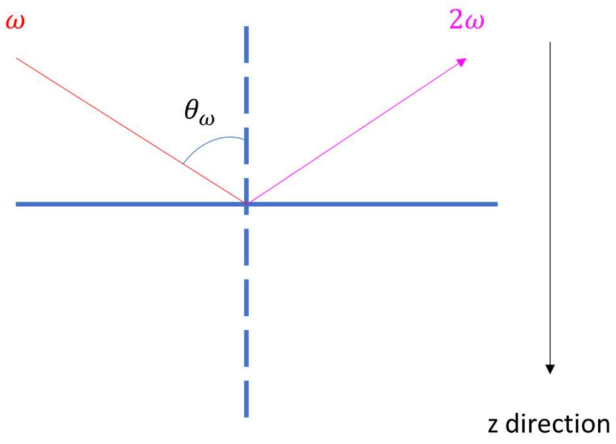

Figure B1 Reflection geometry of SHG and the direction of z axis.

From phase mismatch equation, it showed the mismatch among three photons are the summation of all k vectors:

$$\Delta k_z = |k_{1z} + k_{2z} - k_{0z}| = k_{1z} + k_{2z} + k_{0z} \quad \text{(Eq. S22)}$$

Δk_z is the total difference k vector in z direction, k_{1z} and k_{2z} are the k vector of fundamental (800 nm) and k_{0z} is the k vector of SH photon. As shown in Figure B2, since the direction of fractional vector of SH photon along z axis is opposite to the fundamental, the sign of k vector for SH photon has to be negative:

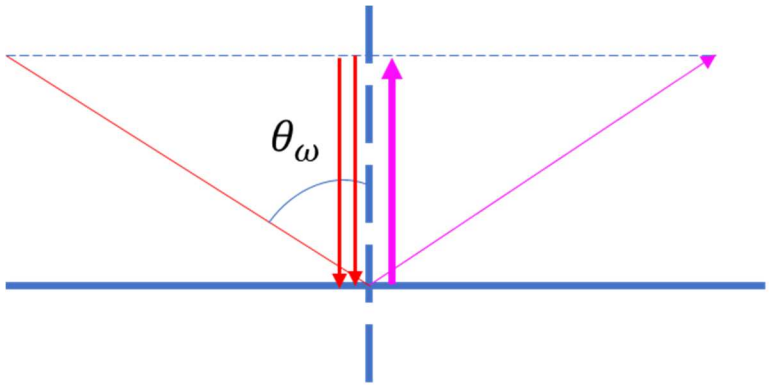

Figure B2 Direction of k vectors in z components.

Based on this concept, the Eq. S22 can be rewritten as:

$$\Delta k_z = |k_{1z} + k_{2z} - k_{0z}| = 2k_{1z} - (-k_{0z}) = 2k_{1z} + k_{0z} \quad \text{(Eq. S23)}$$

After solved the direction of the k vectors, the actual depth of the occurrence of SH process is in the solution phase, rather than the surface. From the viewpoint of light

travelling from one into another medium, Snell's law is considered to calculate the refracted angle of the fundament light:

$$n_{\omega,air} \sin \theta_{\omega,air} = n_{\omega,water} \sin \theta_{\omega,water} \quad \text{(Eq. S24)}$$

From the equation of Snell's law, the refractive indices of air and water for fundamental is 1.000 and 1.329. If the input angle of fundamental is 68.2°, the refracted angle of fundamental is 44.3°. This refracted angle is applied to calculate the phase mismatch condition. As shown in Figure B3, the angle of SH photon can be calculated by conservation of momentum:

$$n_{2\omega}k_{2\omega} \sin \theta_{2\omega} = n_{\omega}k_{\omega} \sin \theta_{\omega} + n_{\omega}k_{\omega} \sin \theta_{\omega} = 2n_{\omega}k_{\omega} \sin \theta_{\omega} \quad \text{(Eq. S25)}$$

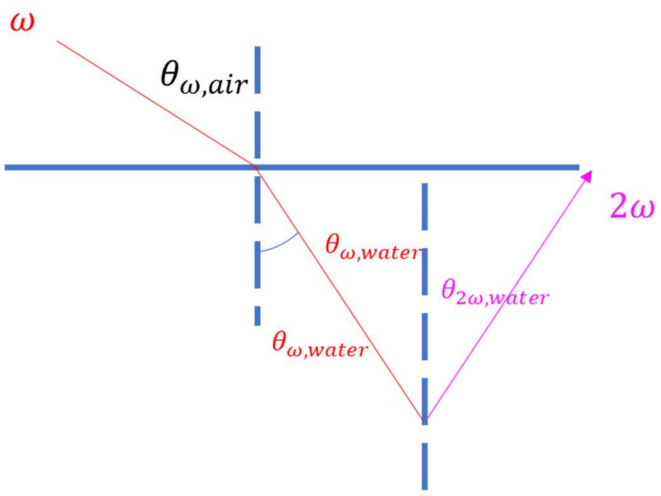

Figure B3 Generation of SH photon is considered underneath the surface.

Once the SH angle is obtained, the phase mismatch Eq. S26 can be obtained:

$$\Delta k_z = \frac{1}{c}(2\omega n_{\omega,water} \cos \theta_{\omega,water} + (2\omega) n_{2\omega,water} \cos \theta_{2\omega,water}) \quad \text{(Eq. S26)}$$

Here c is speed of light, $c = 3 \times 10^8\ (m/s)$, ω is the angular frequency of fundamental 805 nm light, $\omega = 2.34 \times 10^{15}\ (1/s)$, the refractive indices of water for both fundamental $n_{\omega,water}$ and SH light $n_{2\omega,water}$ are 1.329 and 1.339, respectively. As mentioned above, the refracted angle of fundamental $\theta_{\omega,water}$ and reflecting angle of SH $\theta_{2\omega,water}$ are 44.33º and 43.92º, respectively. With all the numbers above, the value of phase mismatch Δk_z is 2.99x10^7 m^{-1}. The corresponding coherence length l_c:

$$l_c = \frac{1}{\Delta k_z} \qquad \text{(Eq. S27)}$$

The value of coherence length is calculated as 33 nm from current experiment geometry.

Appendix C. SHG Alignment and Optimization of Signal

Instrumentation of SHG includes a brief tutor of the alignment, setup of the reference channel and the method of reducing noise. Here a schematic figure is shown in Figure 1:

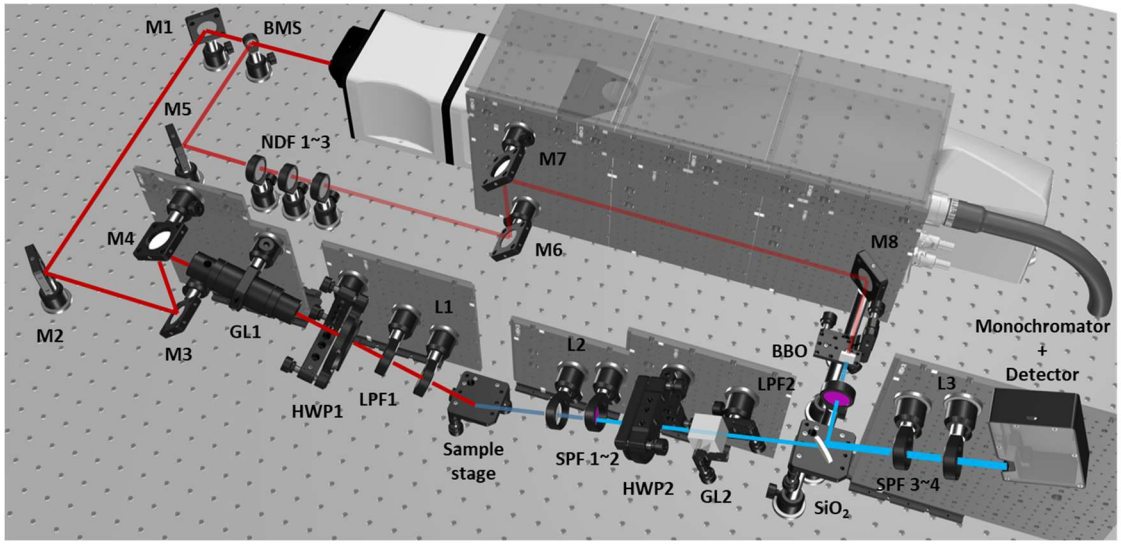

Figure C1 (Same as Figure 1) Schematic representation of the second harmonic generation spectroscopic instrument. BMS: 85/15 beam splitter. M1 ~ M8 are dielectric mirrors. GL1, GL2 are 800 nm and 405 nm Glan-laser polarizer. HWP1, HWP2 are 800 achromatic half-wave plate and 405 nm half-wave plate. L1~L3 are +75 mm, +100 mm, and +50 mm plano-convex lenses with antireflective coating between 650 to 1050 nm. LPF1~2: 690 nm long pass filter, SPF1~4 are 785 nm short pass filters. SiO_2 is silica plate, NDF1~3 are neutral density filters. BBO is BBO crystal. The incident angle of 805 nm beam is 67.2º. The graphical CAD design is constructed from 3DOpticX.

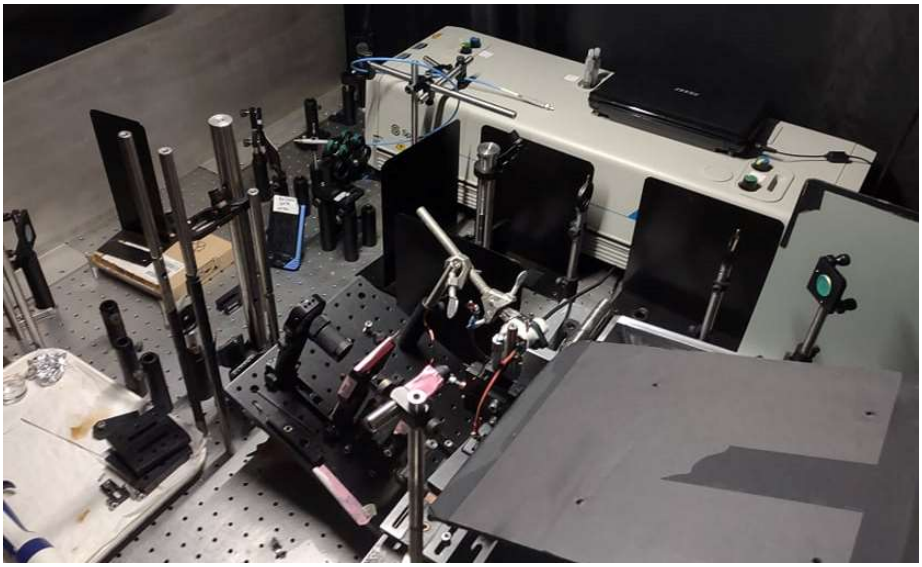

Figure C2 Picture of SHG system in the Allen lab. Note that the detection channel (from L2 to L3, the whole beam path of blue beam in Figure C1) is covered by a black paper box to avoid any scattering light from the environment.

The system is divided into two channels: sample channel from M1 to sample stage where the reference channel starts from BMS to LPF2. The direction of the laser beam requires optimization occasionally. Usually, there are at least four irises to confirm the alignment of each of the beam paths: (1) Iris A locates between M2 and M3 and it is used to confirm the direction of Tsunami laser. (2) The iris B is located next to the paper box shown in Figure C2. (3) Irises C in between M7 and M8 are for the alignment of reference channel. Lastly, the (4) iris D is to confirm the beam direction to BBO crystal.

Usually, the direction of laser beam from Tsunami and reference channel does not change. However, direction of incident beam and detection beam (M4 to L2 from Figure C1) might be affected by mandatory experiment. For instance, because lens L1 is set in front of the sample stage, it is easily to be contaminated by droplets from sample or

is tilted by accident while loading the sample on stage. Thus, the SHG intensity might be affected, and optimization is required.

The first and most important thing in alignment is to confirm the height of iris B because the height of the well-aligned beam is dependent to the iris B. First, iris B is set as the same height to the center of the slit in front of monochromator, which is 13.4 cm. The iris B can confirm the alignment of incident beam (M4 to L1) and SH line (L2 to L3). After, the alignment between M4 to sample stage must be confirmed. Here, iris B is sat at GL1 and confirm the reflection of M3. If the laser beam does not pass through the iris B, adjustment of mirror M3 is required. Then the iris B is sat in front of L1, and then the laser direction is confirmed by iris B. Similarly to M3, if the laser beam is not centered, adjustment of M4 is needed. Further, alignment of M3 and M4 requires multiple times until the laser is completely centered when iris B is located at both GL1 and L1. Later, a solution with high SHG response is used to process the further alignment steps. Solution such as malachite green (around 50 μM) is recommended for acquiring high SHG intensity from CCD. Alignment at SH channel is performed when lenses and filters are removed, liquid sample is set on the sample stage and the laser is reflected from the sample surface. Then the correct height of the liquid sample can be adjusted to the center of the iris B at location L3. After successfully aligned the directions of incident beam and SH line, the lenses can also be aligned regarding to the height of iris B at L3.

Alignment of SHG with neat water is challenging because this is a nonresonant process in SHG. However, malachite green or other solid sample such as gold mirror or GaAs crystal is resonantly respond to the laser excitation. As shown in Figure C3, GaAs

crystal has the strongest response with the exposure time at 5 second, followed by gold mirror and malachite green solution. However, it is suitable for using malachite green while the alignment process because the surface of solid samples is not perfectly perpendicular to the surface normal, causing the possibility of misalignment.

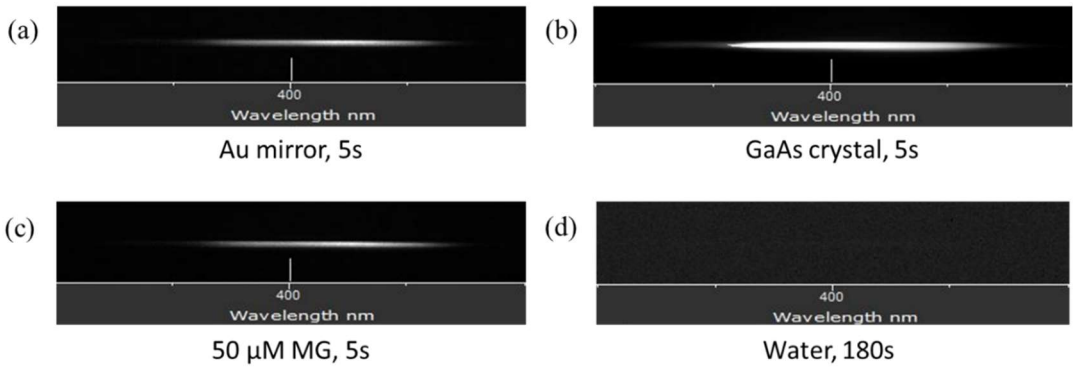

Figure C3 SHG intensity of (a) gold mirror, (b) GaAs crystal, (c) malachite green and (d) neat water are collected by CCD.

Further, after the completion of alignment, environmental scattering light contributes a significant amount of background noise. This environmental background can be minimized by the paper box (shown on the bottom right in Figure C2). After covered by the box, the CCD counts of background is reduced significantly, and the data of neat water is reproducible (Figure C4).

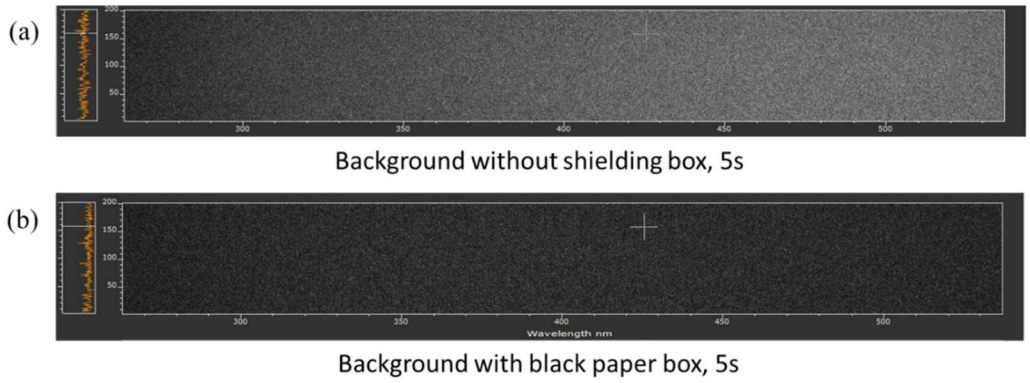

Figure C4 CCD image of SHG background for (a) without paper card and (b) with paper box covered.

After the SH line is covered by paper box, with proper alignment, the image of neat water and the reference channel can be observed on one image (Figure C5). Note that SiO_2 plate can be inserted after alignment of SH line and the reference beam can be adjusted in x and y direction by the mount.

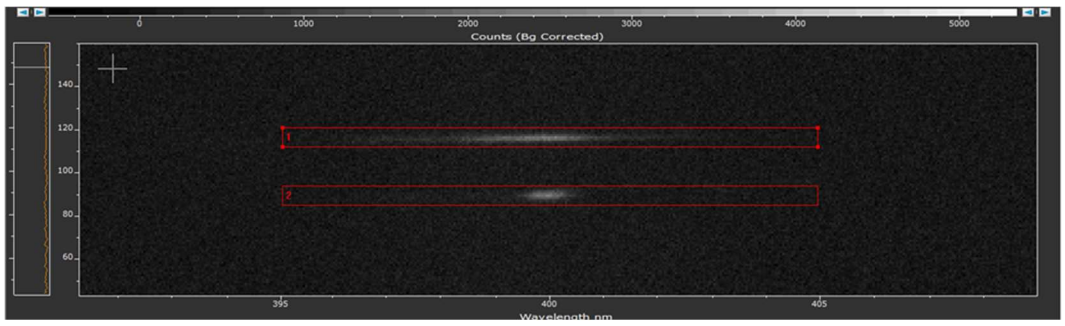

Figure C5 CCD counts for neat water (top) and reference signal of BBO crystal.

Appendix D. Debye Length and Fitting Approach of Frumkin-Fowler-Guggenheim Adsorption Model

Debye Length of $FeCl_3$ Solutions:

Debye length of $FeCl_3$ solution is calculated with the equation for electrolyte solution:

$$\lambda_D = \sqrt{\frac{\varepsilon_0 \varepsilon_r k_B T}{2\times 10^3 N_A e^2 I}} \quad \text{(Eq. S28)}$$

In Eq. S28, λ_D is the Debye length in the unit of meter, ε_0 is the vacuum permittivity, ε_r is the dielectric constant, k_B is the Boltzmann constant, T is the absolute temperature in kelvins, N_A is the Avogadro's number, e is the elementary charge, I is the ionic strength of the electrolyte in the unit of M. After applying the parameters in standard temperature and pressure (STP) conditions, the Debye length of $FeCl_3$ solutions is calculated and is shown below:

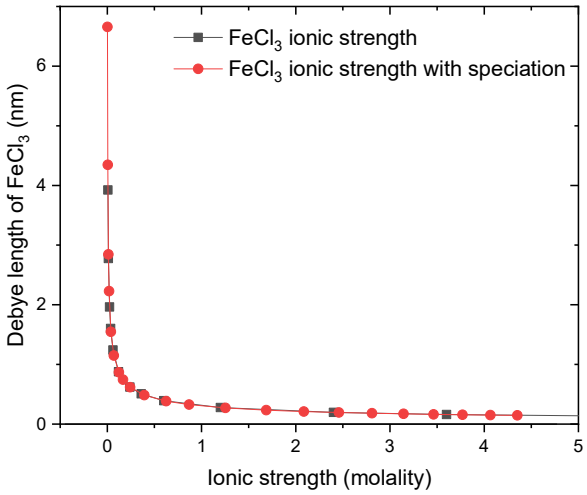

Figure D1 Debye length of $FeCl_3$ solutions plotted with the ionic strength (black) and speciation calibrated ionic strength (red).

Table D1 Data of Debye length of $FeCl_3$ solution with ionic strength and speciation calibrated ionic strength.

	$FeCl_3$		$FeCl_3$ - speciation calibrated	
Concentration (molality)	Ionic strength (molality)	Debye length nm	Ionic strength (molality)	Debye length nm
5.5	33	0.05	4.351	0.15
5	30	0.06	4.066	0.15
4.5	27	0.06	3.770	0.16
4	24	0.06	3.463	0.16
3.5	21	0.07	3.144	0.17
3	18	0.07	2.809	0.18
2.5	15	0.08	2.458	0.19
2	12	0.09	2.085	0.21
1.5	9	0.10	1.687	0.23
1	6	0.12	1.254	0.27
0.6	3.6	0.16	0.868	0.33
0.4	2.4	0.20	0.624	0.39
0.2	1.2	0.28	0.392	0.49
0.1	0.6	0.39	0.243	0.62
0.06	0.36	0.51	0.167	0.75
0.04	0.24	0.62	0.123	0.87
0.02	0.12	0.88	0.070	1.15
0.01	0.06	1.24	0.039	1.55
0.006	0.036	1.61	0.019	2.24
0.004	0.024	1.97	0.011	2.85
0.002	0.012	2.78	0.005	4.36
0.001	0.006	3.94	0.002	6.67

Fitting Approach of Frumkin-Fowler-Guggenheim (FFG) Adsorption Model:

FFG model was applied to fit the SHG data of $FeCl_3$ solutions with the excitation wavelength at 800 and 860 nm. However, the fitting cannot be carried out directly. Here, FFG equation is adapted from Eq. 2.6 and showed below:

$$K'_{FFG}[Fe]_{Bulk} = \frac{\theta}{1-\theta} e^{-w\theta} \quad \text{(Eq. S29)}$$

The surface coverage θ is connected to the normalized E-field of SHG, as showed in Eq. S30:

$$E_{SHG,Normalized} = 1 + B\theta \quad \text{(Eq. S30)}$$

Where details of Eq. S30 can be referred to Eq. 2.2. After rearrangement, Eq. S30 can be expressed as a term of surface coverage:

$$\theta = \frac{E_{SHG,Normalized}-1}{B} \quad \text{(Eq. S31)}$$

Surface coverage term in Eq. S29 is substituted by the term in Eq. S31, and Eq. 29 can be written as:

$$K'_{FFG}[Fe]_{Bulk} = \frac{E_{SHG,Normalized}-1}{B-(E_{SHG,Normalized}-1)} e^{-\frac{w(E_{SHG,Normalized}-1)}{B}} \quad \text{(Eq. S32)}$$

Normalized SHG data of $FeCl_3$ solutions can be fitted by FFG model by using $[Fe]_{Bulk}$ as Y-axis and $E_{SHG,Normalized} - 1$ as X-axis. An example of fitting results of $FeCl_3$ SHG data with excitation at 800 nm is shown in Figure D2:

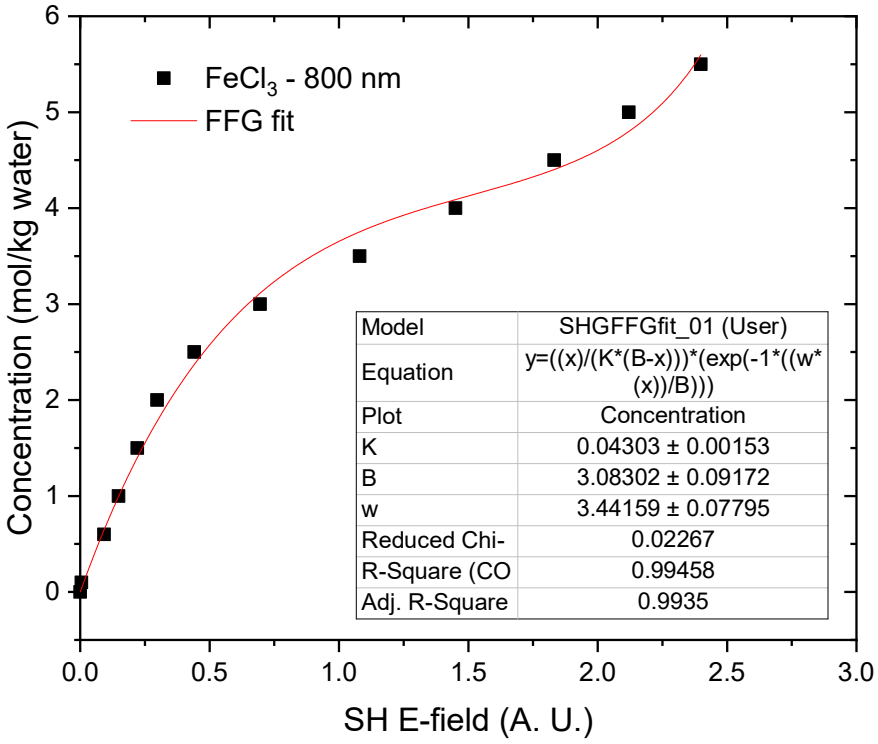

Figure D2 Fitting result of SHG of $FeCl_3$ solutions with FFG adsorption model. Note that X-axis is normalized SHG E-field -1 and Y-axis is concentration in the unit of molality. Fitting equation and R^2 are shown in the table.